TECHNISCHE UNIVERSITÄT MÜNCHEN

TUM School of Computation, Information and Technology

Integrated Data Analysis augmented by Kinetic Modeling

Michael George Bergmann

Vollständiger Abdruck der von der TUM School of Computation, Information and Technology der Technischen Universität München zur Erlangung der akademischen Grades eines

Doktors der Naturwissenschaften
(Dr. rer. nat.)

genehmigten Dissertation.

Vorsitz:	Prof. Dr. Christian Mendl
Prüfer der Dissertation:	1. Hon.-Prof. Dr. Frank Jenko
	2. Priv.-Doz. Dr. Udo von Toussaint

Die Dissertation wurde am 30.08.2023 bei der Technischen Universität München eingereicht und durch die TUM School of Computation, Information and Technology am 29.01.2024 angenommen.

DEPARTMENT OF INFORMATICS

TECHNISCHE UNIVERSITÄT MÜNCHEN

PhD Thesis in Computer Science

Integrated Data Analysis augmented by Kinetic Modeling

Integrierte Daten Analyse erweitert durch Kinetische Modelle

Author:	Michael George Bergmann
Supervisor:	Frank Jenko
Advisor:	Rainer Fischer
Submission Date:	28.08.2023

I confirm that this PhD Thesis in Computer Science is my own work and I have documented all sources and material used.

Munich, 28.08.2023 Michael George Bergmann

Abstract

Density and temperature radial profiles are essential for understanding the behavior and characteristics of fusion plasma experiments. However, due to the inherent complexity and uncertainties in plasma measurements, obtaining accurate and reliable profiles from experimental data is often challenging. To address this challenge, the Integrated Data Analysis (IDA) framework incorporates various diagnostics and prior knowledge to refine the estimation of plasma parameters. By leveraging Bayesian probability theory, IDA can effectively combine the uncertain measurement data from a diverse range of diagnostics and generate more robust density and temperature profiles.

Due to the incomplete coverage of the plasma parameter space, fitted profiles can match the measured data but have gradients that contradict transport theory. In this thesis, an extension of IDA has been established to further enhance the accuracy of IDA-fitted profiles by integrating the modeling suite ASTRA with the quasi-linear transport solver TGLF. This theoretical feedback uses the simulation of plasma profiles and their uncertainties as an additional prior. By doing so, the physically reasonable parameter space is better constrained. The improvement of the profiles is tested by comparing the ion and electron heat flux to the power balance while still maintaining alignment with experimental data.

The application of this physics-motivated prior extends to various plasma scenarios, allowing researchers to explore different operational conditions and analyze their impact on the plasma profiles. The results demonstrate the effectiveness of incorporating prior knowledge and simulated profiles in refining the estimation process, leading to a better understanding of plasma behavior and more accurate predictions.

This work represents a significant step towards making IDA more robust against measurement uncertainties or the lack of measurements. By combining multiple transport solvers with different levels of complexity and computing costs in a multi-fidelity approach, the reliability and accuracy of IDA can be further enhanced. This broader effort acknowledges the inherent challenges of plasma diagnostics and aims to provide researchers with a comprehensive toolkit for characterizing fusion plasmas accurately.

In summary, the Integrated Data Analysis code leverages Bayesian probability theory, prior information, and simulated profiles to provide density and temperature radial profiles of fusion plasmas. IDA improves the accuracy and robustness of plasma parameter estimation by addressing measurement uncertainties and incorporating additional prior knowledge. The integration of ASTRA and TGLF enables a feedback loop that refines the profiles and enhances the heat flux match while maintaining consistency with experimental data. This

work contributes to a broader initiative of combining multiple transport solvers in a multi-fidelity approach to enhance the reliability of IDA and advance our understanding of fusion plasmas.

Kurzfassung

Radiale Dichte- und Temperaturprofile sind entscheidend für das Verständnis des Verlaufs und der Eigenschaften von Fusionsplasmaexperimenten. Aufgrund der inhärenten Komplexität und Unsicherheiten bei Plasmamessungen ist es oft schwierig, genaue und zuverlässige Profile aus experimentellen Daten abzuleiten. Um diese Herausforderung zu meistern, beinhaltet das Integrated Data Analyse (IDA) Modell verschiedene Diagnostiken und A-priori-Wahrscheinlichkeiten, um die Schätzung der Plasmaparameter zu verfeinern. Durch die Nutzung der Bayes'schen Wahrscheinlichkeitstheorie kann IDA ein breites Spektrum von Diagnostiken effektiv kombinieren und robustere Dichte- und Temperaturprofile aus unsicheren Datenmessungen erzeugen.

Aufgrund von Messlücken und fehlerhafter Diagnostik ist eine vollständige Abdeckung des Plasmaparameterraums nicht möglich. Hierdurch können die angepassten IDA Profile mit den gemessenen Daten übereinstimmen, aber Gradienten aufweisen die der Transporttheorie widersprechen.

In dieser Arbeit wird eine Erweiterung von IDA entwickelt, um die Genauigkeit von IDA-angepassten Profilen weiter zu verbessern. Zu diesem Zweck wird der quasi-linearen Turbulenzcode TGLF mit dem die Modellierungscode ASTRA integriert. Diese theoretische Rückkopplung nutzt die Simulation von Plasmaprofilen und deren Unsicherheiten als zusätzliche A-priori-Wahrscheinlichkeit. Auf diese Weise wird der physikalisch sinnvolle Parameterraum besser eingegrenzt. Die Verbesserung der Profile wird durch den Vergleich des Ionen- und Elektronenwärmestroms mit der Leistungsbilanz bei gleichzeitiger Übereinstimmung mit den experimentellen Daten getestet.

Die Anwendung dieser Physik basierten A-priori-Wahrscheinlichkeit erstreckt sich auf verschiedene Plasmaszenarien, die es den Forschenden ermöglichen, verschiedene Betriebsbedingungen zu erforschen und deren Auswirkungen auf die Plasmaprofile zu analysieren. Die Ergebnisse zeigen die Wirksamkeit der Einbeziehung von Vorwissen und simulierten Profilen zur Verfeinerung des Abschätzungsprozesses, was zu einem besseren Verständnis des Plasmaverhaltens und genaueren Vorhersagen führt.

Diese Arbeit leistet ein wichtigen Beitrag, um IDA robuster gegenüber Messunsicherheiten oder fehlenden Messungen zu machen. Durch die Kombination mehrerer Transportlöser mit unterschiedlichen Komplexitätsgraden und Rechenkosten in einem Multi-Fidelity-Ansatz kann die Zuverlässigkeit und Genauigkeit von IDA weiter verbessert werden. Diese umfassenderen Bemühungen erkennen die inhärenten Herausforderungen der Plasmadiagnostik an und zielen darauf ab, den Forschenden ein umfassendes Toolkit für die genaue Charakterisierung von Fusionsplasmen an die Hand zu geben.

Contents

1. Introduction

1.1. Fusion

With the increasing impact of the global climate crisis, there is a growing urgency to adopt carbon-neutral energy sources. These sources are essential to mitigate the additional release of CO_2 into the atmosphere and to minimize the greenhouse effect, particularly as the world's energy consumption continues to rise. Nuclear energy is a supplementary option to solar and wind energy for carbon-neutral power production. Currently, only nuclear fission reactors exist in which heavy isotopes such as enriched uranium are split. Nuclear reactors have the advantage over classic renewables of being continuous, but they require a much larger investment budget [1].

However, fission is not the only process through which nuclear energy can be produced.

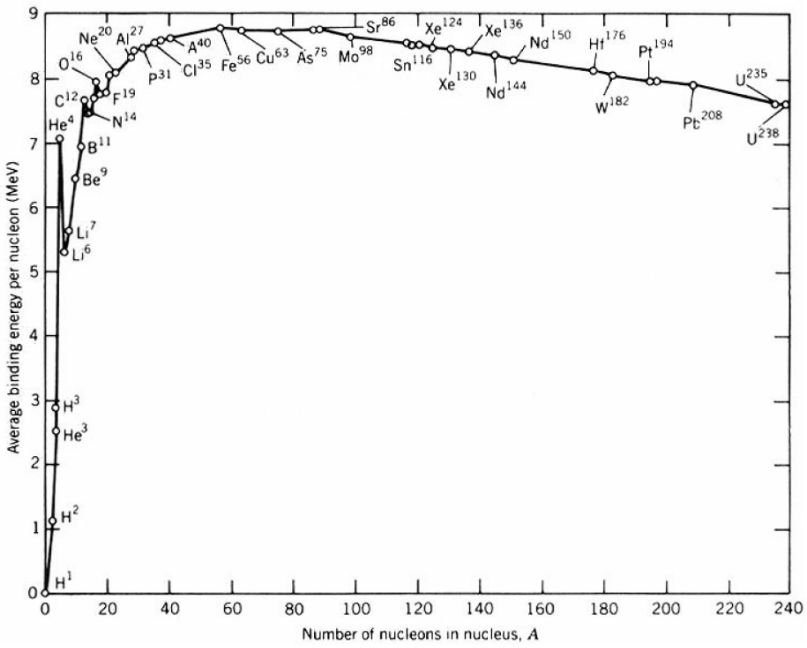

Figure 1.1.: Binding energy of different isotopes. The maximum at iron with A=56 means that to the left of it, energy can be gained via fusion, while to the right, fission gives off energy. Hydrogen isotopes have the largest delta in binding energy, which makes them interesting for power plants. Image taken from [2]

For nuclei with an atomic number below A=56, energy can be gained by atoms fusing, as can be seen in figure 1.1. Nuclear fusion is a process in which two light atomic nuclei

combine to form a heavier nucleus, releasing energy. In both fusion and fission have the advantage of having each reaction create energy in the MeV range and being CO_2-neutral, discounting for such processes as uranium mining and reactor construction. Chemical reactions, such as burning coal or gas, typically only release energies in the eV range, meaning significantly more fuel is needed to run than in a nuclear power plant. Fusion reactions are desirable compared to fission as the reactions do not create long-lived radioactive isotopes.

In contrast to nuclear fission, both reactants are positively charged, and thus, kinetic energy is needed for the isotopes to overcome the Coulomb barrier. Using thermal motion to bring the two isotopes together requires an optimal temperature of tens of keV ($\approx$ 100 million degrees Celsius) in a fully neutral ionized state called plasma. Most fusion projects explore the option of energy production through the fusion of two hydrogen isotopes, Deuterium and Tritium

$$^2D + ^3T \rightarrow ^4He + ^1n, \tag{1.1}$$

, which has the highest cross-section among reactor-relevant reactions. While deuterium is abundantly available, using tritium in a reactor has drawbacks, as it is difficult to produce and has a half-life of 12.3 years. The advantage is that the reaction cross-section is much higher than e.g. the long proton-chain fusion in the sun,

$$^1p + ^1p \rightarrow ^2D + e^+ + \nu_e \tag{1.2}$$

$$^2D + ^1p \rightarrow ^3He + \gamma \tag{1.3}$$

$$^3He + ^3He \rightarrow ^4He + ^1p + ^1p \tag{1.4}$$

$$\tag{1.5}$$

as D-T fusion is done via the strong interaction force only, and the combined rest mass is very close to ^5He, which creates a resonance [3]. While fusion does not produce long-lived radioactive materials, the fusion-born neutrons will activate parts of the reactor, meaning that these will have to be held for around 100 years [4]. In a fusion power plant, the neutrons produced by the DT fusion reaction would leave the plasma, provide the energy to heat water and provide electricity to the grid. Additionally, the neutrons are foreseen to interact with a lithium blanket to produce more tritium. The helium-ion called an alpha-particle, which receives 3.5 MeV of the produced energy, would provide additional heating to the plasma, resulting in a reduction of the required external heating once the plasma is in a self-sustaining chain reaction called *ignited*.

To achieve self-sustaining reactions in a fusion plasma, the heating of the plasma through α-particles has to be larger than the energy lost through radiation and particles leaving the plasma so that the heating becomes self-sustained. This state is called ignition and is reached when the triple product of ion density n_i, ion Temperature T_i and energy confinement time

$$\tau_E = W/P_{lost} \tag{1.6}$$

is high enough, with W being the stored energy and P_{lost} the lost power. The Lawson criterion [5], states the minimal threshold at which ignition is reached

$$n_i T_i \tau_E \geq 10^{22} m^{-3} keVs, \tag{1.7}$$

if impurities in the plasma are considered. Impurities, such as carbon, nitrogen, tungsten and the produced helium, dilute the hydrogen-isotope fuel and cause an increase in plasma power loss due to their higher radiation emission.

There are two main approaches to achieving ignition: inertial confinement fusion (ICF) and magnetically confined fusion (MCF). ICF uses high-power lasers to compress a D-T filled pellet, which would reach the desired triple-product by very high densities but small τ_e, similar to a hydrogen bomb. ICF has garnered a lot of interest with an experiment recently producing more energy than was deposited by the lasers compressing the pellet [6]. However, the path to a commercial fusion power plant using an ICF concept is still unclear.

MCF aims to have much larger confinement times compared to ICF. Similarly to the sun keeping its Hydrogen confined due to its large mass, MCF uses magnets to stop particles from escaping. The charged particles in the plasma will travel along the field lines due to the Lorentz-Force. For a single particle, the force is given by

$$F = q(\vec{v} \times \vec{B} + \vec{E}) \tag{1.8}$$

with $\vec{B}$ being the magnetic field, $\vec{E}$ an electric field, and $\vec{v}$ the the particle velocity. This means that the particle can travel freely along the magnetic field line in a helical trajectory with a radius of

$$r_L = mv_\perp / qB, \tag{1.9}$$

with q being the electric charge, $v_\perp$ the velocity perpendicular to the toroidal magnetic field B and the particles mass m. r_L is generally known as the Larmor radius. The cyclotron- or gyrofrequency ω_c is given by

$$\omega_c = \frac{qB}{m} \tag{1.10}$$

Early magnetic confinement devices such as magnetic mirrors aimed to confine the plasma by a strong magnetic gradient at either end of the machine, leading to particles being reflected (see the trapped particles in section 2.2.1). However, not enough particles were reflected for this to be a viable future reactor.

Nowadays, there are two main concepts for MCF reactors currently being explored: Tokamaks and stellarators. Stellarators achieve their magnetic fields solely by complex external magnets, with the advantage of continuous operation. Due to their complicated magnetic field geometry, stellarators are not yet as well developed and are achieving a smaller triple product than tokamaks, which are introduced in the next section.

1.2. Tokamaks

The MCF devices with the best triple-product record to date have all been tokamaks with reached confinement times in the order of seconds [7]. There are several exciting new experiments currently in construction. For example, the ITER tokamak in France [8] has been a major international collaboration work and is expected to yield ten times more energy than

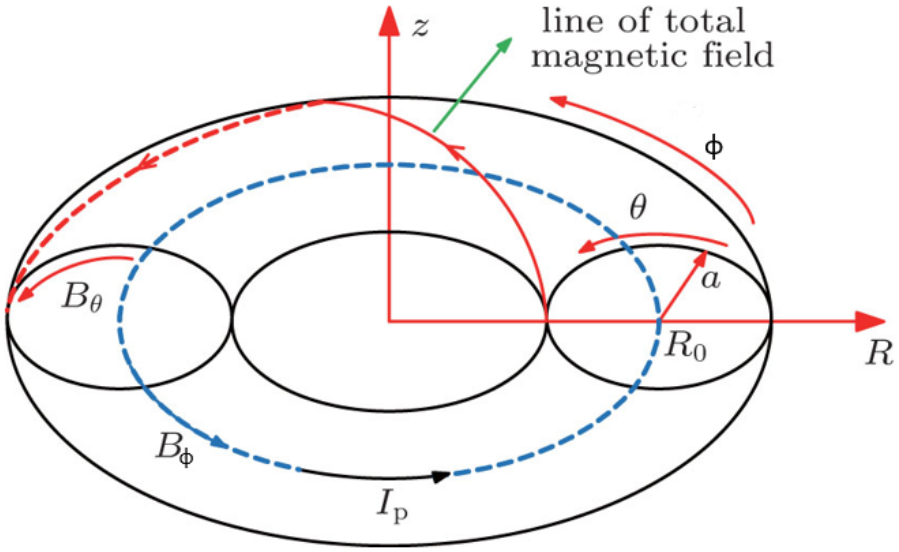

Figure 1.2.: Simple geometry of a tokamak with a circular cross-section. As a common practice, this thesis shall use r as the minor radii, with a being the minor radii at the plasma edge. The figure was taken from [10] with some altered notations.

is injected into the plasma as external heating power during its DT campaign. The startup "Commonwealth Fusion" is building a tokamak based on a stronger magnetic field achieved via high-temperature superconducting magnets [9], which they hope will make it possible to create a reactor with a smaller volume, thus decreasing the costs.

A tokamak uses axisymmetric magnetic fields to bend the plasma into a torus, as shown in figure 1.2, thus avoiding end-losses. A purely toroidal field gives rise to various drifts, which cause diminishing particle confinement. For example, the gradient of the magnetic field causes electrons and ions to drift in opposite directions

$$\vec{v}_{\nabla B} = \frac{m v_\perp^2}{2qB^3} \nabla B \times \vec{B}, \tag{1.11}$$

due to their different charge [11]. This charge separation creates an electric field, which generates a second drift

$$\vec{v}_{E\times B} = \frac{\vec{E} \times \vec{B}}{B^2} \tag{1.12}$$

leading to radial transport and thus loss of confinement.

To average out the drifts, the tokamak uses a helically wrapped magnetic field [12], similar to rotating a knife with honey to prevent it from dripping downward. The field is made by combining a toroidal field B_{tor}, which is formed externally by toroidal field coils, and a poloidal field B_{pol} being produced by a toroidal current in the plasma (see figure 1.2

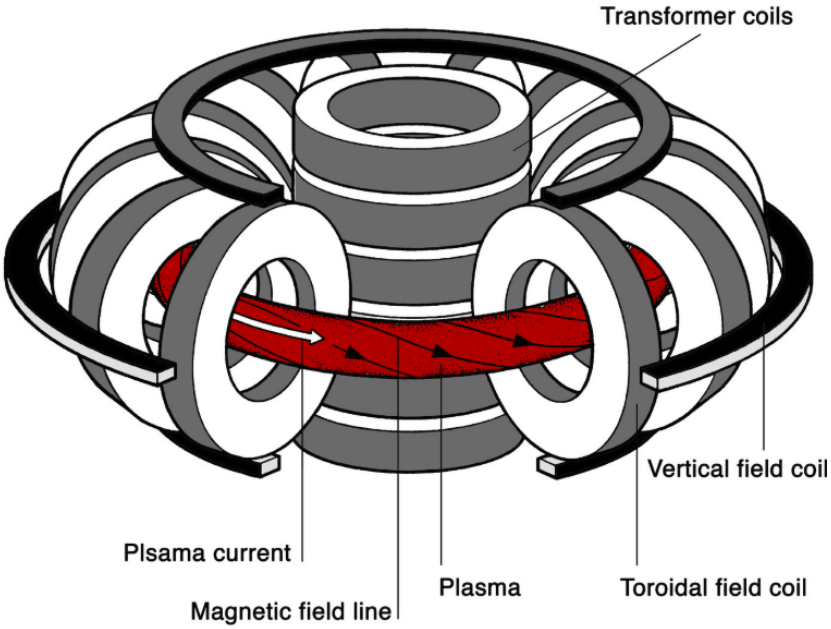

Figure 1.3.: The plasma follows the magnetic field lines, which are helical to protect the plasma from instabilities and confinement deteriorating drifts. The toroidal field coils create the toroidal component, while the poloidal component is formed via ramping the transformer coils' current. The vertical field coils are used to shape and control the plasma. Taken from [15].

for a coordinate system). Additionally, vertical poloidal field coils are used to counter the destabilizing *hoop-force* [13]. The toroidal current is formed via induction by decreasing a current running through the transformer coils called the central solenoid (see figure 1.3). As the solenoid current needs to be continuously decreased, it will reach a minimum current at some point, and the discharge has to end. While there are alternative methods of creating a toroidal current, such as electron cyclotron current drive (ECCD) [14], these use up energy, making a future reactor less efficient. Replacing the transformer current completely is still an active area of research. Thus, only pulsed operation is possible for now. The pulsed operation is a major drawback compared to a possible stellarator reactor.

The plasma can be broadly divided into three radial regions. The core, where particles travel on closed magnetic field lines, is comparatively easy to model as the fusion plasma has no contact with the device walls. The density and temperature are large as this is the region where fusion reactions will take place in a reactor. The scrape-off layer, where $r > a$, is the opposite where open field lines intersect with the machine, making it necessary to take plasma-material interactions into account. As the device walls are much colder than the plasma core, the plasma itself is cooler and often only partially ionized. The plasma boundary ($r \approx a$) combines the core and the edge regions with strong gradients in temperature and density. It plays a crucial role in plasma performance during the transition of different operational modes, as discussed below.

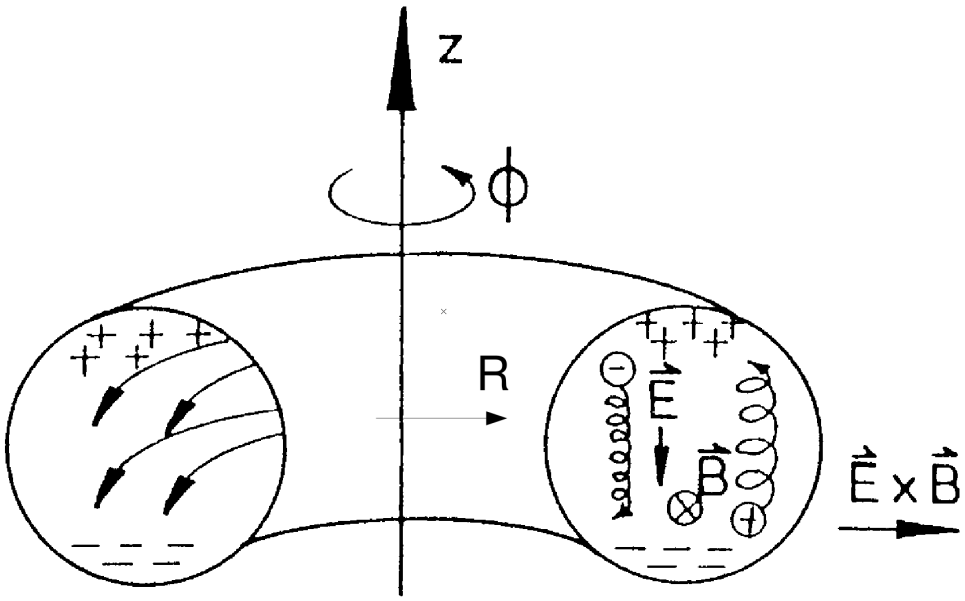

Figure 1.4.: Particle drift in a purely toroidal magnetic field. The curvature and ∇B drift lead to a charge separation, with ions moving upwards and electrons downward. As a result, an electric field acts on the particles, resulting in an outward drift. To average out this mechanism, a poloidal field is added. The $E \times B$ transport mechanism is also extremely relevant for turbulence.

1.3. Experimental profile fitting

Accurate information about plasma discharges in current devices is crucial for code validation and developing discharge scenarios for future tokamak power plants. To study the behavior of the fusion plasma, a host of diagnostics have been developed. The need to gauge different parameters such as currents, magnetic fields and plasma rotation means that a large portion of the experiment's budget and working hours are invested in the measurements. Due to the complexities of the plasma with its different regions, no single diagnostic can cover the entire plasma parameter space.
In a tokamak, one can view important parameters such as density and temperature as a 1D-radial profile assuming a local Maxwellian distribution. Traditionally, every diagnostic was analyzed separately, and a curve was fitted through the data points. This has the unwanted side-effect of different users using different assumptions and profiles and their uncertainty is hard to compare.

This thesis focuses on the IDA framework [16] used at the ASDEX Upgrade tokamak. IDA is capable of providing robust electron temperature and density profiles by combining the different diagnostics, non-physics-based priors and Bayesian probability theory (BPT). With proposed profiles, IDA will create synthetic data for each diagnostic and compare it to the actually measured data. This makes it possible to evaluate all diagnostics simultaneously, exploiting synergies and redundancies between diagnostics in this standardized evaluation.

The priors give information about the plasma without having seen the data by, for example, making assumptions about the monotonicity and smoothness of the profile. For every millisecond of an ASDEX Upgrade discharge, users receive the likeliest profile given the measurements and priors.

Even with its complex and fine-tuned capacities, due to incomplete plasma coverage by diagnostics and potential data corruption or unavailability, IDA profiles can exhibit gradients that contradict established transport theory's expectations. This problem will likely worsen in future reactors, as the neutrons will lead to a deterioration of the diagnostics [17].

1.4. Theoretical transport predictions

While a single particle would be perfectly confined in the tokamak, interacting with other particles leads to transport. It was first expected that transport in a tokamak would be mainly due to collisions. Today, the general consensus is that turbulent transport is the main limitation to the energy confinement time in the core. Turbulent microinstabilities are a result of the free energy present in the gradients of density and temperature profiles. Similarly to an avalanche on a snowy mountain, the gradients must cross a critical threshold to enter the turbulent state. While the plasma in a turbulent state is far from thermal equilibrium, a quasi-stationary state is reached by non-linear coupling between different modes. The non-linear aspect of turbulence means that high-fidelity *gyrokinetic* simulations, even with large advances in computing power, can need wall-clock time in the order of months to compute the temperature, density and electromagnetic fluctuations for a single radial position. The electrostatic and electromagnetic fluctuations again give rise to a $E \times B$ drift, leading to high fluxes.

While turbulence-driven transport usually dominates in fusion plasmas, it is possible to suppress the transport. This was first realized in the 1980s with the high-confinement mode (H-mode) [18], which creates a transport barrier at the edge of the plasma if given enough external heating. By having larger gradients at the edge, H-mode plasmas can have higher overall temperature and density values in the core than typical low-confinement mode (L-mode) discharges. While it is known how to access the operational space of a tokamak with transport barriers, the understanding of the complex physics and correct modeling is still actively researched.

Another limitation on confinement can be the reorganization of the magnetic field lines. In these cases, the magnetic field lines can be torn apart, leading to flat profiles in the area of the tearing mode.

1.5. Scope of this work

This thesis further improves the Integrated Data Analysis framework by combining the traditionally separated domains of experimental and theoretical knowledge. It introduces

a prior based on the predictive model ASTRA [19], which aims to bring IDA profiles into agreement with both experimental data and simulations. ASTRA is coupled with various heating subroutines as well as the gyrofluid quasi-linear turbulence code TGLF [20], which calculates fluxes on an order of seconds by various simplifications compared to gyrokinetic codes. The speed of TGLF comes at the cost of incomplete physics. For example, TGLF cannot correctly model the transport reduction during H-mode, where magnetohydrodynamic limits govern the physics. Together, ASTRA-TGLF simulates density and temperature profiles for various equilibria and heating schemes. While the edge and magnetic axis are still difficult to simulate by the presented model, ASTRA-TGLF is well-validated and can find good agreement with experiments at the mid-radius.

New IDA profiles are calculated by implementing the ASTRA-TGLF simulations as another prior, which is equivalent to viewing it as a synthetic diagnostic from a Bayesian viewpoint. The new profiles are validated by comparing fluxes obtained from the TGLF with the power balance obtained by integrating over the heating sources. To prevent the kinetic model (KM) from dominating experimental data in the IDA framework, the residuals between profile and measurement data are examined. This thesis finds that IDA with the kinetic modeling prior has improved gradients without negatively impacting the match to experimental measurements.

As ASTRA-TGLF is deterministic, no likelihood or uncertainty of the simulation is given. In this thesis, the dependence of the model on its inputs, as well as the systematic errors of TGLF, are explored.

The thesis continues as follows:

- **Chapter 2** gives the reader a brief overview of tokamak physics, starting with the equilibrium. The reader is further introduced to diffusive transport and turbulent microinstabilities that limit tokamak performance and are driven by profile gradients. The chapter closes with the different codes used in the thesis. The ASTRA framework with its various subroutines, as well as the build-up of the used ASTRA kinetic model, is explained. The high-fidelity gyrokinetic turbulence code GENE and the lower-fidelity TGLF follow this. As TGLF is crucial to the thesis, a brief literary overview of previous work validating TGLF on multiple tokamaks and plasma scenarios is presented.

- **Chapter 3** presents the ASDEX Upgrade (AUG) tokamak and some basic information on the most used diagnostics to fit temperature and density profiles, followed by different heating schemes used in the discharges and simulations. The IDA framework, along with its uncertainty quantification, is discussed in some detail as well as other Bayesian fitting procedures used at AUG.

- **Chapter 4** shows concepts and results of uncertainty quantification work utilizing the ASTRA-TGLF model. Error estimations are needed to define the Likelihoods of the simulated profiles for the kinetic modeling prior. As a proof-of-concept work, predefined uncertainties are used for different plasma regions, which are used for the results shown in Chapter 7. These uncertainties are to be replaced with some of the

methods described in the chapter, which include sensitivity analysis such as input uncertainty propagation and polynomial chaos expansion.

- **Chapter 5**: After a quick overview of the kinetic modeling prior's implementation in IDA, results of L- and H-mode discharges are shown. A use-case of IDA with the kinetic modeling prior is presented, in which the new profiles would save computational time when running expensive gyrokinetic simulations. While it is generally desired to have the new IDA profiles match the simulations, it is imperative that the kinetic model does not dominate over the experimental data in case the physics are not correctly simulated. These cases are exemplified in a discharge with an internal transport barrier and a discharge with a large tearing mode.
- **Chapter 6**: The thesis concludes by presenting further turbulence models available in ASTRA as well as alternatives for faster modeling. It also presents utilizing the new prior on an entire discharge.
- **Chapter 7**: Summary and outlook to future work

2. Theoretical background

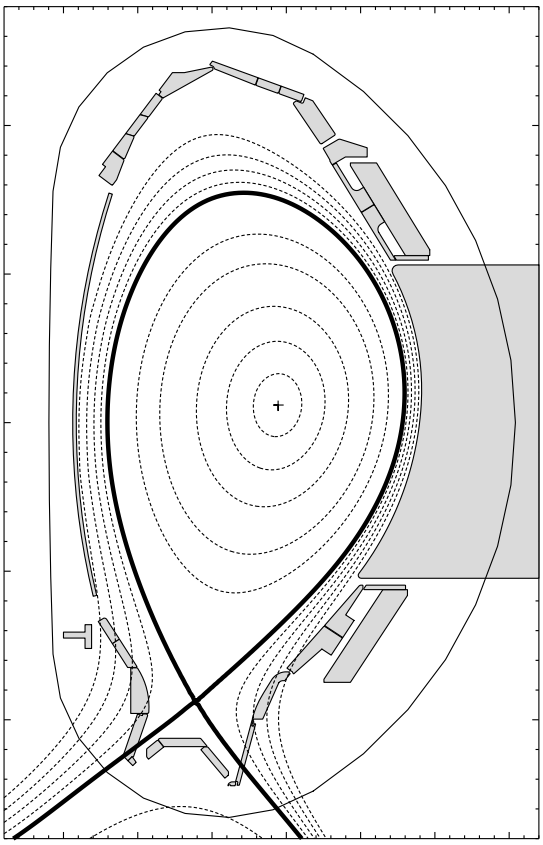

Figure 2.1.: Flux surfaces of a typical diverted plasma at AUG in a lower single null configuration. One can assume constant pressure on the flux surfaces indicated by the dotted lines. The scrape-off layer region begins outside of the separatrix (solid line), where open magnetic field lines end in the divertor.

Until now, the thesis has only introduced the forces acting on an individual particle in a magnetic field. The particles are confined to follow a magnetic field line unless a further force acts upon them, leading to drifts.

However, when dealing with fusion plasmas, the situation changes. Collisions between particles must be considered, which can cause radial displacements. This introduces radial fluxes due to the presence of gradients in the plasma. Early fusion experiments in the latter half of the 20th century revealed that radial transport is significantly higher than expected based solely on collisional theory. This mysterious observation was initially termed "anomalous transport" until it was eventually attributed to turbulence induced by gradient-driven micro-instabilities. This transport of heat and particles out of the plasma sets limitations on the maximum attainable gradients in temperature and density, which limits the achievable triple product.

In this chapter, the plasma equilibrium will be introduced, followed by transport from collisions as well as turbulence. The chapter will end with the models used to predict the kinetic profiles in this thesis, including the codes used to study turbulence.

2.1. Plasma equilibrium

Magnetohydrodynamics (MHD) describe the behavior and form of the plasma as a single conducting fluid in the presence of a magnetic field. This fluid description helps avoid solving

the Lorentz force for every ion and electron in the plasma. Instead, the plasma is described by a distribution function f in a six-dimensional space. The kinetic equation acts on the distribution function

$$\frac{\partial}{\partial t}f + v \cdot \nabla f + q/m(E + v \times B) \cdot \nabla_v f(r, v) = (\frac{\partial f}{\partial t})_{coll}. \tag{2.1}$$

In MHD, one can assume that f is a Maxwellian, as the distribution will be close to thermodynamic equilibrium due to the collision operator. This will not be the when studying turbulence in later sections. Here, one can assume that the ions carry the mass and momentum ($\rho \approx n \cdot m_i$), as protons are around 1800 times heavier than electrons. The current is given by the electron's velocity difference to the ions. The MHD equations [12] are

$$\text{continuity eq. } \frac{\partial \rho}{\partial t} = -\nabla(\rho \vec{v}) \tag{2.2}$$

$$\text{momentum eq. } \rho\left(\frac{\partial v}{\partial t} + \vec{v} \cdot \nabla \vec{v}\right) = -\nabla \vec{P} + \vec{j} \times \vec{B} \tag{2.3}$$

$$\text{adiabatic eq. } \frac{d}{dt}\left(\frac{P}{\rho^\gamma}\right) = 0 \tag{2.4}$$

$$\text{Maxwell} - \text{Faraday eq. } \nabla \times \vec{E} = -\frac{\partial \vec{B}}{\partial t} \tag{2.5}$$

$$\text{Ampre}'\text{s Law } \nabla \times \vec{B} = \mu_0 \vec{j} \tag{2.6}$$

$$\text{No magnetic monopoles } \nabla \cdot \vec{B} = 0 \tag{2.7}$$

$$\text{Ohm}'\text{s law } \vec{j} = \sigma(\vec{E} + \vec{v} \times \vec{B}). \tag{2.8}$$

In the magneto-static limit, the left side of the momentum equation is 0, thus leading to

$$\nabla p = \vec{j} \times \vec{B}. \tag{2.9}$$

One finds that the magnetic field lines are enclosed within concentric magnetic surfaces characterized by constant pressure by multiplying both sides with the magnetic field

$$\nabla p \cdot \vec{B} = 0. \tag{2.10}$$

First tokamak experiments used a circular geometry, in which only the magnetic axis had zero poloidal magnetic field and the separatrix had contact with the *limiter* wall. Later it was found that shaping the plasma into a more elongated and triangular form and creating an additional point in which the poloidal field is zero gave better performance. The elongation κ and upper and lower triangularity $\delta_{u,l}$ is given by

$$\kappa = \frac{Z_{\max} - Z_{\min}}{R_{\max} - R_{\min}} \tag{2.11}$$

$$\delta_{u,l} = \frac{R_{\max} + R_{\min} - 2R\left(Z_{\max,\min}\right)}{R_{\max} - R_{\min}}. \tag{2.12}$$

As shown in figures 2.1 and 2.2, the flux surfaces become elongated and triangular until the last closed flux surface, which is called the separatrix. At the lower end of the separatrix is the *X-point* which has no poloidal magnetic field. A big advantage of this configuration is that any particles that leave the separatrix into the scrape-off layer are transported along open field lines towards the divertor, whose target plates can be cooled to handle large heat loads. At the divertor, neutrals can be pumped out, which leads to fewer impurities than in a "limited" plasma. The specific shape of the magnetic field lines assuming toroidal axisymmetry is given by the Grad-Shafranov equation

$$\Delta^* \Psi = R^2 \nabla \frac{\nabla \Psi}{R^2} = -\mu_0 2\pi R j_\phi = -\mu_0 (2\pi R)^2 p' - \mu_0^2, I'_{pol} I_{pol} \tag{2.13}$$

where Ψ is the poloidal magnetic flux, I_{pol} the poloidal current, j_ϕ the toroidal current density and derivatives with respect to Ψ are denoted with a $'$. As the elongation of the plasma makes using the minor radius of the plasma an oversimplification, the changing poloidal and toroidal flux is often used as a radial coordinate

$$\begin{aligned} \rho_{tor} &= \sqrt{\frac{\Phi - \Phi_0}{\Phi_{Sep} - \Phi_0}} \\ \rho_{pol} &= \sqrt{\frac{\Psi - \Psi_0}{\Psi_{Sep} - \Psi_0}}, \end{aligned} \tag{2.14}$$

where Φ is the toroidal flux. Both coordinates are equal to one at the last closed flux surface called separatrix (Sep) and 0 at the magnetic center. The toroidal magnetic field is zero outside of the toroidal field coils, but ρ_{tor} becomes ambiguous outside the last closed flux surface for diverted plasmas [13]. Thus, ρ_{tor} is only defined up to 1, but theoretically, the ρ_{pol} has no upper limit.

The equilibrium is important for this work as it not only maps lines-of-sight for different diagnostics onto a common coordinate system but also as transport along the field lines is almost instantaneous, one can assume that temperature and density are constant on the nested flux surfaces and thus for the same ρ_{tor}.

If a magnetic confinement device were to be run with a purely poloidal field, it would be subject to kink and sausage instabilities [13]. Reducing the helicity can make the plasma "safer" and thus, the helicity is usually expressed as the safety factor q

$$q = \frac{\Delta \phi}{\Delta \Phi} \approx \frac{r B_{tor}}{R B_\Phi} \tag{2.15}$$

If the safety factor is larger than 1 for the plasma, it should be safe from the aforementioned instabilities. As the toroidal current decreases with increasing minor radius, the helicity of the plasma also decreases, leading to an infinitely high q at the separatrix. For a more useful quantity, the edge q value is usually given as the value at 95% of the poloidal flux q_{95}.

When q has a rational value, the field line reconnects to itself after $q = \frac{m=\#toroidalturns}{n=\#poloidalturns}$, which means that perturbations will travel along the field lines and self-amplify, creating instabilities. For example, the q=1 sawtooth instability leads to a periodic loss of confinement in the core, thus flattening the temperature and density profiles (see also section 2.3.4).

2.2. Plasma transport

A change in density is either given by the sources and sinks S or particle flux $\vec{\Gamma}$ leading to the density continuity equation

$$\frac{\partial n}{\partial t} = -\nabla\vec{\Gamma} + S \tag{2.16}$$

The density flux can be described as the sum of a diffusive term that acts against the gradient and a part connected to transport velocities due to convection or drifts.

$$\vec{\Gamma} = -D\nabla n + v\vec{n} \tag{2.17}$$

Similarly, the continuity equation of plasma energy W is

$$\frac{dW_{Plasma}}{dt} = P - \nabla(\vec{q} + \frac{3}{2}k_B T\vec{\Gamma}) \tag{2.18}$$

with P being the sources and sinks of the Plasma and q the heat flux due to a temperature gradient. Fourier's law for thermal conduction

$$\vec{q} = -n\chi\nabla T, \tag{2.19}$$

means the temperature and density profiles can be predicted as long as the thermal and particle diffusivity χ and D and sources are known.

2.2.1. Collisional transport

As single particles are limited to circling around the magnetic field line, single electrons and ions would not experience perpendicular transport by themselves. When fusion experiments were first started, it was assumed that the main transport mechanism would be collisional transport. In a random walk mechanism, one can assume that the average perpendicular displacement is similar to the Larmor radius yielding [11]:

$$D = \frac{\Delta x^2}{\Delta t} = r_L\nu, \tag{2.20}$$

with $\nu \propto T^{-3/2}$ being the collision frequency. Similiar thoughts can be used to determine the classical χ with $\chi_i = D\sqrt{m_i/m_e}$. However, experiments showed transport several orders of magnitude higher than expected through the simple random walk model.

A better approximation is achieved if the length scale of the random walk is increased to the size of banana orbits using neoclassical theory. As the magnetic field has a radial gradient,

particles following the helically twisted magnetic field will experience varying magnetic field strengths ($B \propto 1/R$). The charged particle has a constant magnetic moment ($\mu \propto v_\perp^2 / B$) and energy ($E \propto v^2 = v_\perp^2 + v_\parallel^2$). If the parallel velocity is too small, the charged particle will bounce back toward the low magnetic field direction instead and are called trapped to the low field side (LFS), and their path looks like a banana in a poloidal cross-section (see figure 2.2. The condition in which a particle is trapped in a low aspect ratio tokamak, meaning that $\epsilon = r/R_0 \ll 1$, is

$$\frac{B_{max}}{B_{min}} - 1 = \frac{(R_0 + r)}{(R_0 - r)} - 1 \approx 2\epsilon \geq \frac{v_{\parallel,LFS}^2}{v_{\perp,LFS}^2} \tag{2.21}$$

The trapped particle fraction is about $\frac{n_t}{n} \approx \sqrt{2\epsilon}$. These trapped particles experience much stronger radial variations than the Larmor radius as the banana trajectory is

$$\omega_B = \approx r_L \frac{q}{\sqrt{\epsilon}}. \tag{2.22}$$

Using the banana width as the random walk step and considering a higher effective collision frequency, the diffusion coefficient increases,

$$D_{neoclassical} = \frac{q^2}{\epsilon^{3/2}} D_{classical}, \tag{2.23}$$

by about a factor 100.

Neoclassical transport is still too small by a factor of 10 for electrons in the core. Still, it does play an important role for deuterium and electrons close to the separatrix and the transport of impurities.

In analogy to the diamagnetic current, the density gradient leads to the neoclassical transport not averaging out toroidally. In figure 2.2, where the green and purple bananas intersect, there are more particles traveling upwards as the green banana has a higher density. This creates a toroidal current called the *bootstrap current*. The bootstrap current is important as it and auxiliary current sources can minimize the transformer's current and prolong the discharge length. It can be approximated by

$$j_{bs} \approx \frac{dp}{dr} \frac{\sqrt{\epsilon}}{B_\theta} \tag{2.24}$$

Additionally, the toroidal electric field required for generating plasma current influences trapped particle trajectories. This field accelerates particles parallel to magnetic field lines, causing banana particles to have varying kinetic energies as they move towards their reflection points in parallel or antiparallel directions to the electric field. As a result, banana orbits tilt, leading to a net inward drift of particles toward the magnetic axis. This drift is called *Ware-pinch* [11].

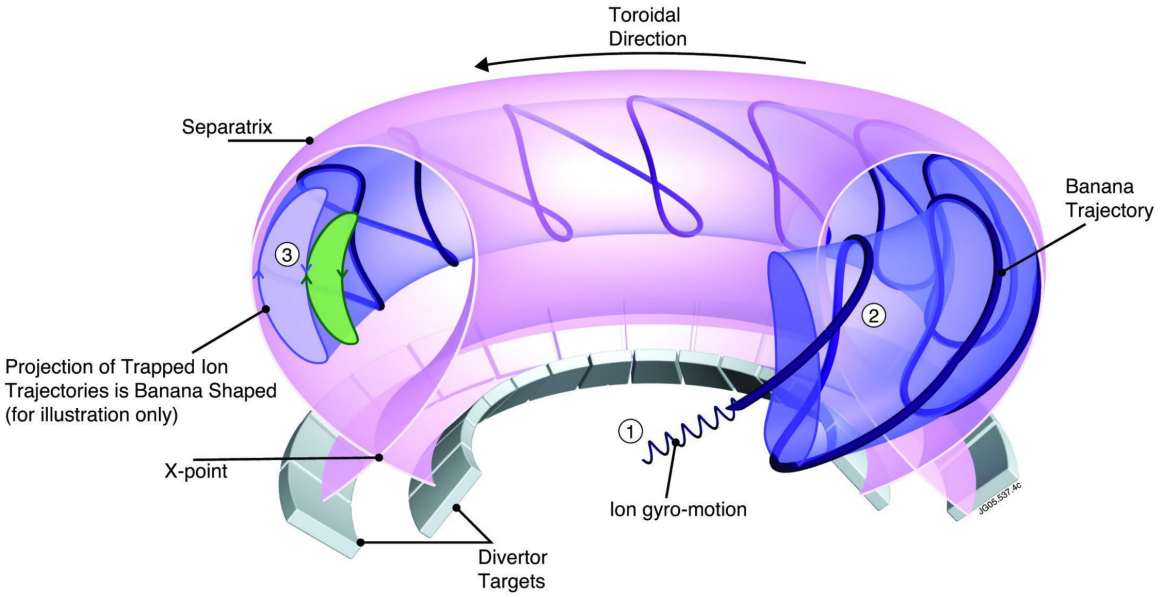

Figure 2.2.: Figure showing a tokamak plasma with a lower single null configuration. At ① one can see an ion gyrating along a trapped ion trajectory. As its velocity parallel to the magnetic field is too small, the particle follows a banana orbit ②. ③ shows the orbit in poloidal cross-section. Taken from [21].

2.3. Plasma turbulence

Turbulent transport is the dominant transport mechanism for ions and electrons in the core. As temperature and density gradients rise, they give free energy to micro-instabilities [22], which severely limit the profile's steepness and thus, the ability to achieve a high tripel product.

In a tokamak, as transport along the field lines is almost instantaneous, the turbulent fluctuations can be viewed as close to 2-dimensional [23]. As can be seen in figure 2.3, while in 3D, energy injected is carried to the small scales and then dissipated, in 2D the energy is carried to larger scales, while the conserved enstrophy $= \nabla \times v$ is carried to smaller scales. This energy flow to the large scales can lead to the appearance of low-frequency turbulent structures such as zonal flows [24]. Turbulence in the atmosphere is also a mainly 2D process with famous zonal flows such as Jupiter's great red spot. These flows can tear smaller eddies apart and thus stabilize turbulence. The need to model both small and large scales adds to the complexity of the problem, which usually needs supercomputing to be properly resolved.

Below, three important types of electrostatic turbulent plasma micro-instabilities are described. Refer to [24, 25] for a more complete list.

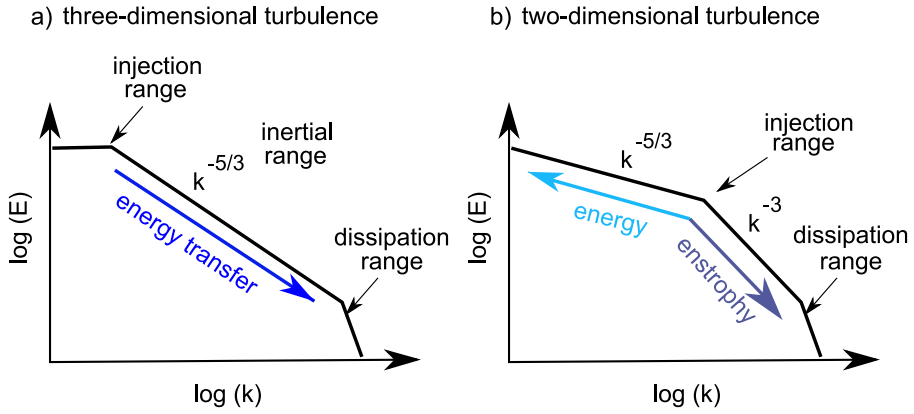

Figure 2.3.: Kinetic energy spectra of three-dimensional (a) and two-dimensional (b) fluid turbulence, as theorized by Kolmogorov and Kraichnan, respectively. Taken from [24].

2.3.1. Ion and electron temperature gradient-driven turbulence

The Ion temperature gradient (ITG) driven turbulent instabilities modes follow the principle of an interchange instability. The Electron temperature gradient (ETG) can be described with the same principle but with the roles of the ions and electrons exchanged. As the electron Larmor radius is much smaller than that of the ion the characteristic lengths ITG are also much larger than that of the ETG.

The interchange instability occurs at the low-field side of the tokamak, where the temperature and magnetic gradients point in the same direction. Figure 2.4 shows the development of the ITG turbulence. A periodic perturbation on the low field side leads to different temperatures (black solid line) on the potential field line (red dotted line). The combination of ∇B and curvature drift:

$$\vec{v_D} = -\frac{m(v_\parallel^2 + v_\perp^2/2)}{qB^3} B \times \nabla B \tag{2.25}$$

is faster for higher temperatures ($v^2 \approx v_{thermal}^2$), meaning that more ions travel upwards and electrons downwards in the high-pressure area. The resulting charge accumulation creates electric fields. The $\vec{E} \times \vec{B}$ drift will then push the hot plasma outwards and pull cold plasma inwards.

If one redoes the figures on the high field side, where temperature and magnetic field gradients are antiparallel, one can see that the electron diamagnetic drift is now pointing upwards, which leads to opposite electric fields compared to figure 2.4. The $\vec{E} \times \vec{B}$ drift here stabilizes the initial perturbation and transport is damped. The ITG is driven by ∇T_i and stabilized by ∇n_e (see equation 2.28).

2.3.2. Trapped electron mode turbulence

The trapped electron mode (TEM) has a drift wave mechanism and thus has to be viewed in 3D. An initial perturbation parallel to the magnetic field causes a difference in pressure.

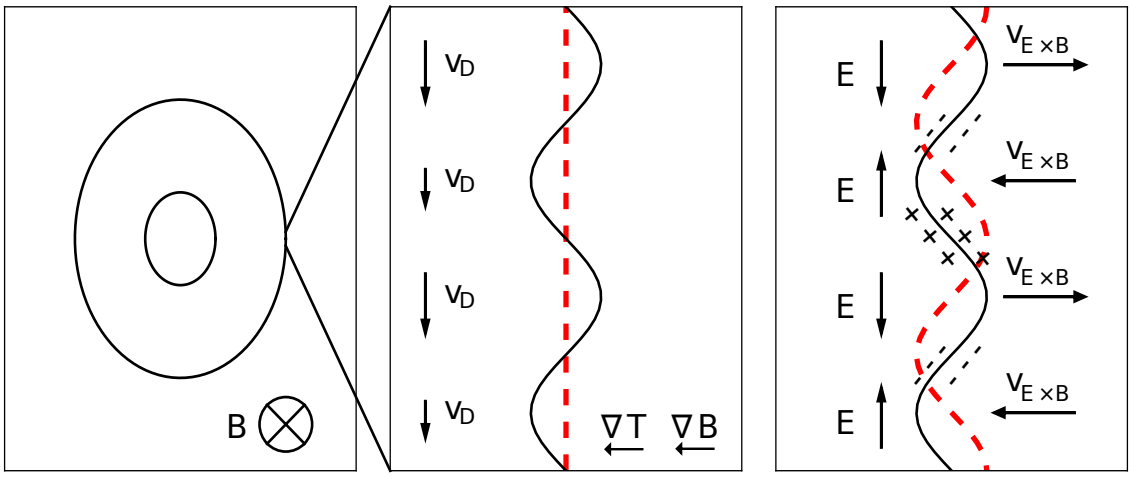

Figure 2.4.: Overview of the ITG mode development. An initial perturbation causes different drift speeds along the flux surface $v_D \propto \nabla p$ with the velocity direction plotted for electrons. The drift difference leads to a charge separation which exacerbates the disturbance. Figure taken from [26] with some modifications.

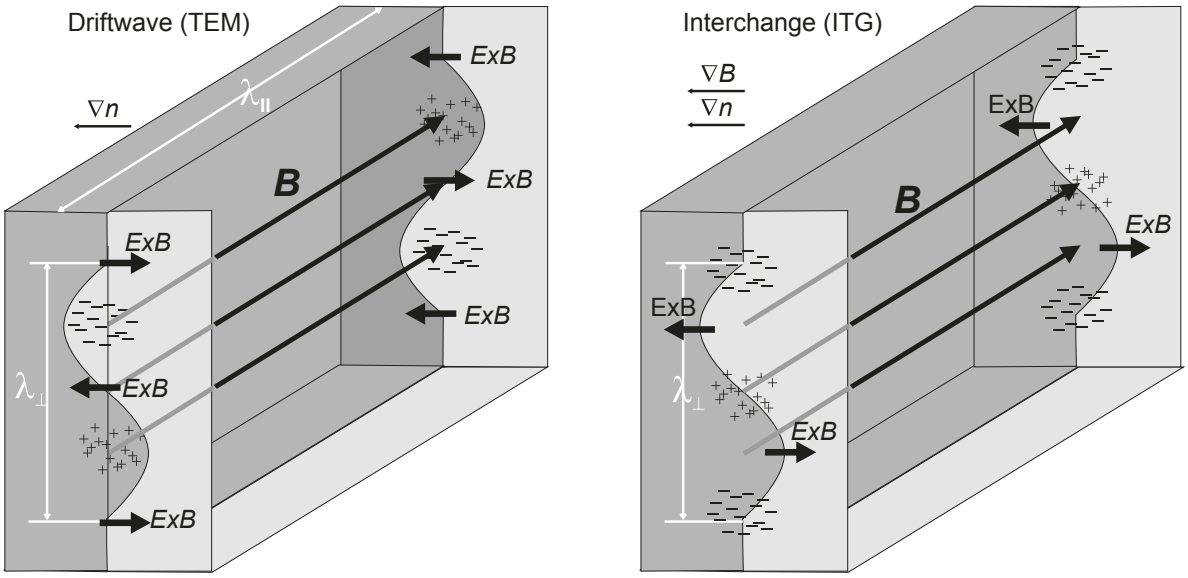

Figure 2.5.: 3d models of interchange and drift wave instabilities. In contrast to the ITG interchange instability, the driftwave TEM also has a perturbation parallel to the magnetic field. In the figure the density and potential are in phase, thus moving the perturbation in the diamagnetic drift direction and not causing any transport. Taken from [11] with some minor modifications.

Because of the fast transport along the magnetic field, one can assume the parallel perturbation length to be larger than perpendicular to the magnetic field $\lambda_{\parallel} \gg \lambda_{\perp}$. The electrons are much lighter than the ions, and they move to lower-pressure regions instantaneously, with the potential perturbation being equal to the electron perturbation. In this case, the electrons are called adiabatic electrons. The charge separation creates an electric field and the $E \times B$ drift. In figure 2.5, one can see that the $E \times B$ drift for the drift wave is such that no transport occurs. The drift merely forces the initial perturbation in the diamagnetic drift direction (downwards in the figure) as the density and potential are in phase. If, however, the electrons are no longer adiabatic, the perturbation and potential are no longer in phase, thus leading to transport. The trapped electrons mentioned in section 2.2.1 are not free to adiabatically move, thus leading to an important source of turbulent transport in a tokamak. Other reasons for not being in phase could be high collisionality, induction or Landau damping [27].

While ITG turbulence is often the dominant turbulence form in the fusion plasma core TEMs are usually subdominant, making it important to model them to properly capture the physics of a discharge. TEMs are driven by both electron density and temperature gradients.

One can tell the different simulated turbulent modes apart by studying the turbulent eddies' characteristic size and propagation direction as well as the mode's structure and cross-phase between the different fluctuations. ITG propagate in ion-diamagnetic drift direction and have a $k_y\rho_s = \frac{2\pi}{\lambda_y}\rho_s \leq 1$, while TEM and ETG propagate in the electron diamagnetic direction. TEM have a characteristic length $k_y\rho_s \approx 1$ while ETG of $k_y\rho_s > 1$ in the plasma core, with

$$\rho_s = \sqrt{\frac{T_e m_i}{eB}} \tag{2.26}$$

being known as the hybrid Larmor-radius. An example of the different growth rates for an ITG-dominated L-mode discharge can be seen in figure 2.6. The exact saturated electrostatic potential $|\tilde{\phi}|$ is either calculated by non-linear interactions or by a saturation rule. For simplicity, one can estimate the flux coming from k_y by the argument that the diffusive coefficient is made up of a distinctive time-step ($\Delta t = \frac{1}{\gamma_k}$) and length ($\Delta x = \frac{1}{k_y}$) [28, 29]. With equation 2.20, the diffusion is

$$D_k \propto |\tilde{\phi}| \propto \frac{\gamma_k}{k_y^2} \tag{2.27}$$

2.3.3. Critical gradients

The fusion plasma is not immediately turbulent. Rather there is a critical gradient beyond which the turbulence starts, and increasing the temperature or density gradients vastly increases transport. This fast rise in transport, as seen in figure 2.7, means that at a certain point, increasing the heating will hardly increase the plasma's temperature as the turbulence is too strong. In this case, the profile is called stiff.

In [31] the critical gradient for ETG turbulence was derived to be:

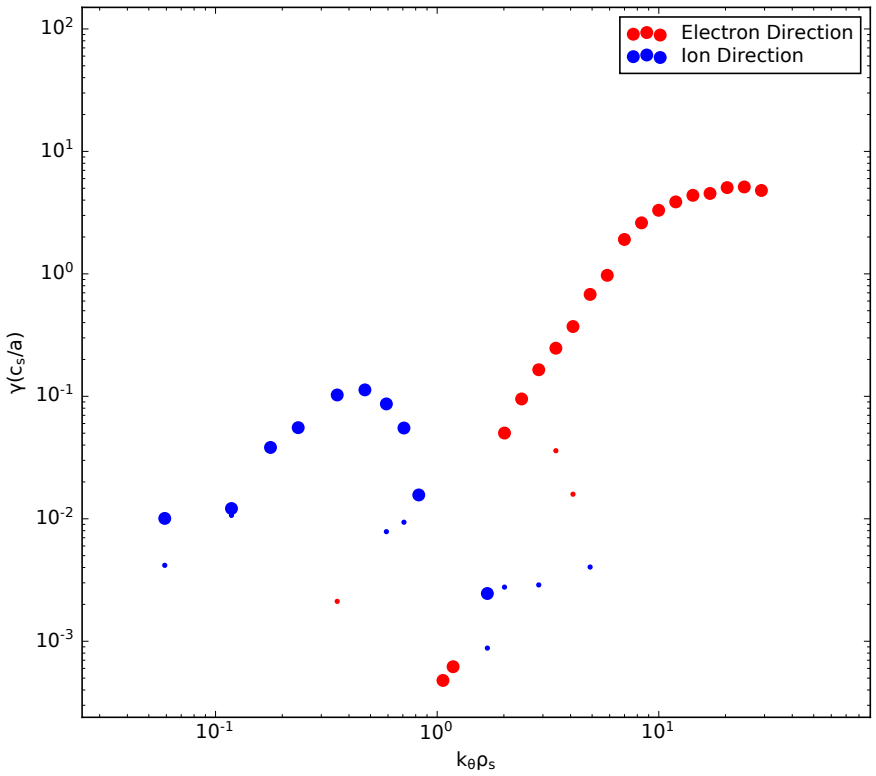

Figure 2.6.: Growthrates for a discharge dominated by ITG and TEM turbulence calculated by TGLF using Omfit [30]. The perturbed electrostatic potential for each wavenumber is approximated by γ/k_y^2. This gives an estimate of which wavenumber contributes most to the heat and particle flux.

$$R/L_{T_e} = max\{(1+\frac{T_e}{T_i})(1.33+1.91\frac{\hat{s}}{q})(1-1.5\epsilon)[1+0.3\epsilon(d\kappa/d\epsilon)], 0.8R/L_{n_e}\} \tag{2.28}$$

with $R/L_{T_e} = -\frac{R}{T_e}\nabla T_e = -R\nabla ln(T_e)$ being the normalized temperature log gradient. The formula also holds true for ITG if one switches T_e with T_i. Because of 3d effects, it is possible to increase the critical gradient by a larger density gradient or by, for example, changing $\frac{T_i}{T_e}$. For more information, [24] is referred to. For the TEM, a critical gradient was found in [32]:

$$R/L_{T_e,crit} \approx \frac{0.357\sqrt{\epsilon}+0.271}{\sqrt{\epsilon}}[4.90-1.31R/L_n+2.68\hat{s}+ln(1+20\nu_{eff})] \tag{2.29}$$

This matches the expectation that density gradients drive TEM activity. The epsilon dependence can be understood that towards the plasma center, the critical gradient becomes larger as the trapped particle fraction becomes smaller.
When taking non-linear interactions between different turbulent wavenumbers into account, the critical gradient was found to be raised due to zonal flows. This effect is called the *Dimit's shift* after the discovery in [33].

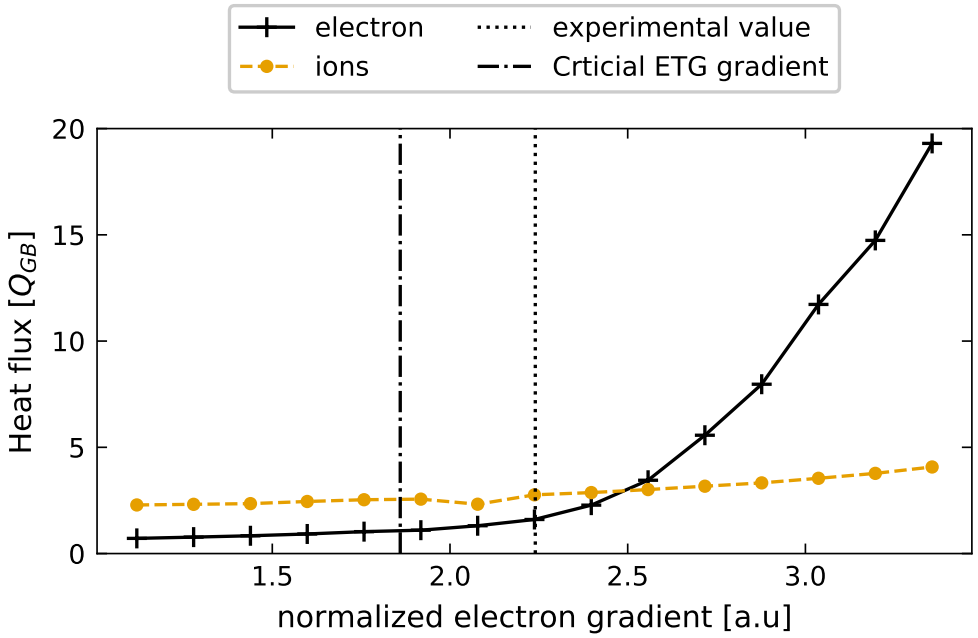

Figure 2.7.: Scan of electron temperature gradient using TGLF and Omfit. After the critical gradient is reached, the electron heat flux rises fast as the profile gets stiffer. This means that a small change in gradient has a large effect on the flux. The critical gradient for ETG is below the experimentally observed value, although ITG and TEM modes were found to be dominant. The critical gradient formulas used several assumptions to be calculated, so should only be taken as a first estimate where the turbulent regime starts.

2.3.4. Further effects on confinement

Transport barriers

While the transport is usually stiff, transport barriers can be created that suppress the turbulent transport. By using a divertor configuration and providing enough heating at the ASDEX tokamak an Edge transport barrier (ETB) was discovered [18]. The ETB leads to an increase of the confinement time of about a factor 2 and is called "high confinement operational mode" (H-mode).

H-mode plasmas have now been recreated in various tokamaks and are the desired running state for ITER. An exact physics model is still not quite available, but there is a consensus that shear in the $E \times B$ velocity is the main driver [34, 35]. The steep gradient at the edge leads to a pedestal in both temperature and density, leading to a strong increase in absolute values. An example can be seen for #33616 in figure 2.8, where the density roughly doubles at the edge and the temperature also strongly increases. The log gradients at mid-radius are however comparable.

This increase in performance comes with a cost. The pressure is periodically reduced with so-called edge-localized modes (ELM). Due to large pressure gradients at the edge,

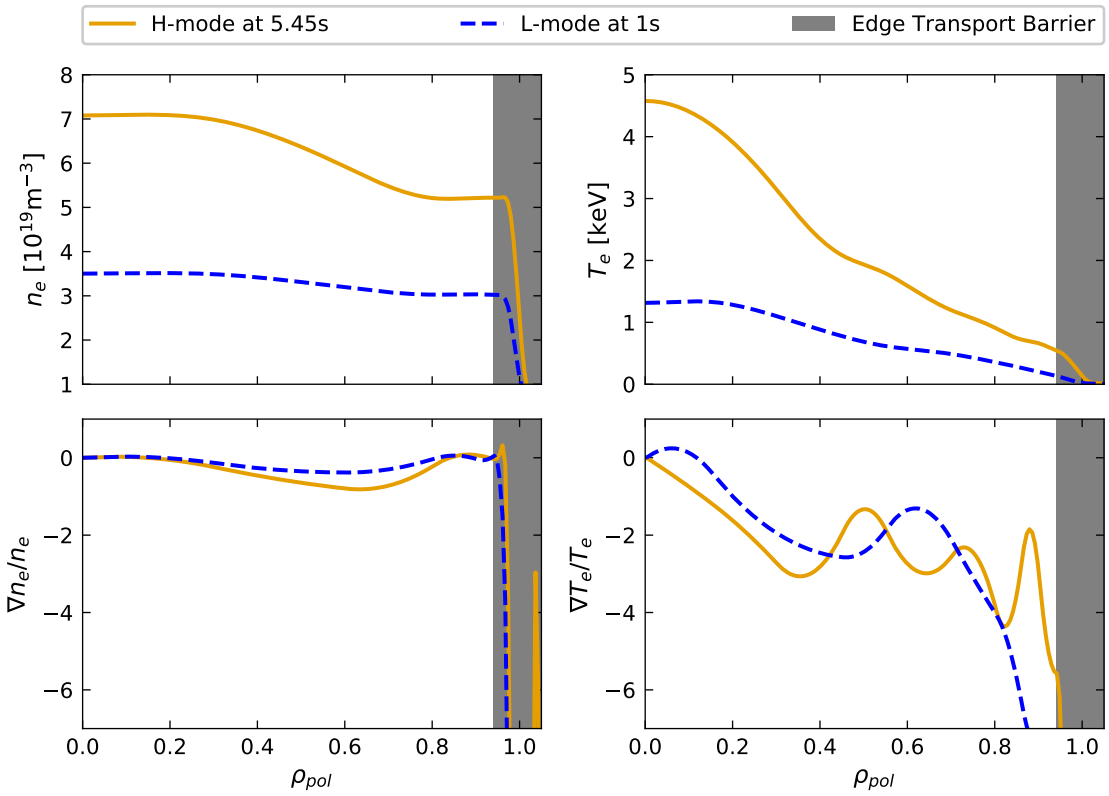

Figure 2.8.: Difference between the H-mode and L-mode phases of discharge #33616. While the log gradients are similar for most of the plasma, the edge transport barrier raises temperature and density, which propagates to the core.

ballooning modes are excited on the low field side. These can interact with peeling modes stemming from the strong current gradients, giving rise to *peeling-ballooning modes* [13]. These are thought to be the mechanism behind the ELM, which can expel up to 15% of the plasma's energy.

While these instabilities are tolerable in today's machines, extrapolating to the size of future fusion reactors will make the heat loads of the ELM disastrous. Much research is going into achieving operational modes with higher confinement that either avoid ELMs or are able to mitigate their power. ELM simulations are an active area of research with [36] having just achieved modelling of elm cycles.

With the right conditions Internal transport barrier (ITB) of fusion plasmas have also been achieved. The creation of ITBs is also not yet completely understood, with a combination of increased $E \times B$ shear and interaction with fast particles being likely candidates.

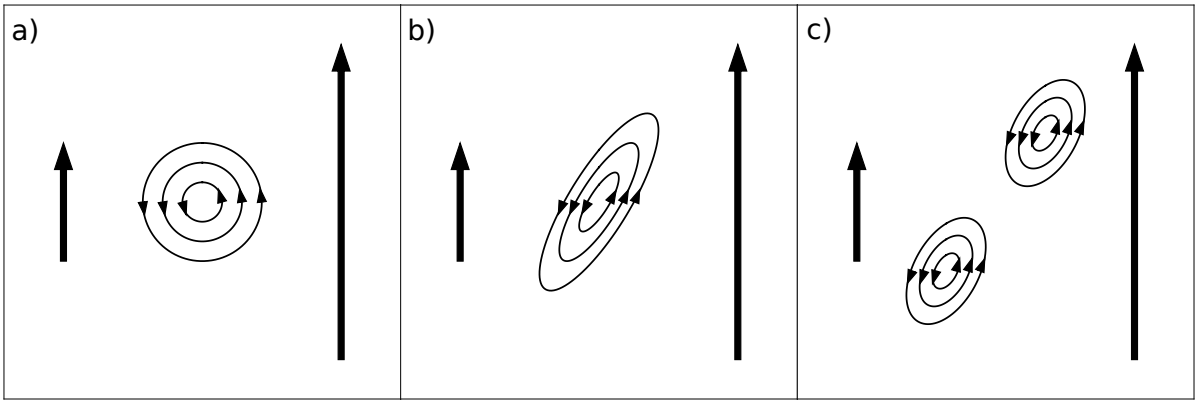

Figure 2.9.: A schematic illustration of turbulence suppression by velocity shear. The presence of a shear in the background velocity (depicted by black arrows) causes a deformation and eventual decorrelation of turbulence eddies. This deformation leads to a reduction in the distance particles can be transported by these eddies. Figure taken from [21]

$E \times B$ and magnetic shear

$E \times B$ shear is understood to suppress turbulence by the different drift velocities

$$v_{E\times B} = \frac{E \times B}{B^2} \tag{2.30}$$

on neighboring flux surfaces. The shear in velocity first elongates and then tears larger eddies apart. This tearing apart of eddies is also the mechanism behind turbulence suppression via zonal flow structures [37] and magnetic shear [38]. While $E \times B$ shear does not seem to be the cause for ITBs at ASDEX Upgrade [21], they could still play a factor at bigger machines where larger values are reached.

Together with the $E \times B$ shear, the difference in magnetic helicity can additionally elongate the eddies. The magnetic shear

$$\hat{s} = \frac{r}{q}\frac{dq}{dr} \tag{2.31}$$

is usually positive as the toroidal current density decreases towards the edge. If the current has a well, for example, due to the bootstrap current, then the shear can also be negative. It has been found that negative magnetic shear suppresses even more effectively in the core and is known to create internal transport barriers [39, 40].

Impurities and fast ions

Finally, the main ions dilution effects by impurities or fast ions can be important. Fast ions are highly energetic particles being created either by a fusion reaction or by auxiliary heating. When impurities or fast ions are present, these will have different drift frequencies due to their mass and higher energy, respectively. The minority species will thus dilute the main ions in the plasma and couple differently (or not at all) to the ITG process detailed above [41].

Further effects of fast ions are more complicated, as they can drive subdominant modes such as Alfvén eigenmodes which can dampen energy from the dominant turbulent mechanism [42]. These interactions are still being actively researched [43].

MHD activity

Some MHD activity, such as tearing modes, have a negative effect on plasma confinement. On flux surfaces with a rational safety factor, a perturbation can self-amplify as the magnetic field closes on itself. In the core, if the safety factor is below one, a sawtooth instability [44] is triggered. It is a periodic process in which the plasma inside the region with $q \leq 1$ is reorganized and pushed outward. The fundamental sequence (depicted in figure 2.10) follows a fundamental pattern where the central temperature and density experience a gradual rise, succeeded by the precursor oscillation (not shown here), and ultimately culminating in an abrupt collapse known as a "crash." This entire sequence recurs periodically. In regions beyond the central area, an inverted sawtooth shape emerges, characterized by a gradual decline succeeded by a swift ascent as the hot and dense plasma is moved. While this can help avoid impurity accumulation, this is generally an unwanted process and can be prevented with careful current profile shaping.

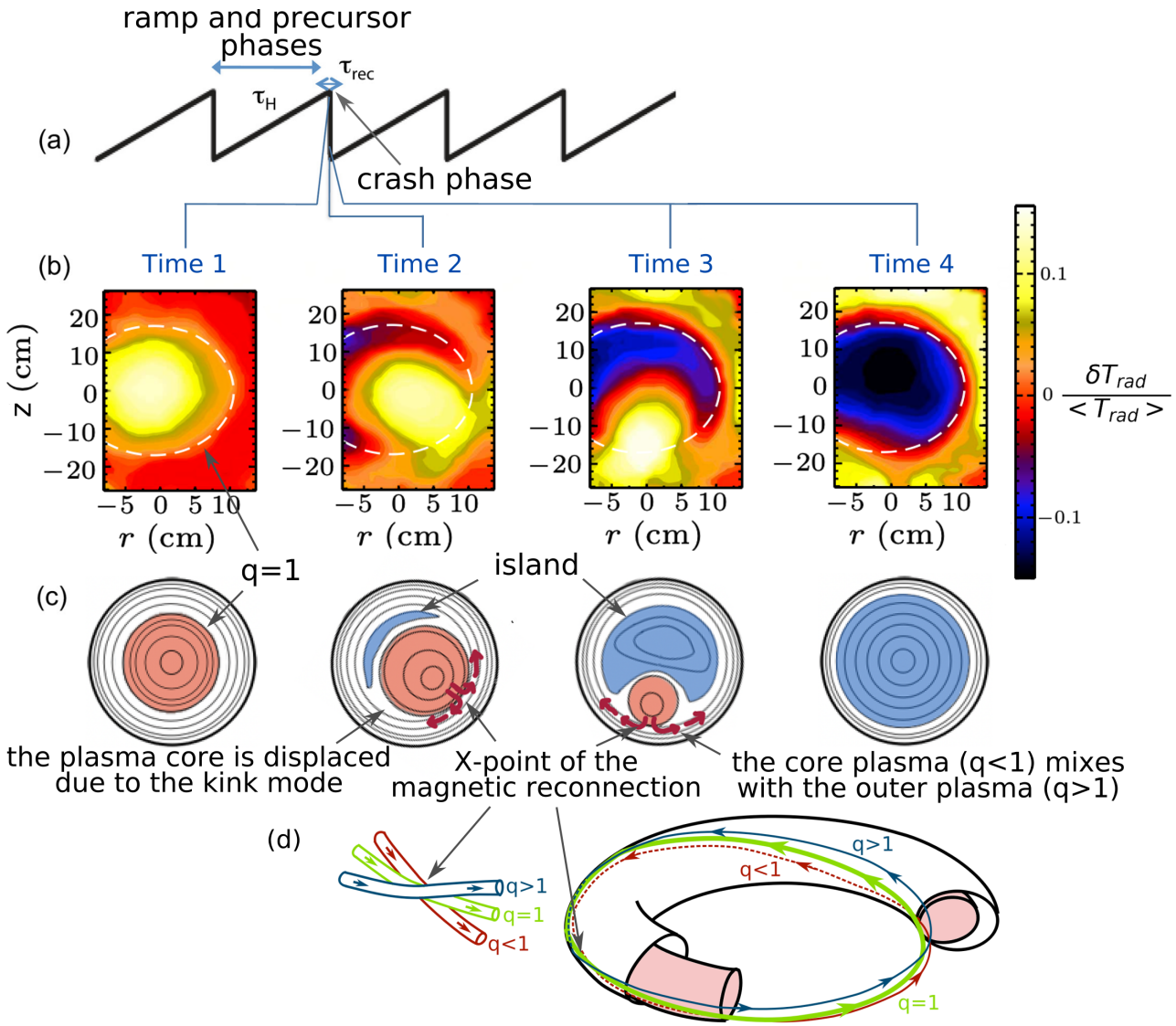

Figure 2.10.: An illustrative depiction of the fundamental 1D signal for electron cyclotron emission (ECE) is presented in a simplified manner in (a). Each cycle of this signal, known as a "sawtooth period," typically comprises two distinct phases: a gradual ramp and a preliminary phase lasting about 100 milliseconds, succeeded by an abrupt crash phase of approximately 100 microseconds. In (b), the 2D measurements of ECE during a single crash phase are displayed [45]. The parameter $\delta T_{rad}/\langle T_{rad}\rangle$ signifies the normalized fluctuation in electron radiation temperature. Additionally, the representation of magnetic flux surfaces and their reconnection is illustrated in (c), while the reconnection X-point is outlined in (d). The figure is taken from [46].

In the previous section, it was shown how temperature gradients can provide free energy to drive turbulence, the plasma current gradient can give rise to tearing modes. In these cases, the magnetic field lines reconfigure to a lower state where magnetic islands form. Often the island growth will be further driven by a gradient in the bootstrap current, which is why the

islands are often referred to as Neoclassical Tearing mode (NTM). Like the sawtooth instability tearing modes also lead to a decline of confinement. As figure 2.11 shows, the new magnetic configuration now has a radial component. As particles move almost instantaneously along the field lines, the kinetic profiles are flat in the region of the tearing mode.

A larger problem is the possibility of tearing modes to lead to disruptions. As the plasma rotates, the perturbed magnetic field induces *eddy currents* in the device's wall. The currents provide a torque, which slows the tearing mode and the plasma down. A mode is referred to as *locked* when it no longer rotates. A locked mode is often a direct precursor of a disruption. This violent process leads to loss of magnetic and kinetic energy, can damage parts of the vessel and must be avoided in future reactors[13].

To differentiate between different possible modes, one refers to the tearing mode as a m=#toroidalturns/n=#poloidalturns mode. Tearing modes can also be triggered by other MHD events such as ELMs and sawteeth. In figure 2.11, one can see a sketch of a 3/1 mode.

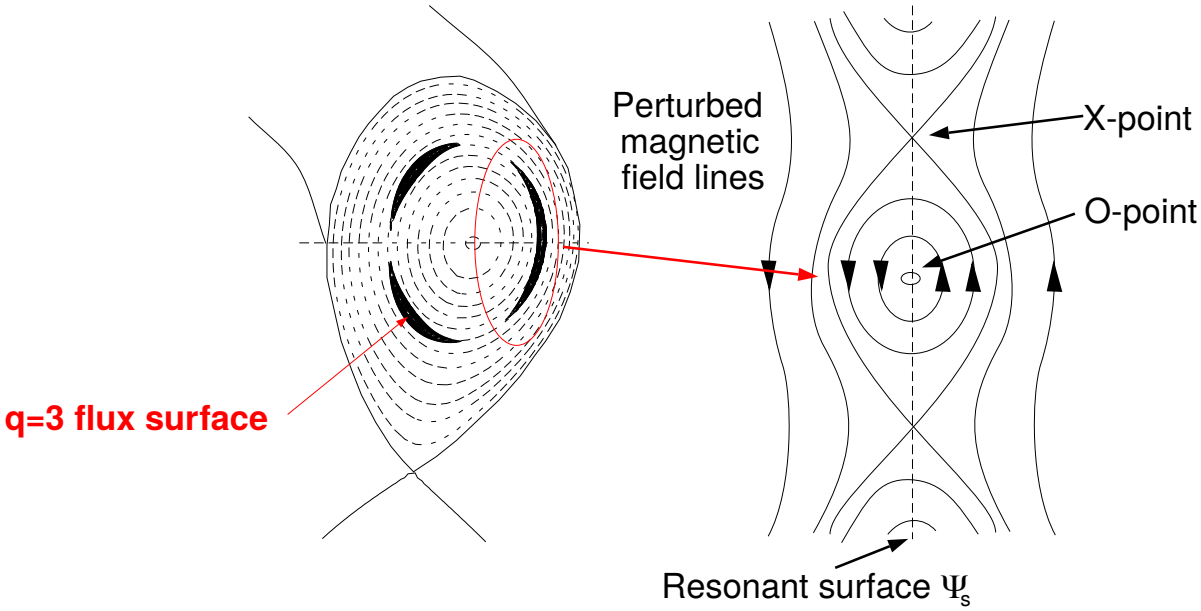

Figure 2.11.: Flux surfaces for a plasma with a 3/1 tearing mode. Gradients in the current density can give free energy to reorganize the magnetic field lines. Tearing modes lead to strong transport at their radius as particles can travel radially along the field lines. Image modified from [47].

2.4. Profile and transport modeling

As plasma turbulence theory becomes more advanced, more accurate replication of experimentally observed heat and particle flux levels is possible. As different factors like critical gradients, mode interaction, and electromagnetic effects are interconnected, computer simulations can be made almost arbitrarily expensive to run in the quest to predict these phenomena accurately. Depending on what needs to be learned from the simulations, a sensible model

must be chosen. In the next part, the various modeling codes used in this thesis are presented, along with a short explanation of the theories behind each code.

2.4.1. Profile predictions with ASTRA

The **A**utomated **S**ystem for **TR**ansport **A**nalysis (ASTRA) integrated modeling suite [19, 48] is the workhorse most used to model fusion plasmas at AUG. ASTRA was first developed in the 1980s in Moscow, with this thesis using the most recent ASTRA8 version. ASTRA plays a vital role in this thesis, as it simulates the profiles later used as a prior for IDA. ASTRA solves four 1-dimensional transport equations for n_e, T_e, T_i and the poloidal flux Ψ, derived in [49]:

$$S_e = \frac{1}{V'}\left(\frac{\partial}{\partial t} - \frac{B_0}{2B_0}\frac{\partial}{\partial \rho}\rho\right)\left(V' n_e\right) + \frac{1}{V'}\frac{\partial}{\partial \rho}\Gamma_e \tag{2.32a}$$

$$P_e = \frac{3}{2}\left(V'\right)^{-5/3}\left(\frac{\partial}{\partial t} - \frac{\dot{B}_0}{2B_0}\frac{\partial}{\partial \rho}\rho\right)\left[\left(V'\right)^{5/3} n_e T_e\right] + \frac{1}{V'}\frac{\partial}{\partial \rho}\left(q_e + \frac{5}{2}T_e\Gamma_e\right) \tag{2.32b}$$

$$P_i = \frac{3}{2}\left(V'\right)^{-5/3}\left(\frac{\partial}{\partial t} - \frac{\dot{B}_0}{2B_0}\frac{\partial}{\partial \rho}\rho\right)\left[\left(V'\right)^{5/3} n_i T_i\right] + \frac{1}{V'}\frac{\partial}{\partial \rho}\left(q_i + \frac{5}{2}T_i\Gamma_i\right) \tag{2.32c}$$

$$0 = \frac{J^2 R_0}{\mu_0 \rho}\frac{\partial}{\partial \rho}\left(\frac{G_2}{J}\frac{\partial \psi}{\partial \rho}\right) - \frac{V'}{2\pi\rho}\left(j_{BS} + j_{CD}\right) - \sigma_{\parallel}\left(\frac{\partial \psi}{\partial t} - \frac{\rho \dot{B}_0}{2B_0}\frac{\partial \psi}{\partial \rho}\right), \tag{2.32d}$$

with the volume derivative $V' = \frac{\partial V}{\partial \rho}$ and the assumption that the ion particle flux $\Gamma_i = \Gamma_e / Z_{eff}$. Γ_e will be referred to as Γ for the rest of the thesis.

ASTRA combines multiple subroutines to predict density and temperature profiles (predictive mode) or provide the conductivities needed to keep the profiles constant (interpretative mode). Provided with some initial profiles and the last-closed-flux surface, ASTRA will calculate a 2D equilibrium with the SPIDER code [50, 48]. As the predicted profiles are 1D, ASTRA is referred to as 1.5D. The plasma current, q-profile and magnetic field are prescribed and are not allowed to deviate from the experiment so that the SPIDER equilibrium is as close to the one used in IDA as possible. For ASTRA8, the SPIDER equilibrium has been found to match the initial one well. Other inputs such as experimental profiles, Z_{eff} and heating information, including type of source, time of operation as well as power and angles, are given using TRVIEW [51].

ASTRA gives the user a wide array of subroutines and applications, so the presented predictive model, which is coupled with the quasi-linear turbulence code TGLF, shall be referred to as ASTRA-TGLF. ASTRA-TGLF will simulate the kinetic profiles using the ASTRA transport matrix, shown in equation 2.33, with the diagonal terms (χ_e, χ_i and D_n) representing the electron and ion heat as well as the particle diffusivities and C_n which is the particle pinch term. The matrix terms are determined by the neoclassical model NCLASS [52] and TGLF [29] for the turbulent transport contribution. NCLASS can usually be ignored for the electrons but is important for the ion transport close to the edge. It would also be capable of providing the bootstrap current if the current is evolved in the future. The other terms of the transport

matrix, for example, the dependence of the particle transport on the ion temperature gradient χ_n^i, are automatically included in the diagonal terms by TGLF and are thus set to 0.

$$\begin{pmatrix} \frac{\Gamma_e}{n_e} \\ \frac{q_e}{n_e T_e} \\ \frac{q_i}{n_i T_i} \\ V' G_1 \frac{\mu_0 j_{BS}}{B_p} \end{pmatrix} = -V' G_1 \begin{pmatrix} D_n & \chi_n^e & \chi_n^i & C_n \\ D_e & \chi_e & \chi_e^i & C_e \\ D_i & \chi_i^e & \chi_i & C_i \\ D_E & \chi_E^e & \chi_E^i & 0 \end{pmatrix} \cdot \begin{pmatrix} \frac{1}{n_e}\frac{\partial n_e}{\partial \rho} \\ \frac{1}{T_e}\frac{\partial T_e}{\partial \rho} \\ \frac{1}{T_i}\frac{\partial T_i}{\partial \rho} \\ \frac{E_\parallel}{B_p} \end{pmatrix} \tag{2.33}$$

The profile is given for 91 points radially with a timestep of 25ms, with all subroutines being recalculated every step. The simulation is usually run for around 80 time steps, at which point the predicted profiles have converged to stable values. TGLF is a local model and mostly tuned to core plasma parameters. As strong profile variations at the edge require a radially global treatment, TGLF often fails close to the separatrix. The use of a boundary condition beyond which point the predicted profiles are kept equal to the input was chosen. This boundary condition could be removed when approaches as in [53, 54] are further validated. Keeping the boundary at $\rho_{tor} \leq 0.9$ for now also means one does not need a sophisticated neutrals model as most neutrals stemming from the scrape-of-layer would be ionized before they reach the boundary condition [55] and computational time is saved as the turbulence code needs to be run for less radial points. ASTRA also does not have a fully consistent MHD model to simulate sawteeth [22] instabilities. As TGLF struggles in the vicinity of the magnetic axis $\rho_{tor} < 0.2$, the model relies on additional diffusion terms where the safety factor q < 1 and $\rho_{tor} \leq 0.2$ to not have too high temperatures and densities in the core and sawtooth region.

If a fully integrated approach to combine the different integrated data frameworks, introduced in section 3.3.7, is attempted, the plasma current could be left to evolve. Recently, much progress has been made in predicting current profiles at ASDEX Upgrade [56] and this work could be implemented in the current model. Using a simple sawtooth model, based on [57], which periodically flattens the profile, was tested in this thesis. The sawtooth model did improve the overall match of T_e, but was abandoned due to unpredictable behavior if the q=1 surface was far from the center. Other models, such as IMEP [54], did have more success with the sawtooth model, making it a potential area to revisit in the future.

The heat sources of equation 2.32 are given by:

$$\begin{aligned} P_e =& P_{ECRH} + P_{e,NBI} + P_{Ohm} - P_{RAD} - P_{e,i} \\ P_i =& P_{e,i} + P_{i,NBI} \end{aligned} \tag{2.34}$$

where P_{ECRH} is the ECRH heating, P_{NBI} the neutral beam heating, P_{Ohm} ohmic heating, P_{RAD} the power lost to radiation and the equipartition term $P_{e,i}$ which is the power transferred to ions by collisions at the radius ρ.

The ohmic heating and electron-ion energy transfer are calculated inside of ASTRA. The Ohmic heating depends on the resistivity, which varies radially due to the temperature profile. It is proportional to I_p^2, but as the resistivity drops with $T^{-3/2}$ it is usually only relevant for L-mode discharges. The same is true for the electron-ion heat transfer as the characteristic

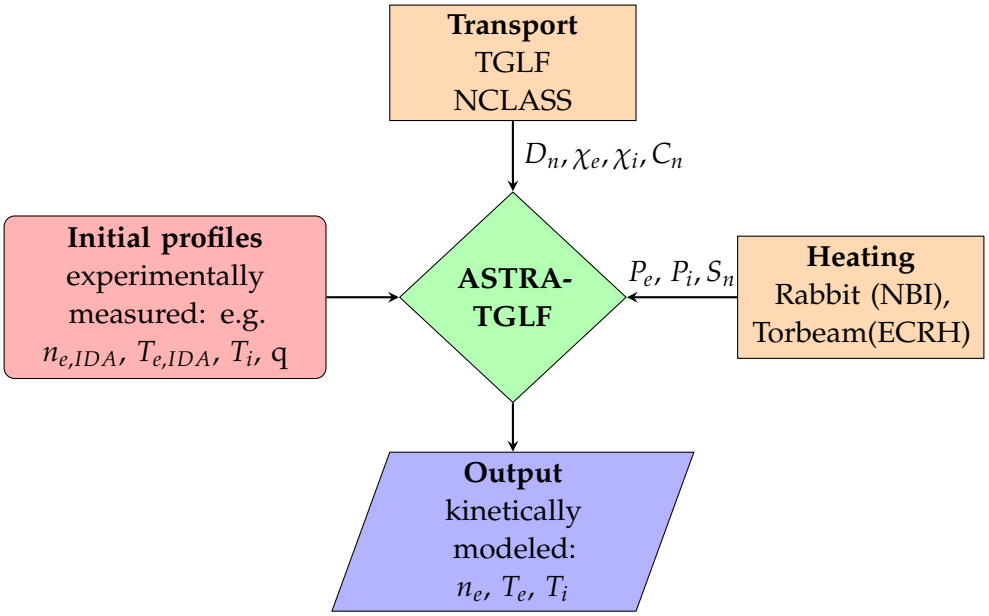

Figure 2.12.: Simple workflow of the ASTRA-TGLF workflow. The T_i profile is not employed to calculate the kinetic modeling priors probability but is used to validate the simulation results.

collision time τ_{ie}, meaning the time for an initial momentum to be canceled, has the same temperature dependency [11]

$$\tau_{ei}[s] = 2.9 \cdot 10^{10} \frac{(T[eV])^{3/2}}{n[m^{-3}]}. \tag{2.35}$$

The exchanged power has the most noticeable effect if there is a large $\frac{T_e}{T_i}$ fraction and/or no auxiliary ion heating is present, with

$$P_{ei} = \frac{3 m_e n_e}{m_i \tau_{ie}} (T_e - T_i) \tag{2.36}$$

The auxiliary power source terms and current drive is calculated by RABBIT [58] for NBI and TORBEAM [59] for ECRH. Both codes are given the total power and angle input of the used heating system from experimental values. RABBIT then calculates the NBI fast-ion distribution given the kinetic equation and uses a collisional model that considers the excitation and ionization of ions and impurities, while TORBEAM employs an electron-cyclotron beam tracing approach using a set of ordinary differential equations. RABBIT is also capable of calculating the fusion energy from plasma-beam interactions, which are usually negligible for the D-D reactions but do play a significant role when simulating JET D-T scenarios.

The particle source comprises the subroutine NEUT, which simulates neutrals coming from the scrape-off layer and RABBIT, which calculates the particles coming from the NBI. NEUT usually does not play a large role as the boundary condition is far enough inside the plasma that neutral particles will have ionized.

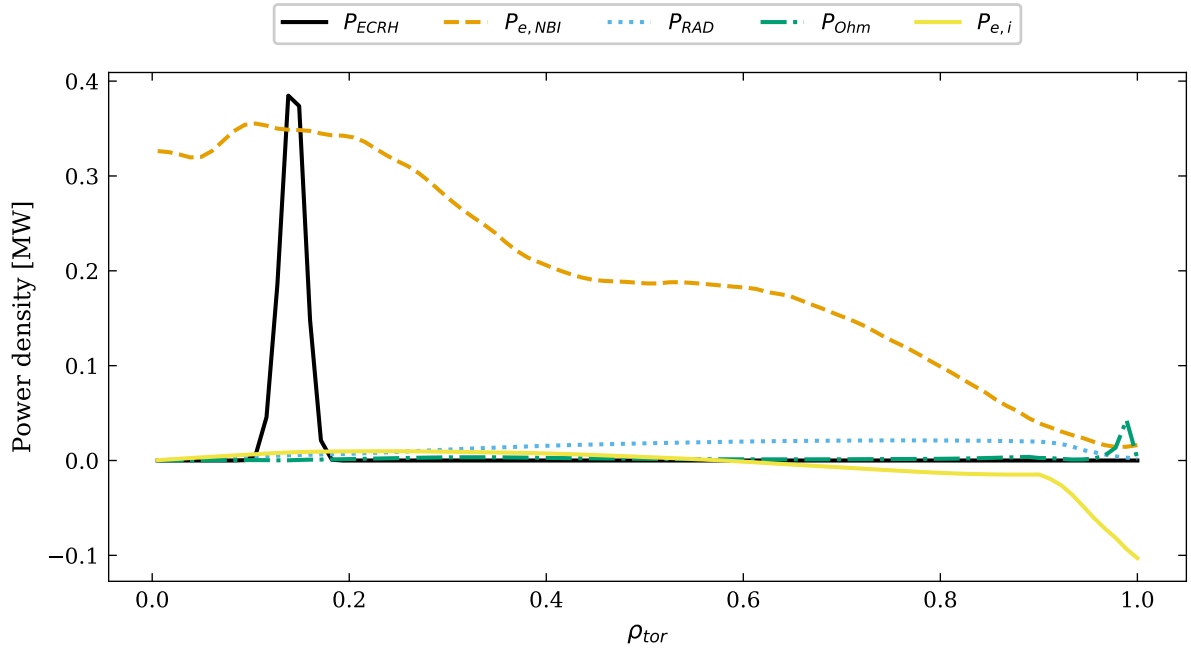

Figure 2.13.: Heating mix for discharge #33616 for electrons. ECRH heating is very localized and only heats the electrons. The NBI has a spread curve as the neutral particles ionize, traveling through the plasma. Radiation, ohmic heating and collisions are almost negligible compared to the auxiliary heating sources.

For the thesis, ASTRA-TGLF had a main impurity of Carbon, whose concentration is based on Z_{eff}:

$$n_{Carbon} = \frac{(Z_{eff} - Z_{main}) \cdot n_e}{(Z_{Carbon} - Z_{main}) \cdot Z_{Carbon}}, \tag{2.37}$$

with $Z_{main} = 1$ being the deuterium charge. Carbon dilutes the plasma slightly less than Boron, which is assumed to be the main impurity in actual experiments. The smaller dilution is expected to be closer to an actual plasma with high-Z impurities. Still, Carbon and Boron are similar enough as to not negatively impact the turbulence simulations. Adding impurities to ASTRA-TGLF has stabilizing effect on the turbulence as fewer main ions are driving the ITG turbulence [41]. Additionally, the tungsten concentration, measured by [60], was added as an important source of radiation. Especially in L-mode the radiated power represents a crucial parameter in matching the experimental T_e profile, with the radiated power often being too small. In these cases, the tungsten concentration was varied until the radiation matched the value given by bolometry diagnostics.

In figure 2.14, one can see a predictive simulation of an L-mode discharge #36190, with the boundary condition at $\rho_{tor} = 0.9$.

While the ASTRA-TGLF model is constantly being improved, some key limitations remain. Across multiple experiments, fast ions coming from ICRH or NBI heating have been found to

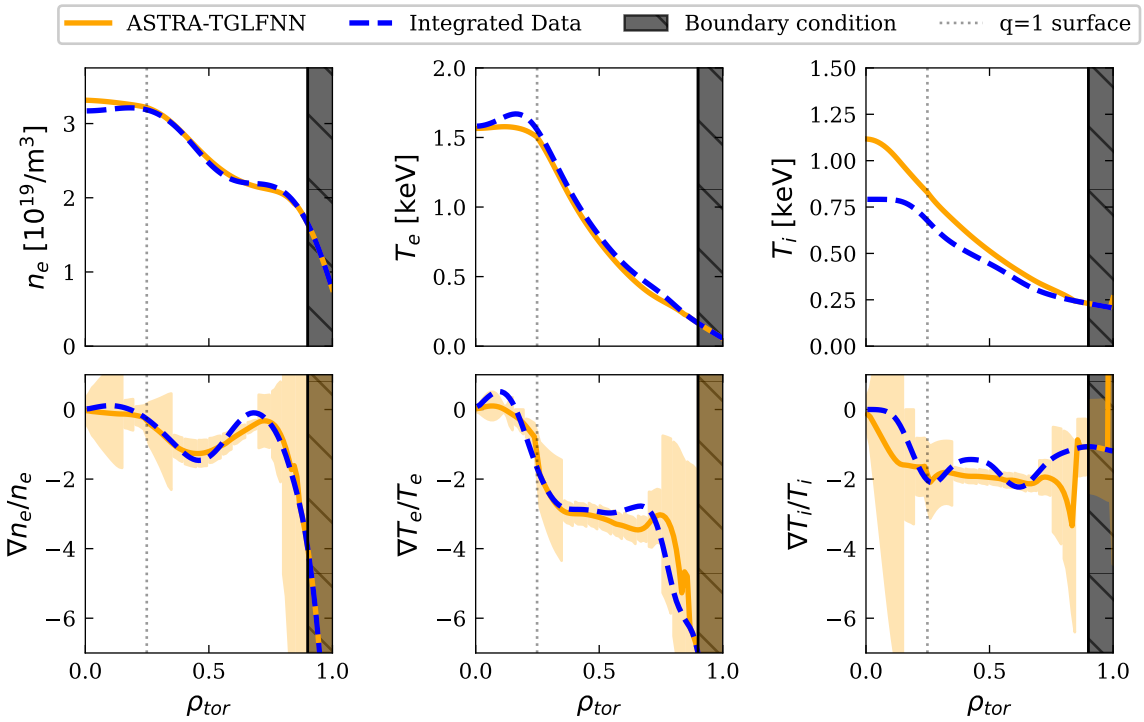

Figure 2.14.: Example of an L-mode discharge #36190 simulated with ASTRA-TGLF. At the boundary condition, the simulation is kept constant with the experimental values. Inside the q=1 surface, sawteeth are simulated by additional diffusive coefficients. In the second row, one can see the log gradients with their uncertainties described in subsection 4.1.

limit turbulent transport further than would have been expected from the ion dilution [61]. In general, ASTRA has a hard time simulating internal transport barriers, which are present in advanced scenario discharges [62, 63]. This is partly because ITBs are not yet as well understood as the barrier leading to H-mode which has been modeled in the IMEP framework using MHD codes [54].

ASTRA can also not simulate tearing modes, explained in more detail in section 5.4.2 or disruptions. Disruptions are a sudden drop in thermal energy (thermal quench) followed immediately by a drop in plasma current (current quench), leading to a loss of the discharge [13]. Disruptions can have multiple causes and are difficult to predict [64].

2.4.2. Gyrokinetic simulations of plasma turbulence with GENE

GENE (Gyrokinetic Electromagnetic Numerical Experiment) [22] is one of the most complete plasma turbulence codes available and has been used to simulate many different tokamaks such as JET [65], DIII-D [66] and ASDEX Upgrade [67].

Taking the kinetic equation and assuming that due to the plasma's temperature, the collision

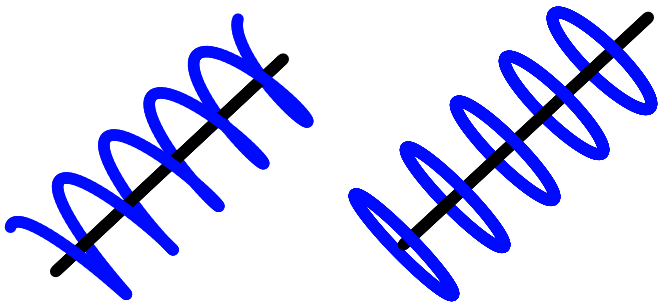

Figure 2.15.: By assuming that the timescales of turbulent transport are slower than the gyrofrequency, GENE averages out the gyromotion and considers charged Larmor radius-sized rings along the flux tubes. This Gyrokinetic approach simplifies the Vlasov equation to a 5-dimensional problem. Image taken from [68].

term is zero, one receives the 6-dimensional Vlasov equation:

$$\frac{\partial}{\partial t} f(r,v) + v \cdot \nabla f(r,v) + q/m(E + v \times B) \cdot \nabla_v f(r,v) = 0 \tag{2.38}$$

with the distribution function f and ∇_v the derivative in velocity space. By making the assumption that turbulence dynamics occur on a longer timescale than the gyrofrequency, one can remove one velocity dimension by approximating the gyrating motion as a charged ring moving along the field lines. This approximation is called the gyrokinetic approach and is the basis of the GENE simulations.

GENE assumes that the distribution function f can be divided into a fluctuating part δf and a part that is a constant background. GENE is also built on the "gyrokinetic orderings" from [69]:

- Relative fluctuation levels are small e.g. $\delta T_e / T_e << 1$
- The fluctuations are anisotropic, with the wavelengths perpendicular to the magnetic field being a lot smaller than those parallel to it, as seen in figure 2.5.
- Relevant turbulence frequencies are well separated from the gyrofrequency

With these assumptions, GENE is capable of solving the δf gyro-kinetic equations in both a linear and non-linear way, as well as taking electromagnetic effects (self-consistently calculating parallel and perpendicular fluctuations in the magnetic field stemming from the turbulent plasma) into account. The linear solution calculates the most unstable modes along with providing info on their growth rates and characteristic size. At the same time, the non-linear simulations are needed to understand the interaction of different unstable modes and larger-scale structures such as zonal flows and to calculate heat fluxes.

GENE can couple to multiple equilibrium codes, making various geometries possible. While global simulations are possible, this thesis shall mostly discuss the results of local GENE simulations in which fluxtube simulation domains at specific radii were examined. Fluxtube simulations assume radially constant temperature and density profiles and gradients.

This is a good approximation in the core, if the experimental profiles do not change strongly in the simulated box size. Global simulations aim to capture the behavior of the entire plasma or at least a substantial portion of it within a fusion device. Instead of focusing on a single localized region like fluxtube simulations, global simulations consider the interactions and effects propagating across the volume. These simulations consider the coupling between different plasma regions, capturing phenomena that may not be present in isolated fluxtubes. Global simulations provide a more comprehensive understanding of plasma behavior and can reveal global instabilities, transport processes, and confinement properties. However, fluxtube simulations are considerably cheaper computationally.

GENE can consider any number of impurity species, trapped and passing, into account but this will make the simulations even more expensive, with run times of several months in some cases.
GENE is currently being developed for application at and beyond the separatrix [70] and for stellarator geometries [71].

2.4.3. Gyrofluid simulations with TGLF

While gyrokinetic simulations are state-of-the-art, they require too much computing time to be used frequently for predicting kinetic profiles. By making several simplifications, the quasi-linear turbulence code TGLF (Trapped Gryo Landau Fluid) is capable of providing turbulent fluxes in a matter of seconds. For one, TGLF assumes that the plasma can be described with attributes such as density and temperature. These quantities are calculated in the gyrofluid approach by solving the moments of the distribution function using the linearized gyrokinetic equation. In references [72] the electrostatic TGLF equations are derived. TGLF can also be run with electromagnetic effects, for which the equations can be found in [73, 74, 75].

The electromagnetic linearized gyrokinetic equation is

$$\left(\frac{\partial}{\partial t} + v_\parallel \nabla_\parallel + i\omega_{dv}\right) \tilde{g} = \left(-v_\parallel \nabla_\parallel - i\omega_{dv} + i\omega_*^T\right) f_0 J_0 \frac{e}{T}[\widetilde{\phi} - \frac{v_\parallel}{c}\widetilde{A_\parallel}], \tag{2.39}$$

with f_0 being the equilibrium's distribution function, J_0 being a Bessel function estimating finite Larmor radius effects, ω_{dv} perpendicular curvature drifts and ω_*^T including driving pressure gradients. $\widetilde{A}$ is the perturbed vector potential. $\tilde{g}$ is the non-adiabtic part of the perturbed distribution function $\tilde{f}$ [74].

The moments are calculated by integrating over the distribution function multiplied by v^n for the n-th moment. The integrals can be used to calculate the physical properties of the plasma. Simple moments are

$$
\begin{aligned}
n &= \int f(\vec{v}) d^3v \\
\vec{u} &= 1/n \int \vec{v} f(\vec{v}) d^3v \\
T &= \frac{m}{3nk} \int \vec{w}^2 f(\vec{v}) d^3v \\
\vec{p} &= \frac{m}{3nk} \int \vec{w} \otimes \vec{w} f(\vec{v}) d^3v \\
\vec{Q} &= \frac{m}{2} \int \vec{w}^3 f(\vec{v}) d^3v,
\end{aligned}
$$

with $\vec{u}$ being the velocity of the mass center, $\vec{w} = \vec{v} - \vec{u}$ the thermal velocity and $\otimes$ the tensor product.

TGLF calculates 12 moments for passing (for the entire velocity space and for the trapped region only the moments are: density n, parallel velocity $v_{\parallel}$, parallel pressure $p_{\parallel}$, total pressure p, parallel energy flux $Q_{\parallel}$ and total energy flux Q) and 3 moments for trapped particles (density n_t, parallel pressure $p_{t,\parallel}$ and total pressure p_t) for each species (derived in detail in [72] and summarized in [29]). The electromagnetic moments can be found in [76]. The passing particles are attained by subtracting the six moments of the trapped region from the total velocity space. As the name suggests, the kinetic effect of Landau damping is included in the model by fitting the moment's closure coefficients to reproduce the linear kinetic response.

It further assumes a linear response function, also called quasi-linear weight, is valid. The linear response presumes that the phases between the fields and velocity moments of distribution functions, responsible for non-linear transport fluxes, closely resemble the linear phases of the most unstable eigenmode for each poloidal wavenumber. This approximation appears correct primarily in tokamak core plasmas with validation coming from fluctuation phase measurements [77] and non-linear gyrokinetic turbulence simulations [78]. Solving for the most important eigenmodes, the linear solver finds eigenvalues expressed as the oscillation frequency and growth rate $\omega(k_y) + i\gamma(k_y)$, with k_y being the binormal wavenumber.

In order for the linearly calculated modes to not grow infinitely and to give actual transport values, saturation rules are used [20]. The final quasi-linear flux, derived in [79, 80], is given as

$$
\begin{aligned}
Q_\alpha &= \text{Dimension Factor} \cdot \sum_{k_y} \text{Linear Response } \cdot \text{Saturated Potential} \\
\text{Dimension Factor} &= \frac{3}{2 n_e T_e} \\
\text{Linear Response } &= \frac{Re\langle i k_y \tilde{\Phi} * \tilde{p_\alpha} \rangle}{\langle \tilde{\Phi}^* \tilde{\Phi} \rangle} \\
\text{Saturated Potential Intensity} &= \bar{\Phi}^2.
\end{aligned}
$$

The saturation rule SAT-2, will be discussed in the next subsection.

Like the local GENE simulations, TGLF calculates the transport for a single radial position, with the advantage that a single simulation lasting on the order of a second makes it possible to simulate several radii simultaneously. TGLF can successfully model turbulence types such as ITG, TEM, ETG, and kinetic ballooning modes (KBM) [24] in the core and is able to model finite β electromagnetic stabilization effects [81]. However, it is often not able to capture the physics when turbulence is suppressed, such as in cases of fast ions and close to the pedestal in H-mode discharges.

This thesis employed mostly standard settings for TGLF in ASTRA. TGLF is calculated on 16 different cores simultaneously, which usually amounts to 5 TGLF calculations per core per step. The Kygrid model=4, which calculates "additional low-ky modes preferred for SAT2" [82] and a maximum number of Hermite basis functions of 6. This makes TGLF SAT-2 run slower than SAT-1, which only requires 4 basis functions.

TGLF Saturation rule 2

The saturation rules are created by comparing the model to high-fidelity codes such as CGRYO [83]. In this thesis, the SAT-2 saturation rule [84] is used, which matches CGYRO up to about 16% in the energy fluxes and 33% for the density flux for the fitting database. This is a big improvement of the SAT-1 model (Q_i 53%, Q_e 57% *and* Γ 75%. As the particle flux is smaller than the heat fluxes in the database, this relative error for the density is better than it might look at first glance.

Like SAT-1, SAT-2 takes the mixing of different modes at different length scales into account and should thus capture the non-linearly observed Dimits-shift. It also takes into account the ratio of poloidal and radial wavelengths, which is shortened for small k_y resulting in "streamers" [85]. SAT-2, compared to SAT-1, is updated with varying eigenmode magnitude with the poloidal angle θ. This was found necessary due to differences between the high-fidelity codes CGYRO and its predecessor GYRO [84].

TGLF uses the gyroBohm normalizations also used in CGYRO simulations: The deuteron sound speed $c_s = \sqrt{T_e/m_D}$, gyroradius $\rho_s = c_s/\omega_s$, gyrofrequency $\omega_s = \frac{eB_{unit}}{m_D c}$ with c being the speed of light and $B_{unit} = \frac{q}{r}\frac{d\Psi}{dr}$. The energy fluxes are also normalized to gyroBohm units $n_e T_e c_s (\rho_s/a)^2$.

Like the SAT-1 model, TGLF SAT-2 assumes that the $E \times B$ flow shear stemming from zonal flows has the strongest saturation effect on the linear growth rate. The zonal flow mixing rate can be assumed to be of the same size as the linear growth rate γ_{k_y} at all k_y[85]. The $k_y = 0$ poloidal zonal flow thus dampens the most unstable modes, which are assumed to have a finite poloidal k_y and a radial $k_x = 0$. The Root Mean Square (RMS) zonal flow velocity for TGLF is then given by

$$V_{ZF} = max\{\gamma_{k_y}/k_y\}, \tag{2.40}$$

with γ_{k_y} being the linear growth rate for the most unstable mode for every k_y. V_{ZF} is found to match the zonal flow velocity calculated by the non-linear saturated spectrum by CGYRO

well (see figure 3 in [84]). The growth rate and wavenumber, for which equation 2.40 is given, will be referred to as $\gamma_{\max}$ and k_{ymax}.

In SAT-2 the growth rate $\gamma_{k_y}^{\text{SAT-2}}$, radial wavenumber $k_x^{\text{SAT-2}}$ and shape function G_θ are all piecewise linear in k_y. The radial wavenumber is given by

$$\begin{aligned} k_x^{\text{SAT-2}} =& \frac{B_{\text{unit}}}{B_{\text{norm}}} k_{\text{ycut}} \,/|\nabla r|_0 && \text{for } k_y < k_{\text{ycut}} && (2.41)\\ =& \frac{B_{\text{unit}}}{B_{\text{norm}}} \left(k_{\text{ycut}} \,/|\nabla r|_0 + b_1 \left(k_y - k_{\text{ycut}}\right) G_q(0)\right) && \text{for } k_y \geqslant k_{\text{ycut}} && (2.42) \end{aligned}$$

where $k_{\text{ycut}} = b_0 k_{ymax}$.

The modeled mixing rate $\gamma_{k_y}^{SAT-2}$, which is estimated to be equal to the linear growth rate, has been simplified in comparison to TGLF SAT-1 and is now just multiplied by the fitting parameter b_2.

$$\begin{aligned} \gamma_{k_y}^{\text{SAT-2}} &= b_2 \gamma_{k_y} && \text{for } k_y < k_{y\max} && (2.43)\\ &= b_2 \gamma_{\max} && \text{for } k_y \geqslant k_{y\max}, && (2.44) \end{aligned}$$

However, when taking electron scale effects into account, it was found necessary to extend the model. For example, a too-small electron-scale electron energy flux was found when decreasing the ion temperature gradient. This lowers the zonal flow velocity and thus the mixing rate. When $\gamma_{k_y}^{\text{SAT}-2}$ reaches values below the growth rate at electron scales, the electron energy rises. To achieve a better fit with CGYRO for $k_y \geqslant k_{y\max}$

$$\gamma_{k_y}^{\text{SAT}-2} = b_2 \left(\gamma_{\max} + \max\left[\gamma_{k_y} - \alpha_{\text{ZF}} k_y V_{\text{ZF}}, 0.0\right]\right), \tag{2.45}$$

with α_{ZF} being fit to 1.05.

The saturated electric potential amplitude has a peak $\Phi(0)_{0,k_y}$ at $k_x = 0, \theta = 0$ and is given by

$$\Phi(\theta)_{k_x,k_y} = G(\theta) \frac{\Phi(0)_{0,k_y}}{\left(1 + \left(k_x / k_x^{\text{RMS}}\right)^2\right)} \tag{2.46}$$

with the modeled intensity

$$I_{k_y}^{\text{SAT-2}} = \Phi(\theta)_{k_x,k_y} = \left\langle G^2(\theta) \right\rangle_\theta \left(\frac{\gamma_{k_y}^{\text{SAT-2}}}{k_x^{\text{SAT-2}}\, k_y}\right)^2 \tag{2.47}$$

for which the $\theta = 0$ is at the outer midplane.

$G(\theta)$ is responsible for the poloidal angle dependence of the model.

$$\begin{aligned} G^2(\theta) =& d_1 G_1(\theta) && \text{for } k_y < k_{y\text{cut}}\\ =& \left(d_1 G_1(\theta) k_{\text{ycut}} + b_3 d_2 G_2(\theta) \left(k_y - k_{y\text{cut}}\right)\right) / k_y && \text{for } k_y \geqslant k_{y\text{cut}} \end{aligned} \tag{2.48}$$

G_1 and G_2 are geometric functions dependent on the magnetic field and d_1 and d_2 coefficients. TGLF SAT-2's parameter (b_0, b_1, b_2, b_3) were then fitted to match the results of 64 CGYRO simulations, which varied different input parameters such as the safety factor, elongation and logarithmic gradients in 13 parameter scans.

Apart from the saturation rule, the TGLF linear eigenmode solver was further improved for cases with large density gradients by implementing a new collision model for electrons. While the solver is slower than in the TGLF SAT-1 model, it is still 18000 times fast than running CGYRO linearly.

Previous validation efforts of TGLF

In order to use ASTRA-TGLF as a prior for the IDA framework, the potential weaknesses of the TGLF model need to be known. This section gives an incomplete overview of earlier TGLF studies.

TGLF has been used at multiple tokamaks to simulate discharges with the many different heating schemes, magnetic fields and shaping. This section is a small overview of published work with TGLF SAT-1, TGLF SAT-1geo (a predecessor of SAT-2) and SAT-2.

Ref. [86] compared TGLF with both saturation rules to gyrokinetic simulations at JET-ILW and found slightly lower ion and electron stiffness. This discrepancy is particularly evident when using the SAT-2 saturation rule, which necessitates higher R/L_{T_i} values to match Q_i. Furthermore, the electron stiffness in the lower Q_e region is underestimated, particularly when employing SAT-2. Conversely, when incorporating a realistic mixture of light impurities, the TGLF SAT-1geo simulations closely approximate experimental observations for both Q_e and Q_i.

Ref. [87] has validated high-fidelity gyrokinetic simulations against experiments with deuterium and hydrogen isotopes at ASDEX Upgrade as well as simulated the plasma with TGLF SAT-2 using VITALS [88]. To extract $\delta T_e/T_e$ levels and the cross-phase angle between the density and temperature fluctuations α_{nT}, new synthetic diagnostics were introduced, employing a Gaussian function to represent the diagnostic antenna pattern in wavenumber space. TGLF SAT-2 successfully captured the higher deuterium temperature fluctuations compared to hydrogen and higher ion and electron heat flux. The simulations consistently showed a negative cross-phase angle between density and temperature, with the magnitudes roughly matching experimental observations. However, TGLF SAT-2 failed to replicate that the hydrogen had the larger cross-phase angle, which displayed almost constant α_{nT} values with varying isotope mass. Despite careful iterations of profile gradients, $v_{E\times B}$ shearing rates, and Z_{eff} within the VITALS framework, the ion heat flux was significantly overestimated, particularly in hydrogen by a factor of up to $7 \cdot Q_i$.

Ref. [89] examined the dependence of turbulent transport on the magnetic field at the ASDEX Upgrade tokamak with ASTRA-TGLF SAT-2. Based on gyroBohm scaling, one would assume a strong effect for the confinement, however, the scaling law IPB98 [8] predicts a very weak dependency. ASTRA-TGLF reproduces the experimental data and further predicts

confinement in line with the scaling laws for hypothetical devices.

Ref. [90] simulated ASDEX Upgrade and JET-ILW plasmas with varying T_e/T_i from 1.1 to 5.7 to prepare for the future ITER experiment with SAT-1geo. The simulated temperature profiles closely match experimental data, allowing for simulations closer to the last closed flux surface. TGLF accurately predicts central electron temperatures with a relative deviation of only (-10 ± 6)% under ITER-like conditions. However, TGLF tends to slightly underestimate T_e and T_i at high T_e/T_i and overestimates them at low T_e/T_i. TGLF also performs well in predicting the edge ion heat flux $Q_{i,edge}$, which might even make it suitable for examining H-mode accessibility at ITER. Notably, in the conditions of dominant auxiliary electron heating explored in this study, TGLF's predictions of heat and particle transport exhibit good agreement with experimental results and theoretical expectations, suggesting its reliability for simulating hydrogen plasmas in PFPO-1, despite being calibrated solely on deuterium plasmas.

Ref. [91, 92] studied cold pulses at Alcator C-mod, DIII-D and ASDEX Upgrade with TGLF SAT-1 supporting the effectiveness of local quasi-linear transport models explaining the physics of the at first sight surprising temperature rise in the core. However, this rise is only possible in discharges with large electron heating and thus large T_e/T_i.

Ref. [93] examined a high-performance JET-ILW hybrid deuterium discharge with GENE and compared to TGLF SAT-1geo. The comparison between TGLF and GENE, considering both the electromagnetic (EM) and electrostatic (ES) cases, reveals remarkably good agreement in terms of growth rates and frequencies. When comparing only the EM case, TGLF demonstrates better agreement with GENE on flux levels than QuaLiKiz to GENE, as TGLF can model linear EM stabilization. Nonetheless, TGLF lacks non-linear EM stabilization physics, leading to an incomplete representation of the strong EM stabilization at the inner radius. Additionally, TGLF exhibits a too-small anti-gyroBohm (anti-gB) effect at both radii when tritium is used instead of deuterium.

Ref. [94] shows results DIII-D ITER baseline simulations comparing NBI+ECRH and ECRH heating only with TGLF coupled with TGYRO [95] which functions similarly to the ASTRA-TGLF transport model. When incorporated into TGYRO simulations, the TGLF transport model accurately captures the observed changes in plasma profiles and confinement. This capability is attributed to its ability to account for transport processes occurring across multiple spatial scales and channels. Moreover, TGLF predicts that electron fluctuations will generate an inward particle pinch, leading to a steeper density gradient, which aligns with experimental observations. Importantly, this inward pinch is expected to intensify as collisionality decreases when moving from ITER Baseline Scenarios to the actual ITER tokamak.

Ref. [63] (using SAT-1) and [62] (using SAT-0) both examined advanced scenarios at ASDEX Upgrade. Ref. [62] saw a high influence of $E \times B$-shear in TGLF simulations that GENE did not reproduce. Ref. [63] concluded that SAT-1 lacked physical accuracy when fast ion effects were relevant and at high-β. $\beta = \frac{\langle p \rangle}{B^2/2\mu_0}$ is the ratio of magnetic and thermal pressure and shows how efficient the confinement is.

Ref. [96] validated the stiffness of SAT-0 on DIII-D H- and L-mode discharges. Simulations

were done at different NBI heating levels and different torque with errors of less than 15%. It was found that TGLF performed best at low-torque and even sometimes outperformed non-linear GYRO predictions on which TGLF SAT-0 is based on.

Finally, Ref. [54, 97] have used ASTRA-TGLF coupled with an MHD solver at the edge to simulate ASDEX Upgrade, Alcator C-mod and JET-ILW discharges without experimental profiles. The simulations consistently perform better than the ITER scaling laws and will be looked at in more detail in subsection 6.2.

The passage discusses applying and evaluating the TGLF model in kinetic simulations. TGLF's usage across different tokamaks and scenarios, including comparisons with gyrokinetic simulations, is covered. Notably, TGLF's predictions exhibited good agreement with GENE regarding growth rates and frequencies. It effectively explained temperature rises during cold pulses driven by large electron heating and T_e/T_i ratios. TGLF correctly predicts the flux dependence on the magnetic field, while it struggles with the ion mass. Recently, a new saturation rule TGLF SAT-3 has been published, which aims to capture the mass effect more correctly [98]. This new saturation rule is not yet included in ASTRA and has not yet been extensively validated otherwise, which is the reason this thesis continued using TGLF SAT-2.

Having introduced the different models and sources of transport in Chapter 3, the ASDEX Upgrade tokamak against which the models are validated is presented. The chapter further introduces the different auxiliary heating systems that act as sources in the ASTRA transport equations 2.32. Finally, the Integrated Data Analysis framework and the diagnostic it utilizes are illustrated.

3. Heating and Diagnostics at ASDEX Upgrade

The ASDEX Upgrade (AUG) tokamak is situated in Garching, Germany. It is the successor of the ASDEX tokamak, where the H-mode confinement regime was discovered [18]. It is classified as a medium-sized tokamak (MST) with a major radius of R_0=1.65m and a minor radius of r=0.6m. This thesis uses AUG discharges of around 8s at a toroidal magnetic field of 2.6T. It is difficult to run the tokamak for longer than ten seconds as the toroidal field coils are not superconducting and thus heat up over time. Discharges can be run with hydrogen, deuterium and helium-3 as the main ion source. Through the use of poloidal shaping coils, configurations with the X-point below or above the magnetic axis are possible, called upper and lower single null shape respectively. With the standard toroidal magnetic field, the upper single null configuration has an unfavorable ∇B-drift. This results in a higher energy threshold needed to reach H-mode, meaning that it has worse performance [35]. However, many of the discharges analyzed were made to specifically measure turbulence and staying in L-mode even with higher heating is a useful feature.

AUG further distinguishes itself by having all tungsten plasma-facing components. Tungsten is relevant for future fusion reactors as Carbon can not withstand the large heat flux and retains the hydrogen isotopes. Unfortunately, tungsten is never completely ionized, making the high Z-material an important radiation source. Often, an ECRH source is used to limit tungsten accumulation and avoid a disruption [64].

3.1. Heating

Before turbulence was identified as the major driver of heat transport, it was hoped that tokamaks could be solely heated by the toroidal current running through the plasma. However, the resistivity of the plasma scales with $T^{-3/2}$ so that reaching reactor-relevant temperatures purely with this "Ohmic heating" is impossible. Instead, AUG can use three auxiliary heating systems named Neutral beam injection (NBI), Electron cyclotron resonant heating (ECRH) and Ion cyclotron resonant heating (ICRH).

The NBI consists of a maximum of 8 beam sources, each providing up to 2.5MW of heating power. Positive ions are sped up in an accelerator and are neutralized in a deuterium gas cloud in order to enter the magnetized plasma. The beam is ionized continuously while moving through the plasma, leading to a prolonged heating curve. Besides heating the ions and electrons, some of the NBI beams also provide rotational torque to the plasma. Increasing the toroidal velocity can have several positive effects. The radial electric field E_r is positively dependent on v_{tor} [100], and an increase in $E \times B$ shear is known to suppress transport by tearing turbulent eddies apart [38]. Furthermore, higher toroidal rotation can protect the

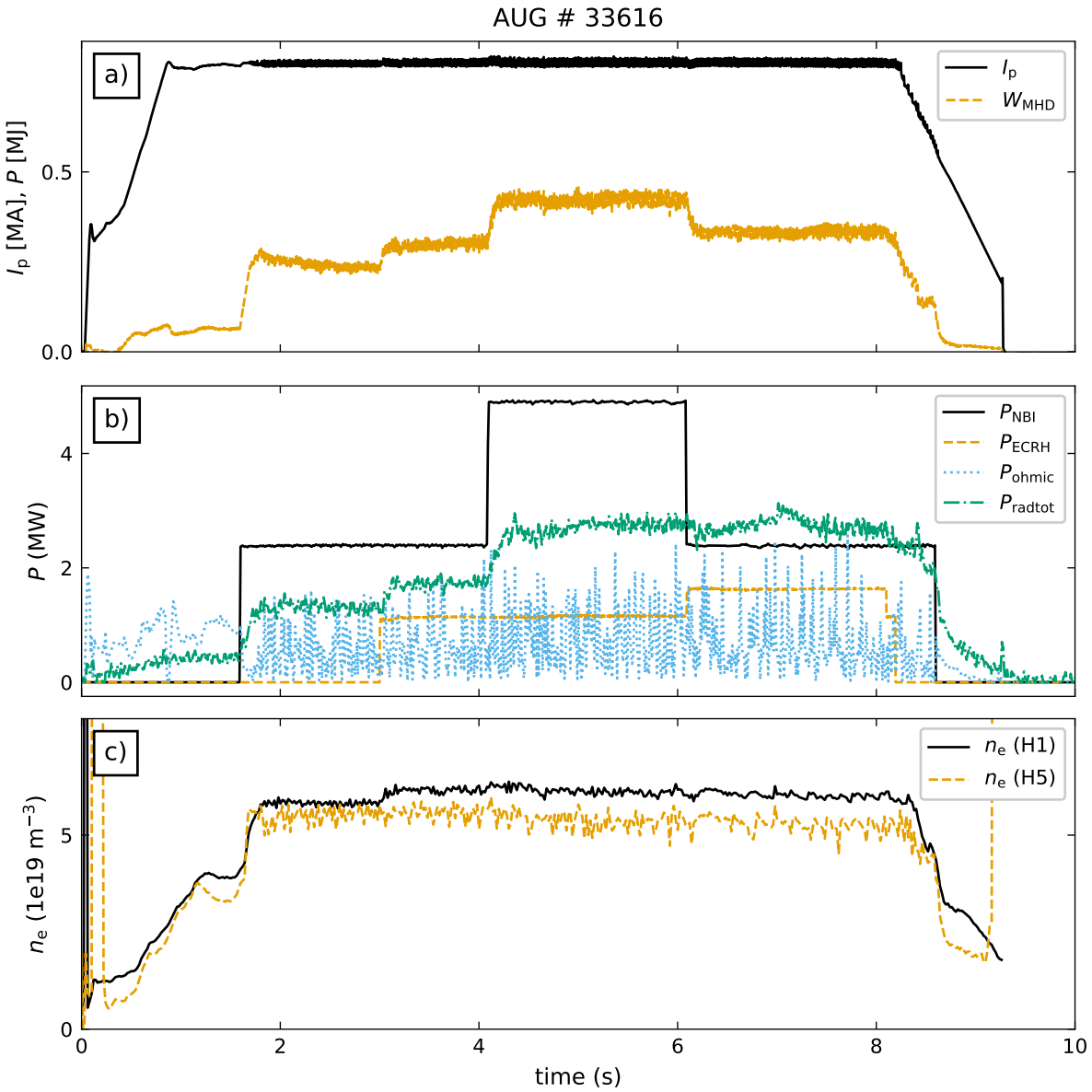

Figure 3.1.: Time trace of a H-mode discharge #33616. After the current reaches flattop at around 1s, the NBI heating at around 2s is enough to reach H-mode, which is visible by the sudden rise in the density seen in the DCN interferometry channels H1 and H5. At 4s, the heating was roughly doubled, with the stored energy W_{MHD} only rising by about 33%, further illustrating the problem with stiff transport.

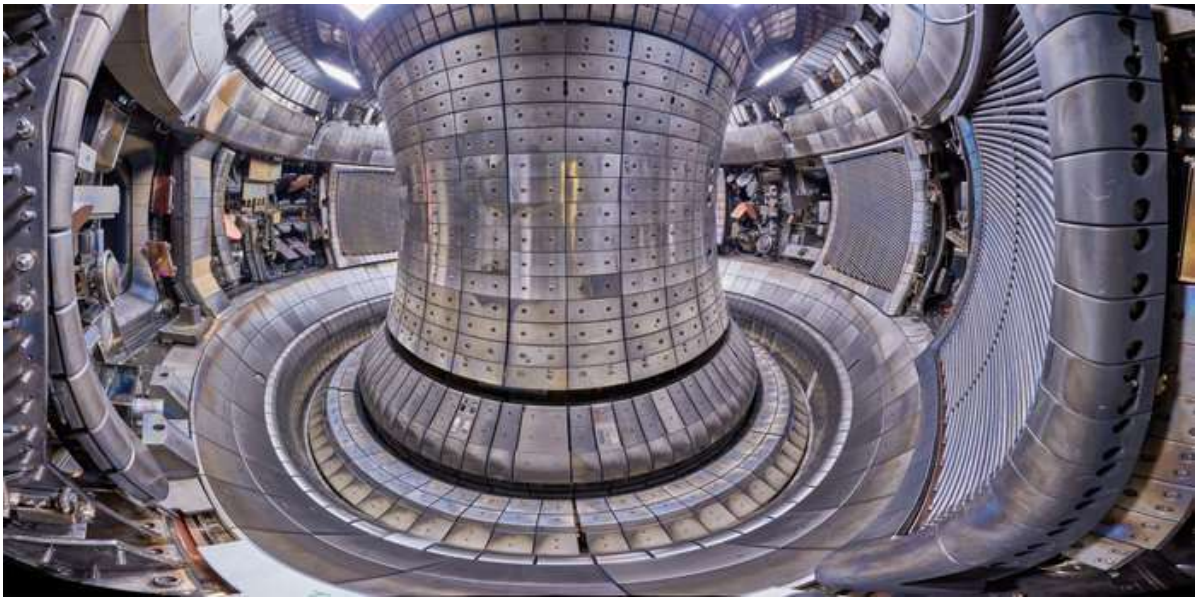

Figure 3.2.: Fishlensview of the ASDEX Upgrade tokamak taken from [99]. The tungsten plasma-facing components make the tokamak an important testing ground for reactor-relevant discharges, with the downside that tungsten can radiate a lot of the plasma energy away and can be a challenge for diagnostics due to reflections.

plasma against mode locking and avoid disruptions [101]. As the beam's momentum is transferred to the ions, they drive a net current, which replaces fractions of the ohmic current from the transformer and could allow continuous tokamak operation. Lastly, the NBI also provides critical measurements as the NBI excites impurities whose radiation gives feedback on ion temperature, rotation and effective charge Z_{eff} (see subsection 3.2.4 Charge exchange spectroscopy[CXRS]).

The ECRH systems can be considered to be 8 powerful gyrotrons, which can provide a total of 8MW. The waves have a frequency of either 105GHz or 140 GHz to avoid the cut-off frequency (explained in 3.2.2) and thus usually heat the second harmonic of the cyclotron frequency. The heating area is narrowly focused, making it possible to change heat fluxes and temperature gradients in a more controlled way than the NBI. The ECRH mainly heats the electrons but is also important to avoid impurity accumulation. ECRH is known to raise impurity transport coefficients and to diminish an inward convective pinch [102].

The ICRH system is similar to the ECRH, but due to the larger antennas, the heating curve is much broader and heats both electrons and ions. The coupling of the heating waves with the plasma is more complicated than for the ECRH. ICRH discharges are especially interesting from a turbulence perspective as the heating results in fast ions, which can both stabilize and destabilize turbulent modes. TORIC [103] is a routine capable of simulating the ICRH. However, for now, it is only available for TRANSP, which makes the ASTRA simulations more cumbersome.

ASDEX Upgrade can be fueled by gas valve or pellet [104]. There are numerous gas valves at different poloidal and toroidal locations that can inject neutrals into the scrape-off layer [105] at more than 10^{22} particles per second. The ice pellets are injected into the plasma from the high field side. The pellets can include up to $4 \cdot 10^{20}$ atoms. While the pellet's neutrals can reach rather central radial positions (e.g. $\rho_{pol} \approx 0.6$ [106], neutrals stemming from gas puffs usually are ionized outside of $\rho_{pol} = 0.95$ [55].

3.2. Diagnostics

At ASDEX Upgrade, various diagnostics exist to measure the plasma parameters. Here, the thesis-relevant diagnostics for temperature and density are briefly explained.

3.2.1. Deuterium Cyanide Interferometry

The Deuterium-Cyanide Interferometry (DCN) measures the line-integrated electron density n_e by measuring the phase difference between a reference beam and a beam going through the plasma. This line-integrated density data is then fed to IDA and compared to its forward model. The phase difference $\Delta\Phi$ is given by

$$\Delta\Phi \propto \int_{LOS} n_e(x)dx. \tag{3.1}$$

At AUG, five lines of sight (LOS) exist with a sampling rate of 10 kHz, allowing for a rough density profile reconstruction by themselves. One can assume that the measurement error is smallest where the LOS is parallel to a field line as it covers the most distance with a similar density there [16].

During strong changes in density and thus refraction index, there may be a mistake in measuring the phase difference by a multiple of 2π [107]. These changes can be due to ELMS, disruptions or intentional events such as pellet injection.

3.2.2. Electron Cyclotron Diagnostic

The Electron Cyclotron Emissions is used to measure the electron Temperature T_e. The gyrating electrons radiate energy at the electron cyclotron frequency and its harmonics $\omega_n = \frac{neB}{m_e}$ and as the toroidal magnetic field decreases with major radius $B \propto 1/R$, the frequency is specific for one radial location. If the plasma density is high enough, the light will be reabsorbed inside the plasma and finally emitted as black body radiation. Using the Rayleigh-Jeans law, the measured intensity of black body radiation I_{ω_n} will let diagnosticians determine the temperature [108, 109].

$$I_{\omega_n} = \frac{\omega_n^2 T_e}{8\pi c^2} \tag{3.2}$$

ECE measurements rely on a correctly reconstructed equilibrium to map the measured temperatures to the right position in the tokamak. A bad equilibrium fit can be spotted when

the ECE measurements exist on the low and high field side and thus, two measurements exist for the same flux surface. A similarly looking mismatch can happen in cases of high electron temperature but low density when radiation transport effects cause a "Pseudo radial displacement" in which case a higher fidelity forward model needs to be used [109].

A problem with the ECE diagnostic is the cut-off frequencies. If an electromagnetic wave travels at frequencies lower than the plasma frequency:

$$\omega_p = \sqrt{\frac{n_e e^2}{m_e \epsilon_0}}, \tag{3.3}$$

the electrons will move like a dipole with the wave, thus shielding it. In high-density discharges, it can occur that no ECE measurements are available as the high-harmonics are not reabsorbing the cyclotron frequency, and the low harmonics are below the cut-off frequency.

Overall the ECE diagnostic is the most reliable diagnostic for T_e due to its high-sampling rate of 1MHz [110].

ECE radiometry relies on the mixers to measure the radiation at certain frequencies. Gaps can appear in the radial distribution of ECE measurements depending on how the mixers are set.

3.2.3. Thomson scattering

The Thomson scattering diagnostic is based on light from an Nd:YAG laser being scattered of free electrons to measure electron density and temperature. When monochromatic light interacts with a moving electron, it undergoes spectral shifting caused by the Doppler effect. This scattering process results in a broad spectrum of scattered light due to the velocity vector variation among an ensemble of electrons. The electron temperature can be determined by measuring the scattered light's spectrum and assuming a Maxwellian distribution. As the amount of scattered light is proportional to the local electron density, it can be used as a density diagnostic. The Thomson scattering system is made up of 4 core and 6 edge lasers which can each shoot pulses with a rate of 20Hz [111].

To counteract problems such as the measurements being shifted on the same coordinate system, the core Thomson density measurements are scaled in IDA to match the DCN measurements. Even with its low-frequency sampling rate, the core TS diagnostic is the main profile gradient predictor for the density. This is also the case for T_e if the ECE is not available e.g. due to cut-off.

3.2.4. Charge exchange spectroscopy

Charge Exchange Spectroscopy is often the only method of determining the ion temperature and rotation [112]. As the fast neutral deuterium atom collides with an impurity, it transfers the electron to the impurity. The atom's electron is then in an excited state and radiates as it drops to a lower state. The exact wavelength of the radiation depends on the excited impurity

and the states of the electron. Through the radiation line intensity, one can determine the density of the impurity. Similar to the Thomson diagnostic, one determines the impurity temperature by recording the Doppler-shift broadening and even the toroidal rotation by examining the Doppler shift. In general, it is assumed that all ion species are in equilibrium with each other and thus have the same temperature. The data is determined in rates of 5ms in the core and 2.3ms at the edge.

If CXRS measurements are needed without heating the plasma with NBI, the neutral beams are sometimes only turned on in short blasts called blips. While this does result in measured data, it can also come at the cost of a small signal-to-noise ratio [113].

3.2.5. Lithium beam

The lithium beam is used to measure the electron density at the edge [114, 16]. Similar to the CXRS, the radiation of excited lithium atoms is measured along the lines of sight. The emission profile of one Li emission line is forward modeled by a collisional radiative model, which lets the diagnostician infer the density profile with a typical rate of $50\mu s$. As the lithium beam is quickly ionized, it is only available at the edge. A higher density will lead to a quicker ionization and thus a smaller radial space.

The lithium beam's importance is emphasized in that conducting a density analysis using solely relying on the DCN data is difficult due to a lack of data regarding the density shape at the plasma edge. The two outermost DCN channels, which have minimum ρ_{pol} values of 0.6 and 0.8, are insufficient for accurately determining the density at the plasma edge [16].

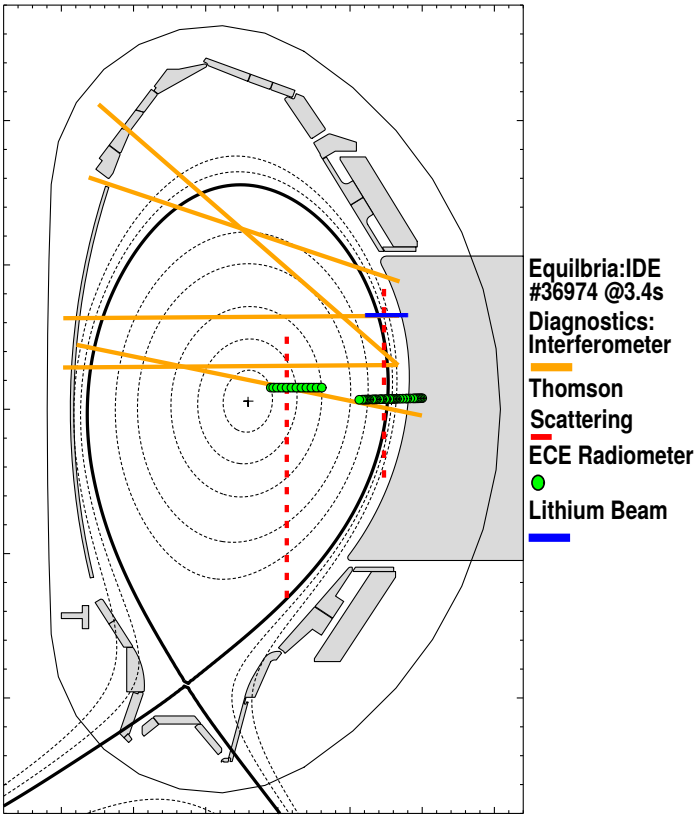

Figure 3.3.: Diagnostic distribution for the L-mode discharge #36974. One can see that the diagnostics are not covering the entire parameter space. Depending on the discharge, the equilibrium can look vastly different, which changes the ρ that is being measured. Also the shown ECE gap shown here is not present in every discharge but hinges on the mixers.

3.3. Integrated Data Analysis

The Integrated Data Analysis framework is the primary tool in fitting electron density n_e and temperature T_e profiles at ASDEX Upgrade using the diagnostics mentioned above. Similar concepts have been implemented at JET [115] and other tokamaks and it is further planned to be implemented in the future ITER tokamak.

3.3.1. Bayesian probability theory in IDA

As can be seen in figure 3.3 the diagnostics are not capable of covering the entire plasma parameter space. Thus, IDA incorporates a Bayesian probability theory (BPT) and solves for the maximum a posteriori (MAP), which is the most likely profile combining the probabilities of the different diagnostics and well-chosen priors.

In BPT, the posterior probability distribution function (pdf) $p(\Theta|d)$ is the probability for an outcome Θ given some data d and having some background information I. It is calculated

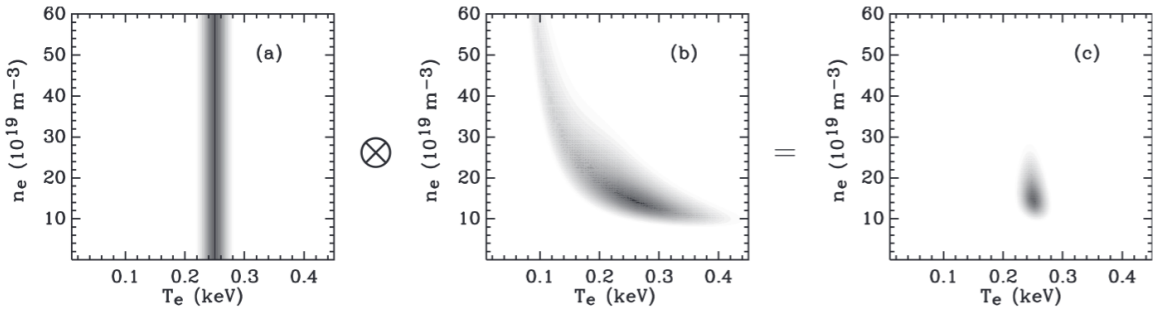

Figure 3.4.: The marginal posterior distributions for electron temperature and density for a spatial position at Wendelstein 7-AS stellarator, taken from [121]. (a) illustrates the pdf corresponding to the Te measurement using soft X-ray, (b) shows the pdf from Thomson scattering data, and (c) displays the posterior resulting from the combination of both likelihoods.

using the likelihood $p(d|\Theta)$, the prior $p(\Theta)$ and evidence $p(d)$

$$p(\Theta|d, I) = p(d|\Theta, I)p(\Theta|I)/p(d|I). \tag{3.4}$$

The evidence normalizes the posterior to pdf and does not affect the shape of the pdf and, therefore also not the MAP location. Thus this scaling factor is usually dropped when maximizing the posterior with regard to Θ. The prior quantifies relevant additional information that is available independent of the data [116] and can have different complexity ranges. BPT is explained in more detail in [117]. It is important to keep the implicitly used background information in mind when running the calculation and presenting the results. For brevity, it is dropped in the further discussion.

The probability that needs to be maximized in IDA is thus just the product of the four likelihoods from the diagnostics and the multiple priors (here shown as one):

$$\begin{aligned} p(n_e, T_e|d_{LIB}, d_{DCN}, d_{ECE}, d_{TS}) \propto\ & p(d_{LIB}|n_e, T_e) \\ & \times p(d_{DCN}|n_e) \\ & \times p(d_{ECE}|T_e, n_e) \\ & \times p(d_{TS}|n_e, T_e) \\ & \times p_{prior}(n_e, T_e) \end{aligned} \tag{3.5}$$

There is no limit to the potential number of diagnostics used as the product can just be expanded. At AUG, the reflectometry (measuring the edge density [118]) and helium beam (measuring edge density and temperature [119, 120]) are also regularly being utilized.

Calculations with the pdfs can be simplified by optimizing for the maximum negative logarithm. This particular choice turns Gaussians into parabolas, and the logarithm of a product is the sum of the individual logarithms. This is also beneficial for numerical processing with finite precision due to the probabilities dropping rapidly to zero away from the mode of a distribution.

By maximizing the sum of the different log-likelihoods, IDA considers interdependencies that are difficult to take into account in the traditional way of profile fitting. For example, creating temperature results directly from the ECE data alone would require some assumptions of the density profile and most likely some smoothing to reduce noisy data during the inversion process. Taking the uncertainty of the density input into account would be challenging and becomes even more difficult as more diagnostics are added. IDA is able to avoid this by applying the different forward models to the same proposed profile and calculating the probability.

An impressive example of combining diagnostics is the reduction of uncertainty for the density profile of W7-AS shown in figure 3.4, which was taken from [121, 16]. Even though the soft X-ray diagnostic measures no density information, by combining it with the Thomson Scattering measurements and thus limiting the parameter space of the TS, the users are able to reduce the uncertainty of the density profile by 30%.

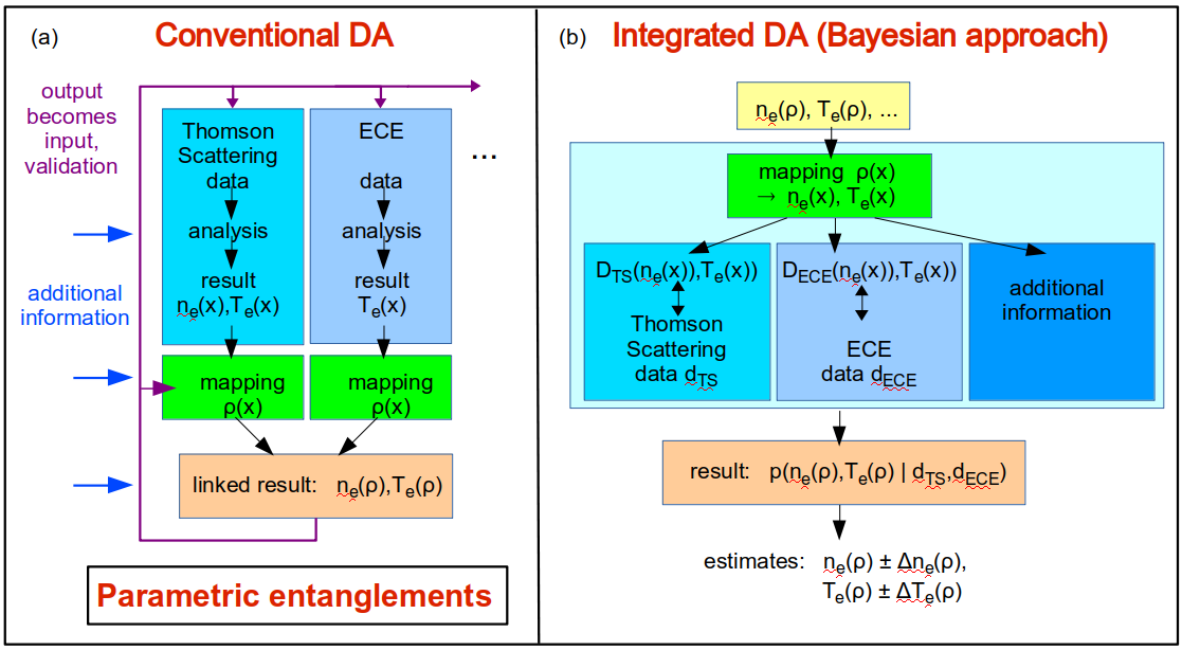

Figure 3.5.: Flow chart of the IDA framework compared to a regular method of data fitting. Simultaneously optimizing the different diagnostics makes it possible to take interdependencies into account and reduce the profile uncertainties. Figure taken from [122].

3.3.2. Profile model

In IDA, the n_e and T_e profiles are represented using the exponential of cubic splines S using the ρ_{pol} coordinate system. For example,

$$T_e(\rho_{pol}, Y) = exp(S(\rho_{pol}, Y)), \tag{3.6}$$

with Y being the spline height at the spline point. This representation naturally enforces positivity constraints. The splines position is given nonuniformly with fewer spline points in the core than towards the scrape-off layer. This way, the strong gradient at the separatrix and the relatively smooth core profile can be captured. The electron density is fitted with 14 and the electron temperature with 19 spline points, whose positions are determined before the fitting procedure is started and shown in figure 3.6. The spline point positions are usually kept unchanged between different fits.

Two models are utilized to establish a connection between the measured data and the fitted profiles: a statistical model and a forward model.

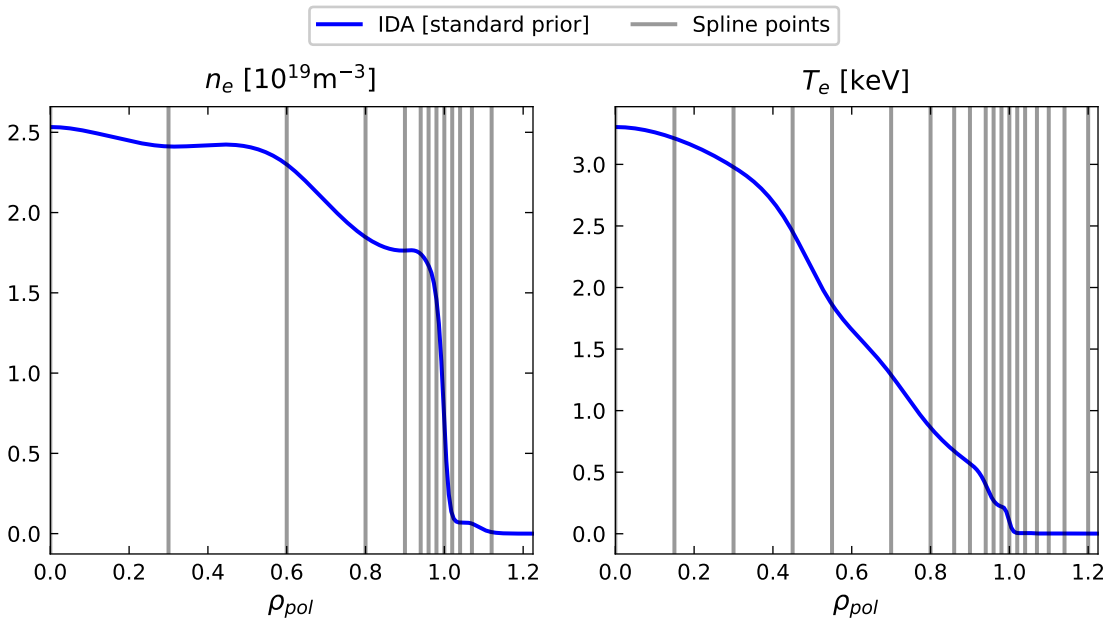

Figure 3.6.: Spline point distribution for the density and temperature profiles. The distribution of 14 points for density and 19 for T_e is usually kept the same for every analysis, with a more points at the edge due to the strong gradients. The IDA profiles used in [123, 87] removed spline points to achieve additional smoothing.

3.3.3. Forward model

The forward model of a diagnostic calculates synthetic data for specific parameter values. This model encapsulates the physical aspects of the measurement process, as well as the setup and calibration procedures. The synthetic data can then be compared to the real measured data. The use of forward models generally suffers less from noise fitting than backward inversion techniques. Data pre-processing steps such as calibration or background subtraction are typically integrated into the forward model for exhaustive error handling.

IDA gives the user a free choice between 5 ECE forward models in which the simplest

assumes black-body radiation and thus $T_e = T_{rad}$, while the most complex is the ECrad model from [109]. Typically, at AUG, the second highest-fidelity ECE forward model is used, which considers Doppler and relativistic effects. The other diagnostics have their set forward models.

3.3.4. Statistical model

The statistical model comprises statistical and systematic uncertainties by characterizing the distribution of measurement uncertainties and accounting for potential errors in the data acquisition process. The uncertainties are crucial as they determine how strongly each diagnostic is weighted. Systemic uncertainty can be included as a prior dependent on a nuisance parameter and can be integrated out. As an example, if there is some uncertainty about the atomic data A_i used for the Lithium beam, then $p(d_{LIB}|n_e, T_e) = \sum_i p(d_{LIB}, A_i|n_e, T_e)$. The statistical uncertainty is assessed with the chosen likelihood pdf. In IDA, the diagnostics are either fitted with a Gaussian or Student's t-distribution.

In the ECE's case, the Gaussian log-likelihood is proportional to $\propto ((T_e - d_{ECE})/\sigma_{ECE})^2$ and the logarithm of the Student's t-distribution $\propto (a_0 + 0.5) \times ln(2a_0 + ((T_e - d_{ECE})/\sigma_{ECE})^2)$ with d_{ECE} being an ECE measurement, the data uncertainty given by the standard deviation σ_{ECE} and a_0 determining how large the tails of the Student's t-distribution are (see Figure. $a_0 = 0.5$ represents a Cauchy pdf, while for $a_0 \to \infty$ a Gaussian is recovered. The more outlier robust Student's t-distribution is especially practical in cases where the uncertainty was chosen to be too small due to (forward) models having incomplete physics. This is again shown in section 5.4.

3.3.5. Priors

A prior is the initial belief or knowledge about the probability distribution of a parameter before incorporating new data or evidence. It represents what is known about the parameter before any data has been observed. Priors are crucial in determining the plasma profile if some of the aforementioned diagnostic problems occur. A sensible first prior is that IDA excludes negative densities or temperatures by having the profiles be the exponential of the cubic splines. Other default priors are used with comparably wide distributions to not bias the MAP location when sufficient data are available.

In most cases, assuming that the plasma gets denser and hotter the closer one gets to the magnetic center is sensible. In a tokamak, a non-monotonic density and/or temperature profile could be achieved via pellet injection, strong core radiation, sudden off-axis heating or during the ramp-up. Figure 3.8 shows a discharge during ramp-up with a hollow T_e profile. For these reasons, the monotonicity priors in IDA have some leeway. The discharge was made hollow by design to decrease Landau damping and study the effects of energetic particles [124]. The fit to the recorded ECE and Thomson scattering data is decreased by a stronger monotonicity prior than usually used.

The likelihood formula for the monotonicity prior is given in [114] as

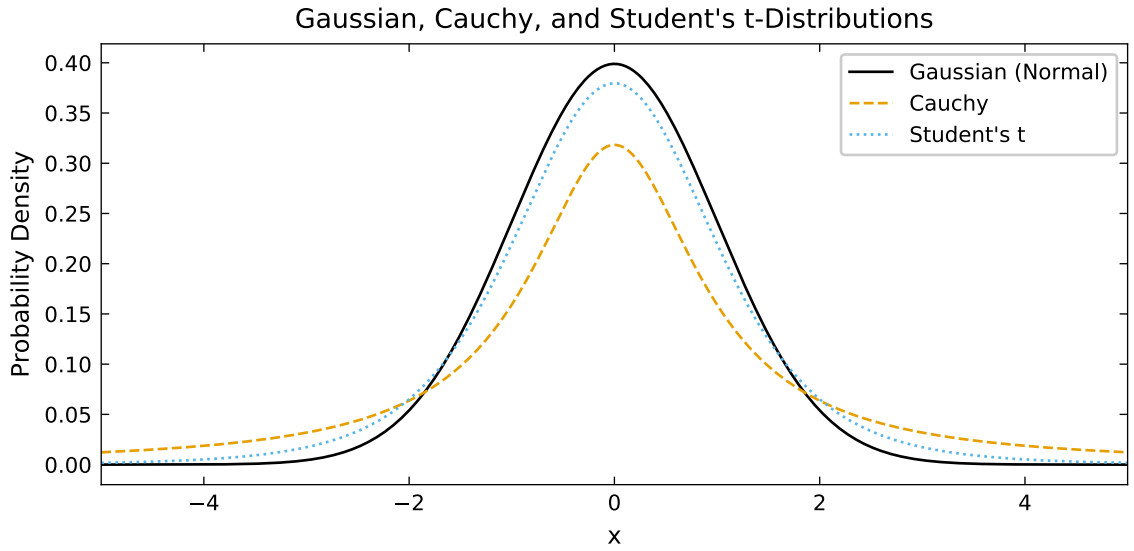

Figure 3.7.: Comparison of Gaussian, Cauchy and Student's t-distributions with $a_0 = 5$. The Cauchy pdf is equivalent to a Student's t-distribution with $a_0 = 0.5$. The smaller a_0, the less outliers are punished in the IDA framework.

$$p(\Theta) \propto \begin{matrix} \exp\left\{ -\sum_{i=1}^{N-1} \frac{(\Theta_{i+1}-\Theta_i)^2}{(\Theta_{i+1}+\Theta_i)^2 s_g^2} \right\} & \text{for } \Theta_{i+1} < \Theta_i \\ 1 & \text{elsewhere,} \end{matrix} \tag{3.7}$$

where s_g is a scaling factor that decreases penalization if it is increased.

The curvature prior influences a profile's second derivatives and contributes to a certain smoothness [125]. This thesis shall mostly focus on the curvature prior due to its influence on the gradient.

In figure 3.9, one can see three IDA profiles all fitted on the same data with a less or more strict curvature prior. In the top row, one can see the density and temperature with the diagnostic data. Below one can see the logarithmic gradients $\nabla ln(T_e) = \frac{\nabla T_e}{T_e}$. The profiles are very similar where experimental data is available. However, the gradients of the three profiles are vastly different in the ECE gap at $0.4 \leq \rho_{tor} \leq 0.7$. While these profiles do a good job of fitting the experimentally measured data, the resulting profiles can have gradients that are too large to fit with the current understanding of transport physics.

As shown in the transport chapter, turbulent transport is driven by the logarithmic gradients of profiles. A simple check is to examine the power balance of the discharge. Using ASTRA-TGLF in interpretative mode, meaning not developing the profiles, in figure 3.10 it is shown that the transport driven by the gradients does not match the power balance attained by volume integrating the heating sources. As the discharge only used a single ECRH source at around $\rho_{tor} = 0.2$, the expected heat flux should be close to a straight line outward. However, the heat flux shoots up at the position of the largest T_e log gradient. This overestimation is

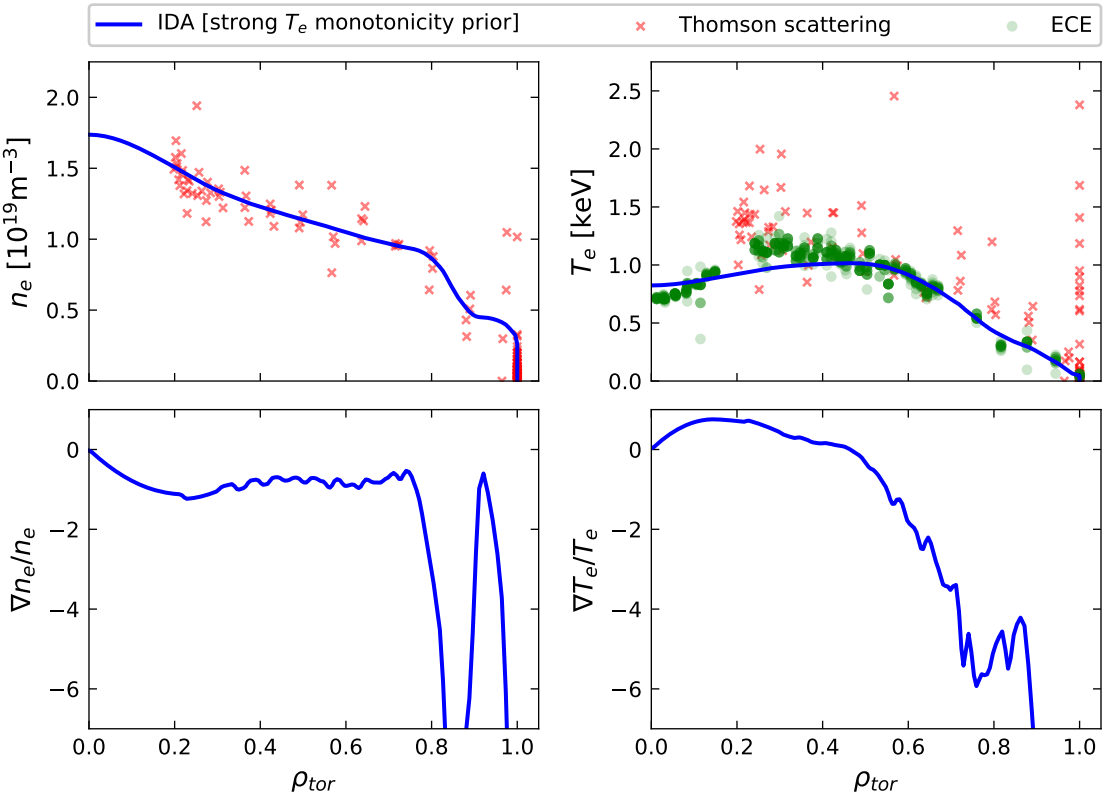

Figure 3.8.: IDA profile of discharge #31213 at 0.84s. The profile has a non-monotonically rising T_e profile. Due to the strong penalization of the monotonicity prior, the fit to the recorded data is not satisfactory, with the residuals not scattering around 0 in the core.

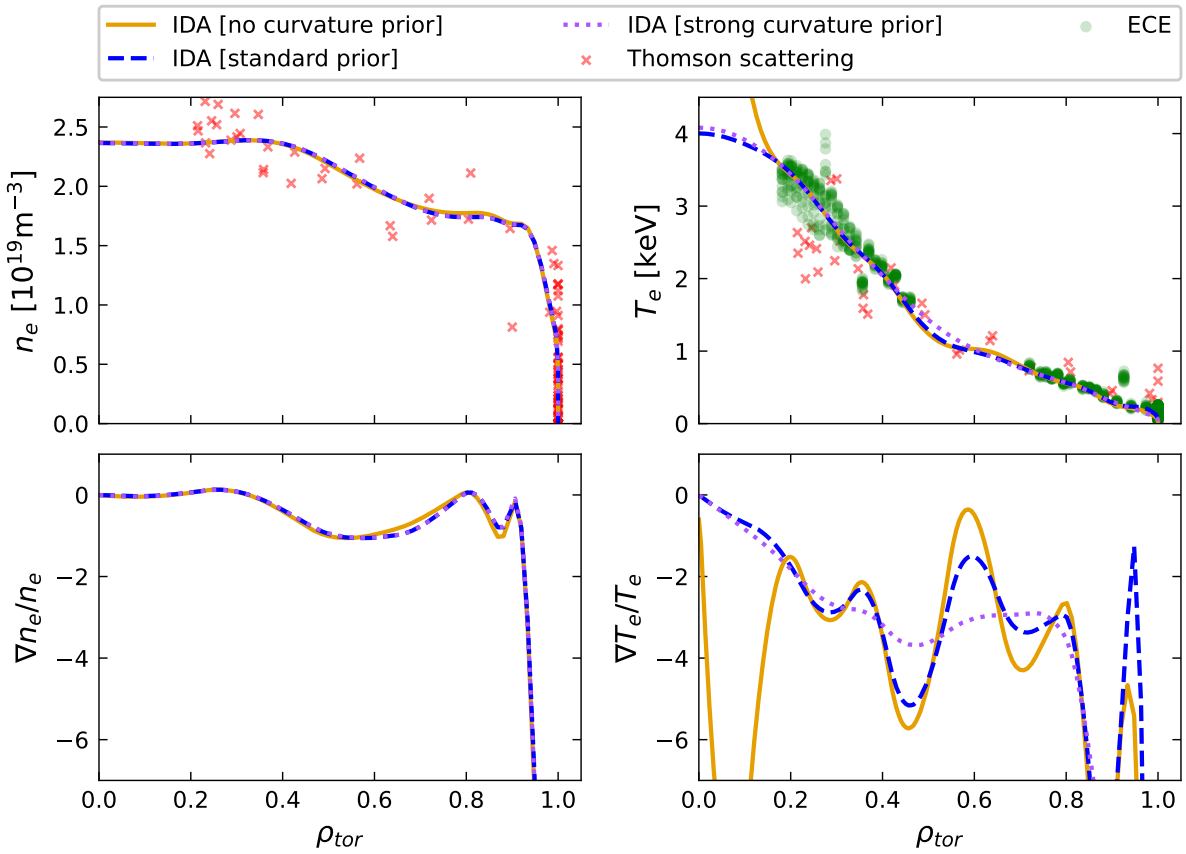

Figure 3.9.: Three IDA profiles using different strengths of the curvature prior all fitted on the same diagnostic data from the L-mode discharge shown in 3.3. While all profiles fit the data, one can see that the priors greatly impact the temperature gradient in the ECE gap at around $\rho_{tor} = 0.6$ and that the curvature prior prevents the temperature from rising to unrealistic heights in the core. The Thomson scattering measurements are depicted as red crosses, while the more frequently sampled ECE measurements are shown as green circles.

also present for the stronger curvature prior, although slightly reduced. However, such a strict prior has been known to overrule diagnostics and is thus not wanted. The mismatch in the power balance motivates a new physics-informed prior created by using ASTRA-TGLF simulations.

3.3.6. Uncertainty of IDA profiles

Section 4.2.1 shall introduce input uncertainty propagation to ascertain the sensitivity of the kinetic model. IDA profile's uncertainty is given by locally changing the profile until the residual of the likelihoods has increased by 1 [113]. For this method, the profile is divided into bins and the profile is changed by a triangle-like shape with a basis of about $\Delta\rho_{pol}$=0.05. This uncertainty approach gives the user an estimate of the information density of the measured data. In IDA profiles, one can thus frequently see the uncertainty shoot up in the very center

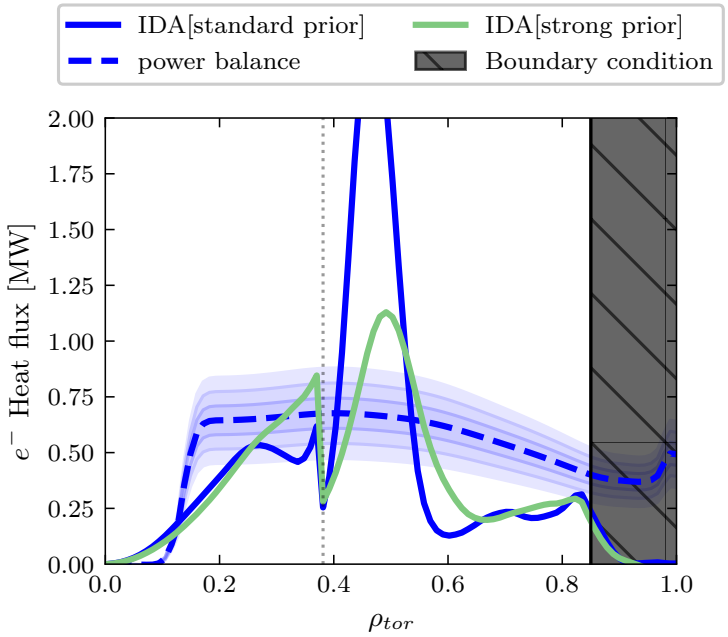

Figure 3.10.: Heatflux calculated by TGLF and NCLASS by running ASTRA interpretively with two IDA profiles from figure 3.9. The strong T_e gradients in the ECE gap drive stronger turbulence than one would expect from the power balance. The faintly dotted line is the q=1 surface for which stronger diffusion coefficients are given.

where diagnostics are often absent. This uncertainty is thus not suitable for input uncertainty propagation of kinetic models.

IDA can also be used with a Markov Chain Monte Carlo (MCMC) Metropolis-Hastings [126, 127] algorithm, which converges up to 1000 times slower but gives more realistic profile uncertainties. Monte Carlo algorithms are further described in [117]. In the IDA-MCMC profiles, the mean of the 10^6 samples is defined as the profile and the standard deviation of the samples as the uncertainty. The MCMC profile uncertainty is often smaller than that of MAP since the entire correlation structure of the posterior pdf is taken into account [113]. The same can be done for the gradients of the samples, which is not the same as taking the gradient of the mean profile. In most cases, the two will, however be fairly similar.

The MCMC fitting method provides gradient uncertainties that can be used in kinetic simulations but requires extra care from the user. Potential problems include but are not limited to:

- Convergence Issues: One of the primary concerns with MCMC is ensuring that the chain has reached its stationary distribution (converged) and is not stuck in a transient state. Convergence issues can lead to biased or inaccurate estimates of the target distribution.
- Burn-in: In some cases, it may take a certain number of initial iterations (burn-in) for the chain to reach the stationary distribution. Discarding these initial samples is common

practice to reduce the impact of the starting point on the posterior estimates.

- Auto-correlation: MCMC samples can be auto-correlated, which can lead to underestimation of uncertainty and inefficiency in the estimation process.

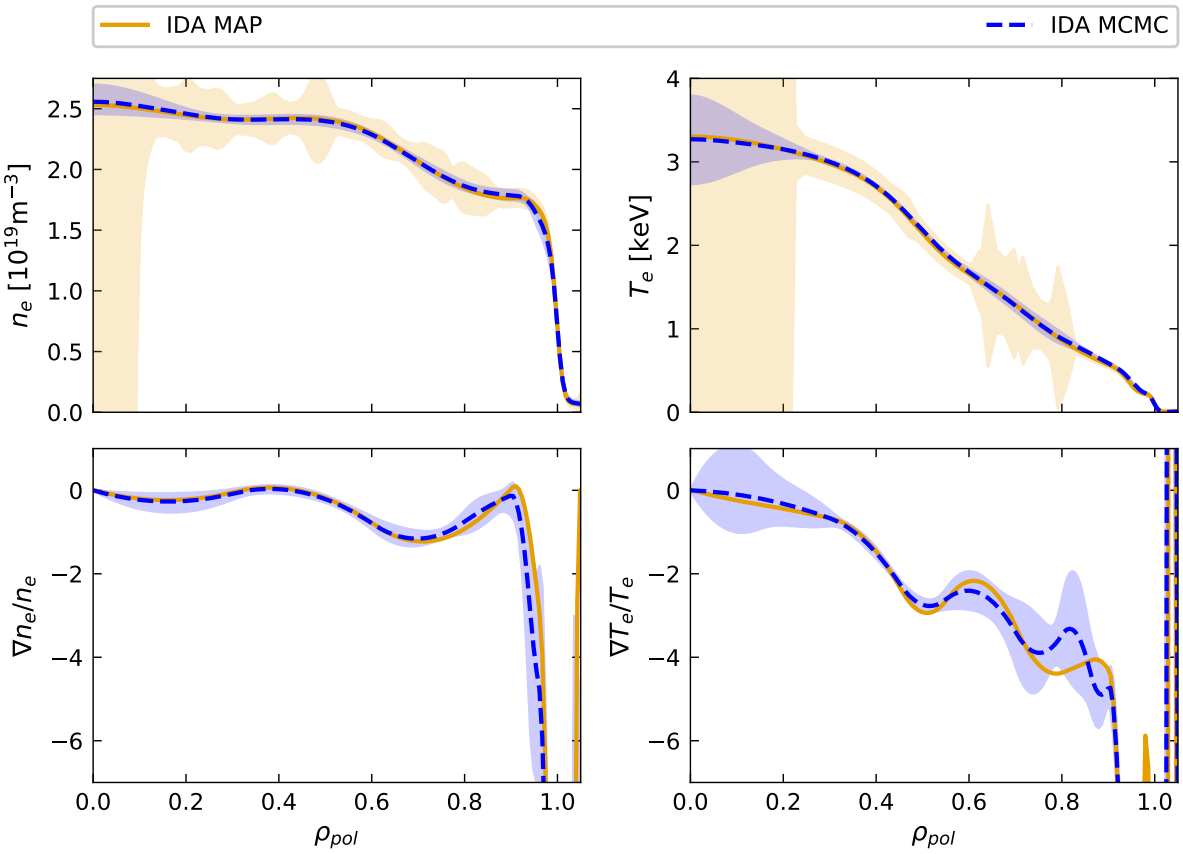

Figure 3.11.: Comparison of MAP and MCMC methods for IDA discharge #36770. The MCMC method computes its uncertainty from the standard deviation of drawn samples, thus making it possible to give realistic error bars for the gradients. However, it is a lot slower.

Furthermore, the amount of spline points can make a large difference not just in the profile shape but also in the uncertainty. For the GENE validation studies shown in section 5.2, IDA-MCMC profiles were made with reduced spline points to achieve additional smoothing. This had the additional effect of smaller variations between the drawn samples, thus leading to smaller error bars. To properly assess which number of splines are needed, the evidence of equation 3.4 would have to be calculated for a number of models with different numbers of spline points and locations. This is not feasible for routine analysis but should be part of further studies.

3.3.7. Other data analysis frameworks at AUG

At ASDEX Upgrade, Integrated Data Analysis is not only used for electron density and temperature profiles. The following are some other experimental shotfiles that are later used in the kinetic modeling section as input.

IDI [113] uses Gaussian Process Regression [128] to fit CXRS data for ion temperature measurements and toroidal velocities. The covariance Kernel is varied between the data at the edge and core to reflect the expected gradients. GPR is fast for the interpolation of noisy data, making it ideal for the already analyzed CRXS measurements. IDI also has some gradient expectations already implemented, as there can be a lack of data close to the magnetic axis or separatrix. This could be further extended with the gradient information of the ASTRA-TGLF model.

GPR is not used for the electron profiles due to the non-linearity of the ECE and lithium beam forward models. In addition, GPR is known to have issues with outlier-rich data, which is unsuitable for Thomson scattering but could perhaps be solved with a process regression based on a Student's t-distribution.

IDZ combines the line radiation from CXRS and Bremstrahlung measurements [129]. IDZ is usually calculated along with IDA to incorporate uncertainty coming from density and temperature measurements.

IDE [130] solves the Grad-Shafranov equation with additional pressure constraints being the neoclassical current diffusion equation (CDE) and the Kadomtsev reconnection model [131, 113]. IDE can also consider fast-ion profiles, which are either calculated by RABBIT or TRANSP/TORIC in the case of ICRH. For now, IDA and IDE can not be solved simultaneously, so in cases where the equilibrium greatly changes the profile, both codes need to be iterated to achieve converged results.

As the equilibrium is important for matching the lines of sight to the flux surfaces, an IDE equilibrium was used for all IDA fits in this thesis. IDA uses ρ_{pol} as its coordinate system, while ASTRA-TGLF uses ρ_{tor}. In figure 3.12, one can see that the choice of equilibrium can have a strong effect on the mapping between coordinate systems.

For the kinetic model, all of these integrated processes are used as input, but the simulation only feeds information back to the electron density and temperature IDA framework. With some tweaks to the kinetic model, impurities and currents could be simulated, which could act as priors to the various frameworks.

The need for a kinetic modeling prior has been motivated in this chapter. In chapter 4, the thesis shall introduce the uncertainty quantification needed to calculate the probability density function in chapter 5.

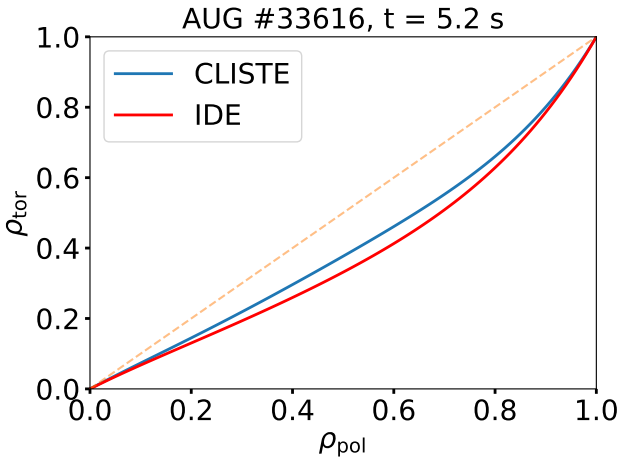

Figure 3.12.: Depending on the equilibrium used, the conversion ρ_{pol} to ρ_{tor} may differ greatly and thus also impact comparisons of gradients. For this thesis an IDE equilibrium is always used to get the best possible mapping of diagnostics to the equilibrium.

4. Uncertainty quantification in ASTRA

To be able to formulate a likelihood of the kinetic modeling prior, it is necessary to determine the uncertainty of the simulation. Unfortunately, all subroutines of ASTRA are deterministic and give no information about their confidence intervals. This chapter first introduces error bars based on personal experience, then moves on to an input-sensitivity analysis of the ASTRA-TGLF model. Finally, it analyzes different sources of possible errors in the model itself.

4.1. Predetermined uncertainty based on region

As a proof of concept, it was decided to define an uncertainty for the gradients at certain radii based on our experience of running different discharge scenarios listed in tables 5.2 and 5.3.

Table 4.1 shows the regions and their uncertainties chosen for a simulation with a boundary condition at $\rho_{tor} = 0.9$. If it was necessary to move the ASTRA-TGLF boundary condition inwards, the 75% and 25% uncertainty region was moved accordingly.

$$\sigma(\rho_{tor}) = \begin{cases} 400\%, & \text{for } \rho_{tor} \in [0.00, 0.15) \\ 100\%, & \text{for } \rho_{tor} \in [0.15, 0.20) \\ 50\%, & \text{for } \rho_{tor} \in [0.20, 0.35) \\ 10\%, & \text{for } \rho_{tor} \in [0.35, 0.80) \\ 25\%, & \text{for } \rho_{tor} \in [0.80, 0.85) \\ 75\%, & \text{for } \rho_{tor} \in [0.85, 0.90) \\ 125\%, & \text{for } \rho_{tor} \in [0.90, 1.00] \end{cases} \tag{4.1}$$

In figure 4.1, an implementation of the predetermined uncertainty is presented for the L-mode discharge #36974. The experimental gradients of n_e and T_i are within the error bars, while the simulated T_e log gradient matches IDA except in the region where the overly strong gradient variation was observed due to the ECE gap.

In some cases, an overpredicted density can have a stronger negative effect on the temperature gradients. A higher density means that the heating power is diluted over more particles and that, overall higher amounts of impurities radiate more. For these cases, an optional additional uncertainty has been implemented in which the line-averaged density can be compared to that of the experimental profile. The comparison of line-averaged density is not refined enough to have an impact on the profiles shown in this thesis so it was not utilized for this thesis.

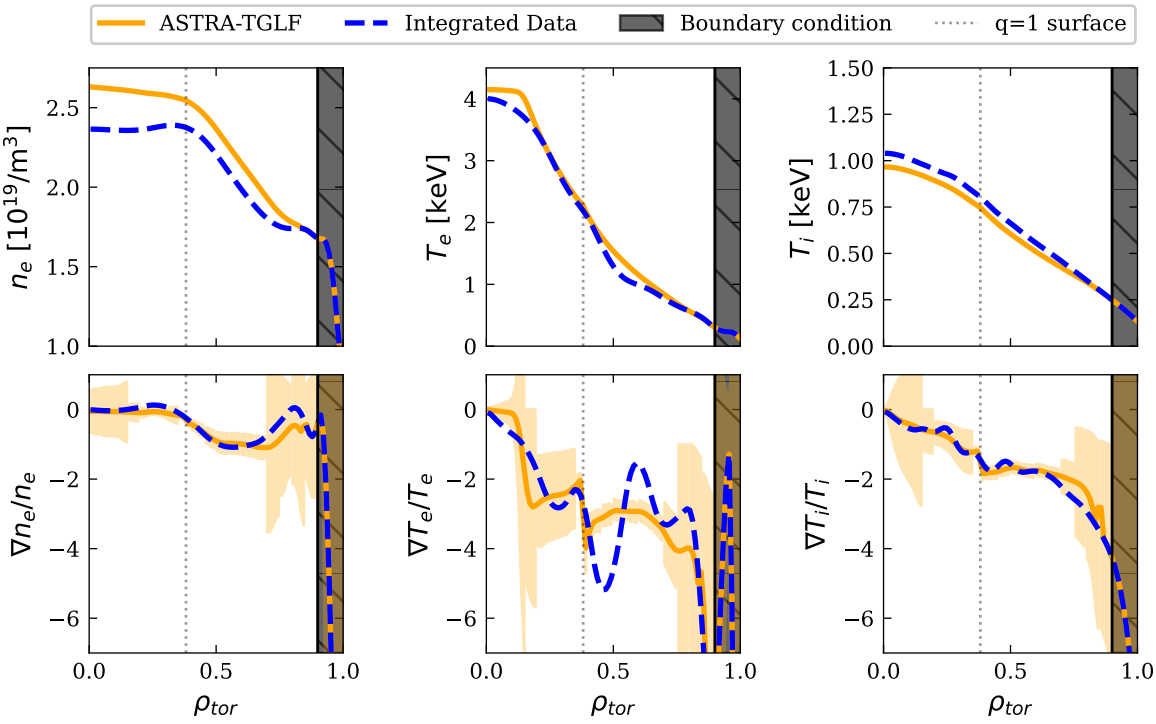

Figure 4.1.: ASTRA-TGLF simulation for the L-mode discharge #36974. The simulated profiles largely match the input profiles in blue. The first row shows the absolute values with the log gradients plotted below. The predetermined gradient uncertainties are shown in an orange shade. For the density and T_i, one can see that while the simulated gradient is slightly off close to the boundary condition, at mid-radius, the uncertainty seems reasonable. The electron temperature gradient has a stronger mismatch with the experiment. Thus, the simulation will have a larger impact on T_e when IDA is augmented with the kinetic model, see section 5.2.

The uncertainty was chosen to be large, close to the boundary condition (as the absolute values are largely determined by the experiment, and the gradients experience sudden jumps) and core (as our model has several limitations such as sawteeth and too low simulated turbulence from TGLF). For simplicity, the 50% uncertainty-region outer limit was kept at $\rho_{tor} = 0.35$ even if the q=1 surface moves outward. As the log gradient can be close to zero, a minimum uncertainty of $\sigma = 0.075$ for every value is assigned.

These uncertainties were found to work sufficiently well that they are used for the profiles in chapter 5. In the future, a more rigorous uncertainty model as a standard will be implemented with the ideas described and tested below.

4.2. Global sensitivity analysis

While the ASTRA-TGLF model is deterministic, the input parameters usually do have an uncertainty. This section aims to quantify the importance of the input parameters and to show how the output uncertainty is affected by the not well-known input. While there are

many methods devoted to this topic [132], this section will focus on a simple Monte Carlo method and Polynomial chaos expansion (PCE), which was worked on in cooperation with the Technical University of Munich and is still in active development.

4.2.1. Monte Carlo input uncertainty propagation

Monte Carlo simulations are a common approach to uncertainty quantification due to their versatility and quick implementation. A set of samples $\{\boldsymbol{\theta}^n\}_{n=1}^N$ is drawn from a distribution $p(\boldsymbol{\theta})$, with the guarantee that the function's expectation value $\langle f(\boldsymbol{\theta}\rangle$ matches that of the drawn samples $\langle \hat{f}(\boldsymbol{\theta}\rangle$ if enough samples are drawn independently of each other

$$\langle f(\boldsymbol{\theta}\rangle = \int d\boldsymbol{\theta} f(\boldsymbol{\theta}) p(\boldsymbol{\theta}) \approx \langle \hat{f}(\boldsymbol{\theta}\rangle = \frac{1}{N}\sum_{n=1}^{N} f(\boldsymbol{\theta}^n). \tag{4.2}$$

For more information, see [117].

Here, a Monte Carlo approach is used for a simple input uncertainty propagation scheme in which eight different input profiles were varied simultaneously for 80 ASTRA-TGLF runs. 80 samples are not as large a number as one would like in the context of Monte Carlo sampling. But it was chosen as a fast preliminary test of the method. Figure 4.3 shows simulations in which T_e, T_i, n_e, E_r, the safety factor q, Z_{eff}, P_{NBI} and P_{ECRH} were multiplied by a different random number. The number was taken from a normal distribution with mean $\mu = 1$ and standard deviation $\sigma = 0.15$. Similar simulations were also run varying Z_{eff}, the tungsten concentration and v_{tor}. This approach is similar to [87], where gradients were varied for single locations using VITALS [88].

Instead of using a grid search, the input was randomly varied. This method is known from hyper-parameter tuning [133] in machine learning and was chosen as some parameters are expected to have a bigger impact than others. Thus, a grid would waste simulations with varying parameters that might not be important. In figure 4.2, one can see an example of a two-dimensional sensitivity scan to which only one parameter meaningfully contributes. A quasi-random sampling method such as Sobol points [134] could be a further improvement over truly random samples because its more even distribution leads to better coverage.

The n_e, T_e and T_i profiles are expected to be stiff, due to the turbulent transport. These stiff gradients lead us to expect uncertainties of the simulated values at the boundary condition to propagate along the profile towards the core, i.e. the density is mostly sensitive to the density at the boundary condition. One can observe this in figure 4.3. The first row again shows the absolute values of inputs and simulated values. The shaded areas are a standard deviation of the samples, with the dotted line being the minimum and maximum sample. The profile stiffness can most effortlessly be seen in the minimum and maximum simulated density values originating from their input counterparts. The same is true for the electron and ion temperatures, although it is not as easily seen.

Overall, the observations from 4.1 continue. The electron density and temperature are well matched, although slightly overpredicted. Interestingly, the ion temperature is usually

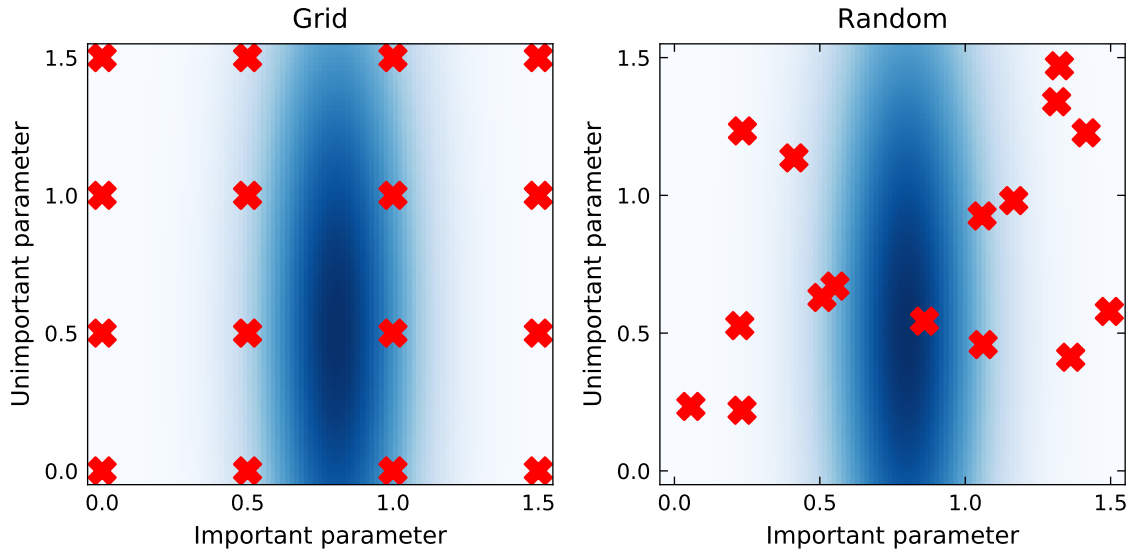

Figure 4.2.: Comparison of a grid and random Monte Carlo-like approach to sampling of a function. As the "Unimportant parameter" has only a small impact, one is effectively only receiving $\sqrt{n}$ new sampling info for n samples.

underpredicted, which might indicate the need to take the NBI blips as a heating source into account.

The log gradients are not as obviously connected to the inputs. Divided into the regions from above, in table 4.1, the highest log gradient standard deviations for the log gradients of two analyzed discharges are shown. The previously defined uncertainty for the T_e log gradient is close to that found by error propagation. However, the density standard deviation can deviate substantially. This is partly due to $\nabla n_e/n_e$ being closer to zero for most of the minor radius and is caught by the $\sigma_{min} = 0.075$ condition above. If assigning uncertainties for regions remains the predominant method for IDA-KM, it may be necessary to make the density margin of error larger.

Overall, the sensitivity analysis done for a few discharges shows that comparing log gradients of the profiles makes sense and that our assumed uncertainty is not completely unreasonable. However, it also has drawbacks. The log gradient for T_e is too small in the vicinity of the sawtooth region, where it changes suddenly. This should remind the user that this kind of analysis can not detect model deficiencies. In [84] the TGLF SAT-2 was found to compute energy fluxes with an error of about 16% and particle fluxes of about 33% compared to CGYRO. These uncertainties can just be added to the input uncertainty propagation scheme variables.

ρ_{tor}	Assumed σ	n_e L-mode	T_e L-mode	n_e H-mode	T_e H-mode
0.15	400	19	15	20	18
0.20	100	591	5	17	19
0.35	50	300	4	15	10
0.80	10	23	12	127	10
0.85	25	16	17	93	16
0.90	75	19	22	58	25
1.00	125	-	-	-	-

Table 4.1.: Comparison of the assumed uncertainty for IDA+KM to the standard deviation found for the L-mode #36974 and H-mode #33616 discharges for different plasma radii. The region of smallest uncertainty $0.35 \leq \rho_{tor} \leq 0.8$ also has the best matching heat flux in figure 5.2

4.2.2. Polynomial chaos expansion

Section 4.2.1 introduced estimating the sensitivity of the ASTRA-TGLF via input uncertainty propagation. The method had the advantage of being simple to implement and being easily run in parallel. However, Monte Carlo methods have a root-mean-square error (RMSE) of $\sigma/\sqrt{N}$, where N is the number of samples. Thus, a large number of samples is required to achieve a given level of accuracy, which is impossible for many kinetic models due to the excessive computational requirements. There are many alternative approaches available to solve this issue[135]. In cooperation with the Technical University of Munich, PCE has been implemented as one of the methods to efficiently perform Forward Uncertainty Quantification. The following section is quite technical, but the overarching goal is to decompose the behavior of the model into orthonormal polynomials, perhaps similarly to how a Fourier transform decomposes a function into orthogonal sinusoidal components.

Again consider a function $f(t,\theta)$, where $t \in \mathbb{R}^{d_t}$ are the deterministic parameters and $\theta \in \mathbb{R}^{d_\theta}$ represent the stochastic parameters. The distribution of the stochastic parameters is known ($\theta \in \rho(\theta)$). Let θ_i represent the i^{th} stochastic dimension.
The first step of building PCE is to decide upon the choice of a polynomial. The polynomial represents the i^{th} stochastic dimension ($\phi_n(\theta_i)$) and is chosen based on the orthonormality with respect to the distribution. The inner product of two polynomials of different orders should equal 0 when the orders are different and equal to 1 when the orders are the same. Mathematically, it can be formulated as

$$< \phi_n(\theta_i), \phi_m(\theta_i) >_\rho = \int \phi_n(\theta_i)\, \phi_m(\theta_i)\, \rho(\theta_i)\, d\theta_i = \gamma_n\, \delta_{nm}$$

- Kronecker delta $\delta_{nm} = \begin{cases} 1, & \text{if } n = m, \\ 0, & \text{if } n \neq m. \end{cases}$
- normalization constants $\gamma_n =< \phi_n(\theta_i), \phi_m(\theta_i) >_\rho$

For this PCE analysis, a uniform distribution was chosen ($\mathcal{U}[-1,1]$). Thus Legendre polynomials were used. Legendre polynomials are formulated as:

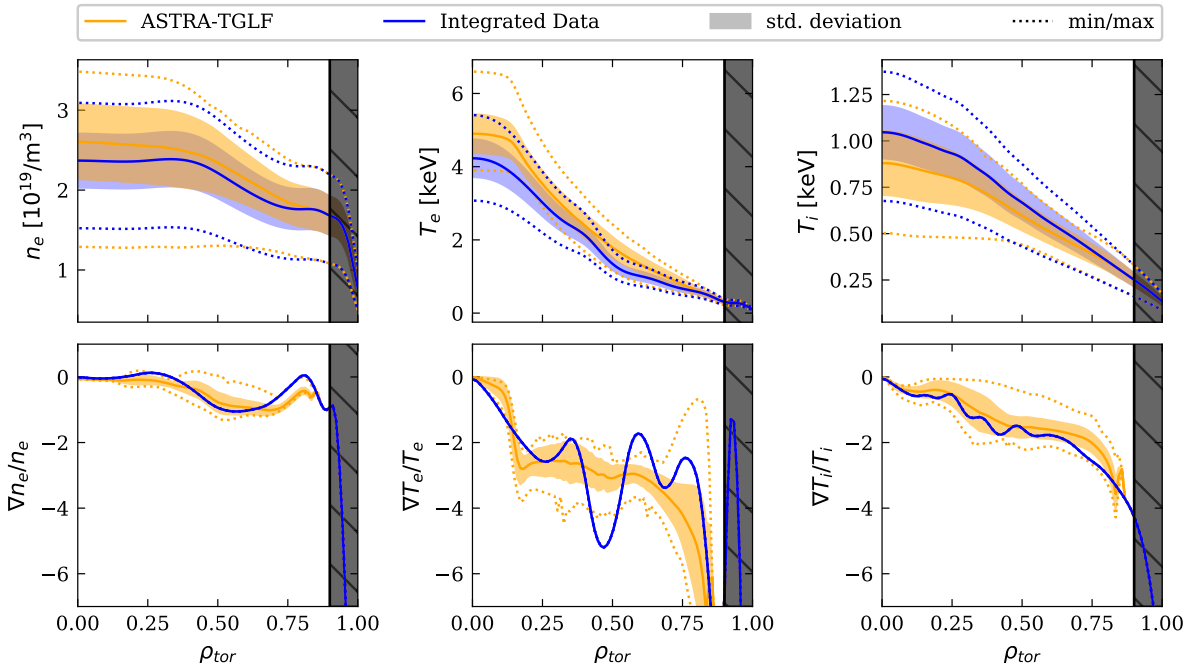

Figure 4.3.: Input uncertainty propagation for the L-mode discharge #36974. 8 different parameters (T_e, T_i, n_e, E_r, the safety factor q, Z_{eff}, P_{NBI} and P_{ECRH}) were varied for 64 simulations. 16 more simulations were started but terminated early due to problems achieving an equilibrium. The input uncertainty propagation shows that the density and temperatures are mainly sensitive to their input counterpart. The log gradient of the profiles is less obviously connected to the input.

- $\phi_0 = 1$
- $\phi_1 = \omega$
- $\phi_2 = \frac{1}{2}\left(3\omega^2 - 1\right)$
- $\phi_3 = \frac{1}{2}\left(5\omega^3 - 3\omega\right)$
- $\phi_4 = \frac{1}{8}\left(35\omega^4 - 30\omega^2 + 3\right)$
- ...

with $\gamma_n = \frac{1}{2n+1}$.

If the distribution is normal ($\mathcal{N}(0,1)$), then one can use Hermite polynomials such as were used for the basis functions of TGLF in section 2.4.3. Hermite polynomials are formulated as:

- $\phi_0 = 1$
- $\phi_1 = \theta$
- $\phi_2 = \theta^2 - 1$

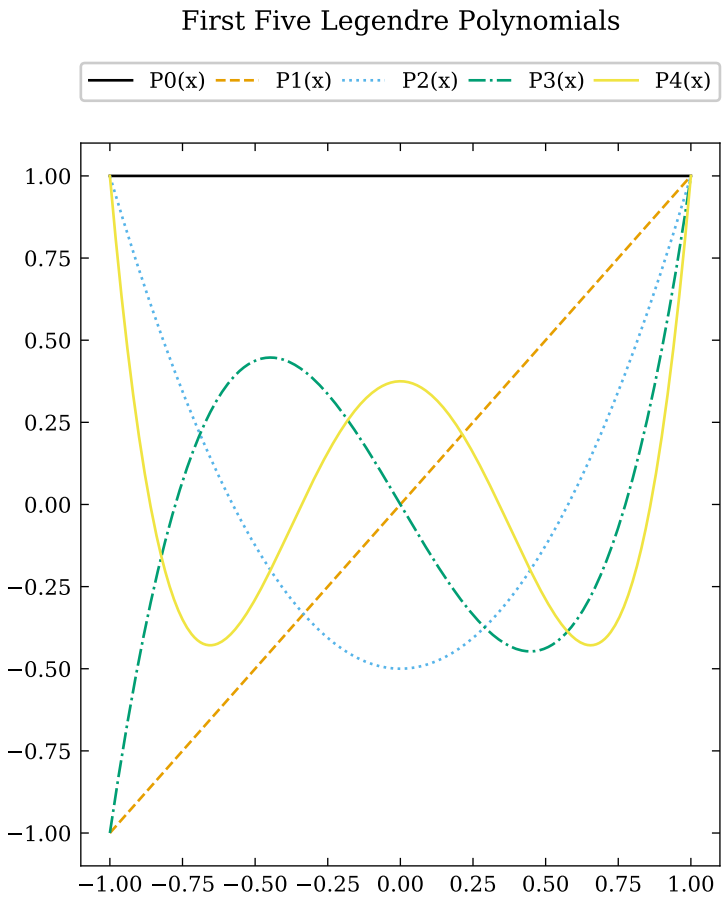

Figure 4.4.: First 5 Legendre polynomials used to approximate a uniform distribution.

- $\phi_3 = \theta^3 - 3\theta$
- $\phi_4 = \theta^4 - 6\theta^2 + 3$
- ...

with $\gamma_n = n!$.

The multi-dimensional polynomials are defined by taking the product of polynomials of each dimension. Using multi-index (a set of integers) $n = \{n_1, n_2, ..., n_{d_\theta}\}$ where n_i represents order of the i^{th} stochastic parameter, the corresponding polynomial is written as:

$$\Phi_n(\theta) = \phi_{n_1}(\theta_1)\phi_{n_2}(\theta_2)...\phi_{n_{d_\theta}}(\theta_{d_\theta})$$

Now, one can write write down the PCE as follows:

$$f(t,\theta) = \sum_{n \in \mathcal{A}} \hat{f}_n(t)\Phi_n(\theta) \tag{4.3}$$

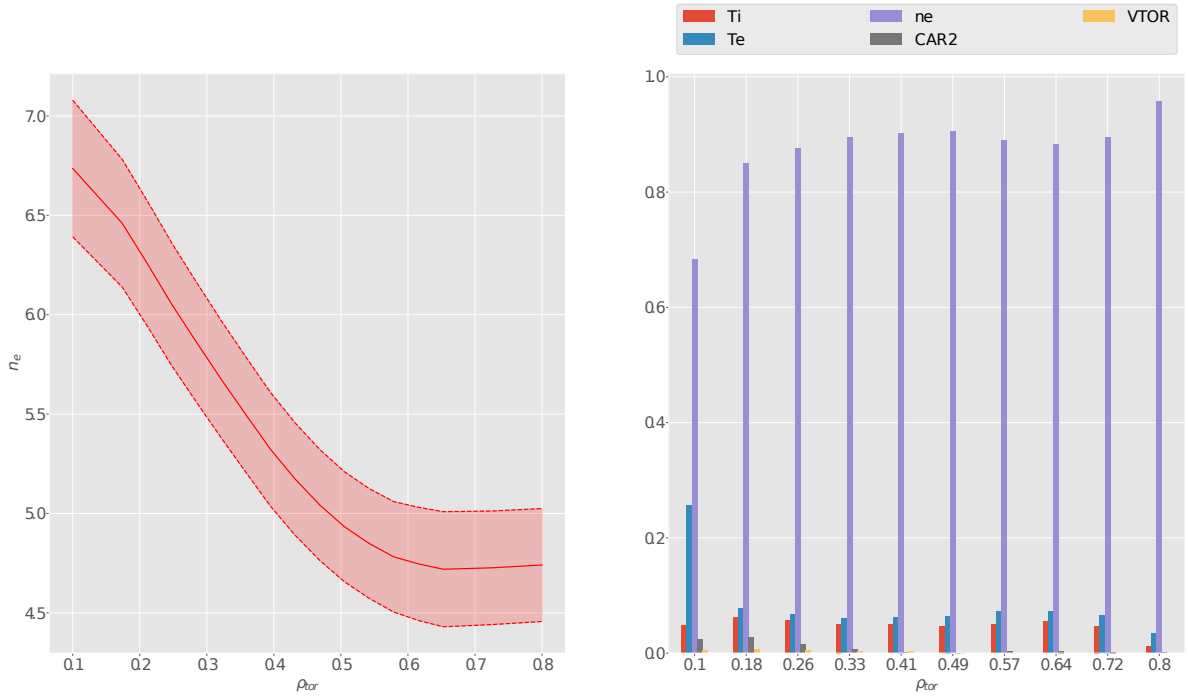

Figure 4.5.: Example of a polynomial chaos expansion exploring the density sensitivity on five inputs. Compared to the input propagation from 4.2.1, the user gets the benefit of the Sobol indices, which illustrate the relative importance of the input. For this simple case, the density is unsurprisingly most important. More recent results hint at a $\frac{T_e}{T_i}$ dependence for the simulated gradients. $CAR2$ represents the safety factor q in these simulations.

where $\mathcal{A}$ is a set of active multi-indices and $\hat{f}_n(t)$ is the coefficient of the polynomials. $\mathcal{A}$ is chosen according to the $f(t,\theta)$ and computational budget. The coefficients can be calculated by taking the projection of the function $f(t,\theta)$ on the polynomial. This method is known as the Pseudo-spectral approach [136]. This method suffers from the curse of dimensionality, meaning that as the number of dimensions increases, the computational resources required to process and analyze the data also increase significantly. Algorithms that are efficient in low-dimensional spaces might become computationally infeasible or slow in high-dimensional spaces. This problem can be solved by using a sparse grid [137, 138]. Another popular method is Stochastic Collocation [136].

One can calculate the statistical moments directly from these coefficients.

$$\mathbb{E}[f(t,\theta)] = \hat{f}_{\emptyset} \tag{4.4}$$

$$Var[f(t,\theta)] = \sum_{n \in \mathcal{A}} \hat{f}_n^2(t) - \hat{f}_{\emptyset}^2 \tag{4.5}$$

where $\emptyset$ represents a multi-index of zeros.

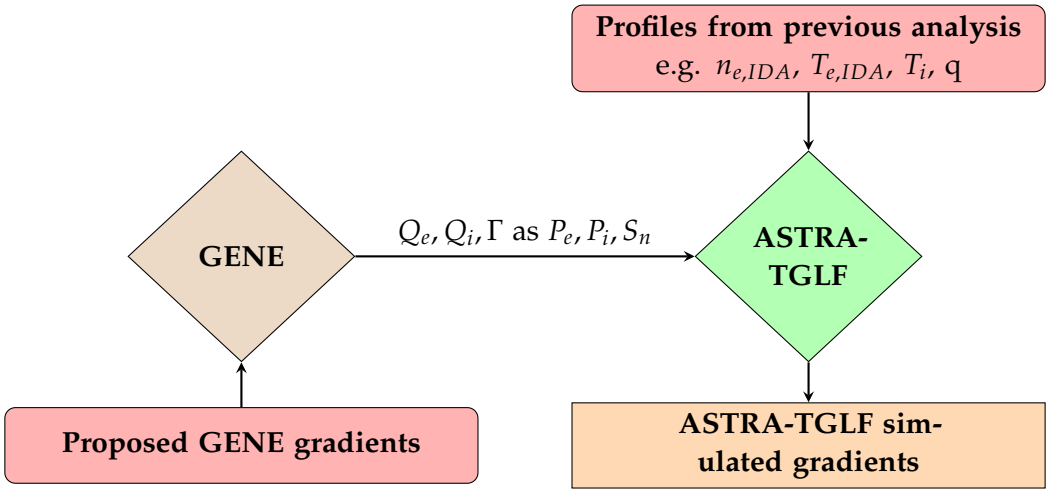

Figure 4.6.: Sketch of the workflow to compare the gradients of GENE and ASTRA-TGLF. GENE was given gradients chosen by the user whose fluxes were given as input to ASTRA-TGLF.

An advantage over standard Monte Carlo methods is that the user receives information on the relative importance of each input parameter, as the method calculates the variance-based Global Sobol sensitivity index [139] directly from PCE.

The sensitivity index of θ_i is calculated as:

$$S_i(t) = \frac{D_i(t)}{\mathrm{Var}[f(t,\boldsymbol{\theta})]}, \quad D_i(t) = \sum_{\boldsymbol{n}\in A_i} \hat{f}^2_{\boldsymbol{n}}(t) \tag{4.6}$$

The first sensitivity index represents the change in the input when only the ith input variable is varied:

$$A_i = \{\boldsymbol{n} \in \mathbb{N}_0^d : \forall j \neq i, \boldsymbol{n}_j = 0, \boldsymbol{n}_i \neq 0\}$$

The total sensitivity index takes both direct effects as well as any interaction effects with other input variables into account.

$$A_i = \{\boldsymbol{n} \in \mathbb{N}_0^d : \boldsymbol{n}_i > 0\}$$

4.3. Errors ingrained in the ASTRA-TGLF model

In the previous section, the thesis explored the uncertainty of the model based on an uncertain input. In this section, some further possible limitations of the ASTRA-TGLF model are presented, which have a direct impact on the simulated gradients.

4.3.1. GENE gradient comparison

On top of the sensitivity analysis above, work was done to ascertain the presence of a systematic prediction error for the simulated gradients. This error could arise from an offset of the critical gradients or by varying stiffness levels. While measuring a profile's exact gradient

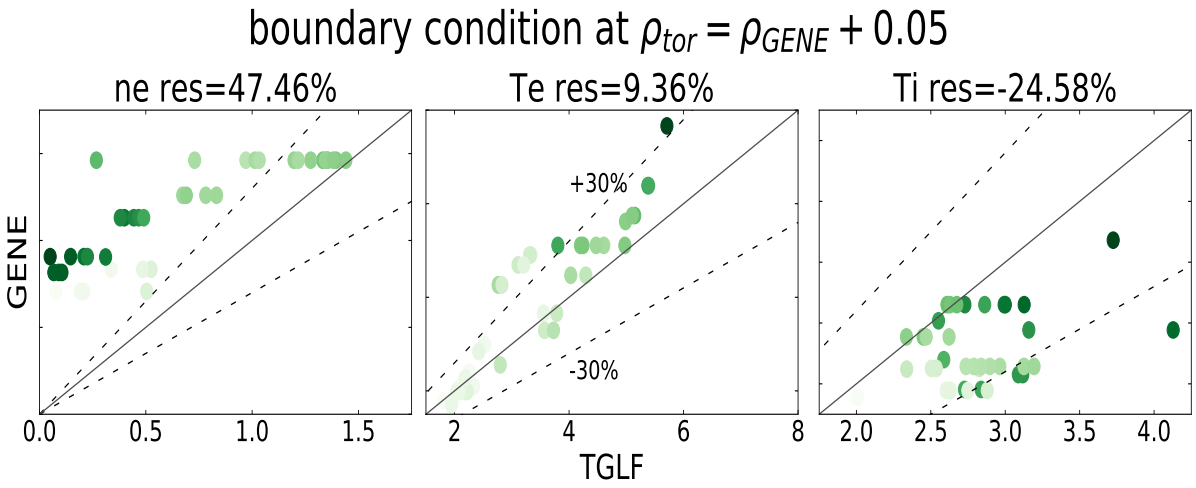

Figure 4.7.: Comparison of log gradients of ASTRA-TGLF L-mode simulations compared to GENE. The points are shaded with the size of the gyroBohm flux. The residual is given in a relative deviation of the gradients. While $\nabla ln(T_e)$ matches quite well, the density gradient is systematically under-predicted while $\nabla ln(T_i)$ is over-predicted. In general, it seems that the fit between the two decreases with the magnitude of gyro-Bohmflux. Points on the black diagonal line mean a perfect match of the gradients with the dashed lines being $\pm 30\%$.

is nearly impossible, one can assume that the high-fidelity transport codes contain enough physics to be close to the actual true value. It was decided to compare GENE instead of CGYRO with TGLF, as there were simulated discharges and more expertise readily available. GENE is one of the highest-fidelity codes available, and it is our best representation of the actual gradients in an experiment, see section 2.4.2. Due to a recent problem with a gradient jump at the boundary condition, the results shown in this subsection are based on ASTRA7-TGLF-SAT1 results.

For this work, non-linear electromagnetic GENE simulations of 3 L-mode deuterium discharges and 1 L-mode Hydrogen discharge at different radii (ρ_{tor}=[0.563, 0.615, 0.75]) were studied [140, 87]. The simulations were done for code validation, with the heat flux being one of the many aspects of GENE being validated. As the studies did not find well-matching heat fluxes just using the experimental profiles, several additional GENE runs had to be produced. At the simulated radius, the gradients of the input profile were varied until the GENE fluxes matched the heating input calculated by TRANSP [141] (a comparable code to ASTRA). Overall, more than 40 GENE simulations with different gradients and, thus different fluxes were added to the database.

For this work, the particle and heat sources of the ASTRA-TGLF model were scaled to match the GENE fluxes for the simulated GENE radius (see the flowchart in figure 4.6). This way, possible sources of discrepancies between ASTRA and TRANSP, such as $P_{e,i}$, are excluded. The boundary condition of ASTRA-TGLF was chosen to be the radius of the GENE

simulation + 0.05 ρ_{tor}. After the ASTRA-TGLF simulation has reached convergence, one can compare the gradients with those used as input to GENE.

In figure 4.7, one can see the resulting log-gradients of the ASTRA-simulation compared to inputs of GENE with each point being colored by the flux in gyro-Bohm units (particle flux $\Gamma_{GB} \propto nT^{1.5}$ and heat flux $Q_{GB} \propto nT^{2.5}$), which illustrates how "turbulent" the plasma is. The average deviation $res = \frac{\nabla ln(GENE) - \nabla ln(TGLF)}{\nabla ln(GENE)}$ from the GENE log-gradients is given as the residual above. The density gradients are systematically under-predicted, with the error worsening the more turbulent the simulation is. While TGLF's predicted T_e gradient is quite close to GENE, the ion gradient is over-predicted for most cases, and again the match gets worse with rising gyro-Bohm flux.

Of course, this is just a rough estimate as the boundary condition is not exactly at the radius of the GENE simulation, meaning that important values such as $\frac{T_e}{T_i}$ and the collisionality are close but not exactly the same. It was observed that if the boundary condition is moved further away from the radius of interest, the T_i gradient match is improved, underscoring its importance on the gradients.

Moving the boundary condition further back also gives $\frac{T_e}{T_i}$ more flexibility. In figure 4.8, one can see the results for ASTRA-TGLF simulation with a boundary condition at $\rho_{tor} = 0.9$. The x-axis shows the change in $\frac{T_e}{T_i}$ of the ASTRA-TGLF simulation. One can see that the error in for the density and T_i gradients clearly decrease with rising fraction. An important caveat with regard to this finding is that in a substantial amount of the GENE simulations, the used T_i gradient was too large, leading to an overly large ion heat flux. The simulated ion temperature was often too high as the simulated GENE ion heat flux was also larger than the TRANSP power balance in many cases. This results in a too-large ion heating in ASTRA-TGLF. One should also mention that some of these GENE simulations were made at radii where the ECE had a measurement gap, and the T_i was measured via NBI blips, adding further uncertainty for both temperatures.

The results are an interesting starting point in quantifying systematic errors of TGLF. The mismatch compared to GENE has many possible explanations due to the flawed methodology. The VITALS [88] framework has been implemented, which will make a more systematic approach possible, allowing for scans and free variation of specific parameters in TGLF.

4.3.2. Uncertainty due to differences in equilibrium

Just as IDA uses an equilibrium to map the diagnostics to ρ_{pol}, ASTRA-TGLF uses SPIDER to create its 2D equilibrium needed by the various subroutines. For most of the discharges analyzed in the thesis, the flux surfaces of the two codes matched well.
For the discharge #30506, the heating profiles were calculated by TRANSP because the discharge used ICRH heating, which is not yet implemented in ASTRA. While the q-profile matched that of the CLISTE equilibrium, the flux surfaces calculated by SPIDER were shifted as shown in figure 4.9. The mismatch is most likely due to the ICRH-born fast-ion pressure not being included in CLISTE (or IDE).
The equilibrium matches when simulating discharges with fast ions purely from NBI heating.

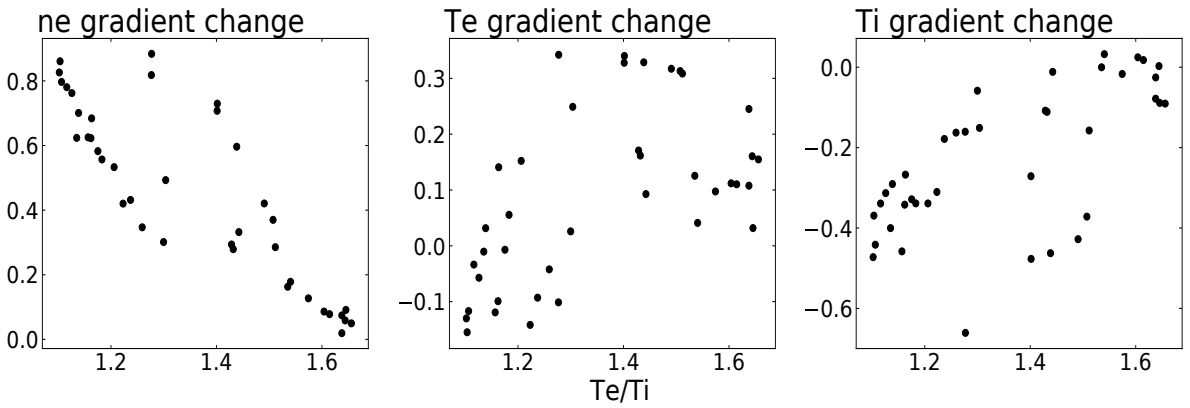

Figure 4.8.: Gradient error between TGLF and GENE compared to $\frac{T_e}{T_i}$ of the ASTRA-TGLF simulation. Compared to figure 4.7 the boundary condition was moved back to $\rho_{tor} = 0.9$. The mismatch in n_e and T_i gradient was found to decrease with rising temperature fraction. This strong dependency motivates further analysis with codes such as VITALS.

However, in discharges with internal transport barriers such as the #39230 discussed in section 5.4, the equilibrium match becomes problematic. The ASTRA-TGLF simulation of figure 5.9 nicely matched the experimental equilibrium but did not capture the ITB. Consequently, the simulated thermal pressure is too low. When running ASTRA in interpretative mode, fixing ASTRA's kinetic profiles to the experimental ones, the thermal pressure is higher than in the ASTRA-TGLF case, as the ITB raises the profiles. The SPIDER equilibrium, in this case, has an overly strong Shafranov-shift when fast ions are considered and slightly too small when the fast ion pressure is set to zero, see figure A.1.

A similar mismatch between the flux surface reconstruction was found between TRANSP and ASTRA depending on the equilibrium provided to those codes in [142]. In their work, these codes are employed to model the rotation velocities of NBI modulation experiments in ASTRA7. This is documented in more detail in [143]. In their analysis, they opted to map the diagnostics taken in real-space coordinates onto a CLISTE equilibrium due to the better flux surface and volume element match with SPIDER.

In contrast to this thesis, [142] let the current evolve so that the ρ_{tor} to ρ_{pol} mapping is not the same as that of the input equilibrium. Repeating the discharge simulation with the ASTRA8-TGLF model, we still find SPIDER to match EQH's flux surfaces better. However, the match to IDE is good enough for our analysis.

Overall, the equilibrium uncertainty does not seem to be negatively impacting IDA+KM. Keeping the current and thus q-profile fixed leads to a constant mapping between ρ_{tor} and ρ_{pol}. It is thus believed that the error of the log gradient stemming from switching between IDE and SPIDER should be small. The mismatch of the flux surfaces is also usually not big enough to warrant concern that the heat and particle flux is being wrongly calculated. Based on a limited sample size of ASTRA8 and ASTRA7 simulations, the equilibrium must be double-checked when simulating discharges with internal transport barriers or a large fraction of fast ions.

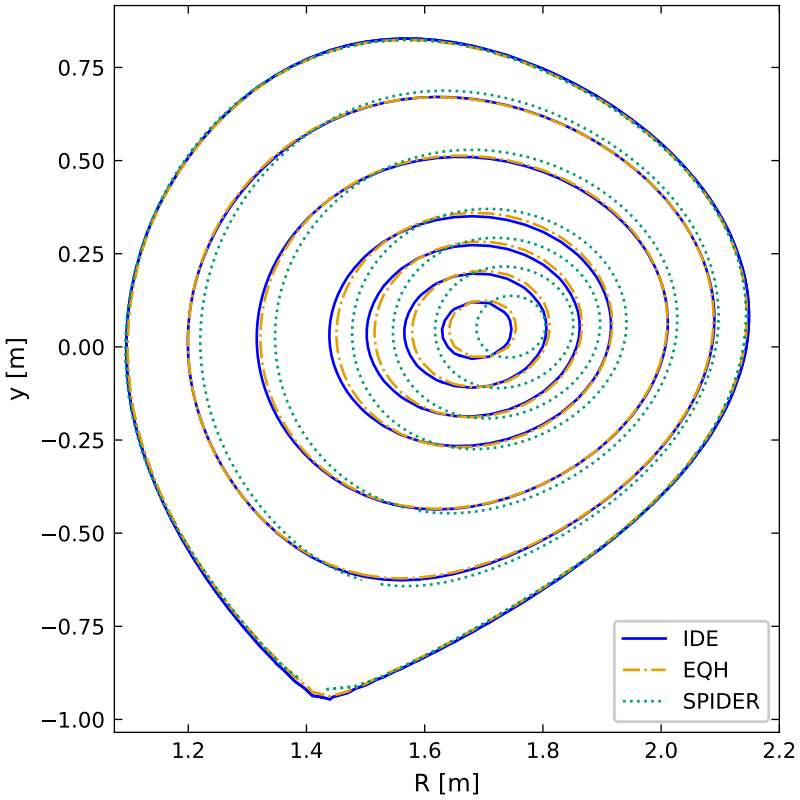

Figure 4.9.: Equilibria for #30506 at 5.2s using the IDE, CLISTE and SPIDER solvers. The discharge has a high ICRH fraction, which could explain the strong Shafranov shift, as only fast ions stemming from NBI heating were included in IDE in this case.

SPIDER is expected to slowly be replaced by the **F**ast **Equi**librium **S**olver (FEQIS) [144], which was first developed as an equilibrium code for the ASDEX Upgrade flight simulator Fenix. If FEQIS also becomes the norm for IDA+KM, the same checking of equilibria will need to be done.

4.3.3. Uncertainty due to numerical diffusivities and smoothing

As for most tokamak simulations, the transport is stiff; changing a gradient for the turbulence solver can mean a large change in the flux. This strong dependence of the diffusion coefficients on the gradients leads to numerical problems that cause unphysical oscillations in the profiles. To tackle this problem, [145] introduced effective numerical diffusivities into ASTRA, which make it possible to run with larger timesteps and thus speed up convergence by a factor of 100. The implementation in ASTRA is further derived in [146]. These numerical diffusivities should be chosen with some care if one is simulating certain transient events, as increasing them can lead to faster convergence in ASTRA, but also to loss of physical effects when the profile rapidly evolves. For the ASTRA-TGLF model, the simulation was run with a fairly standard $50 m^2/s$ for each species, letting the user terminate the simulation after 80 steps,

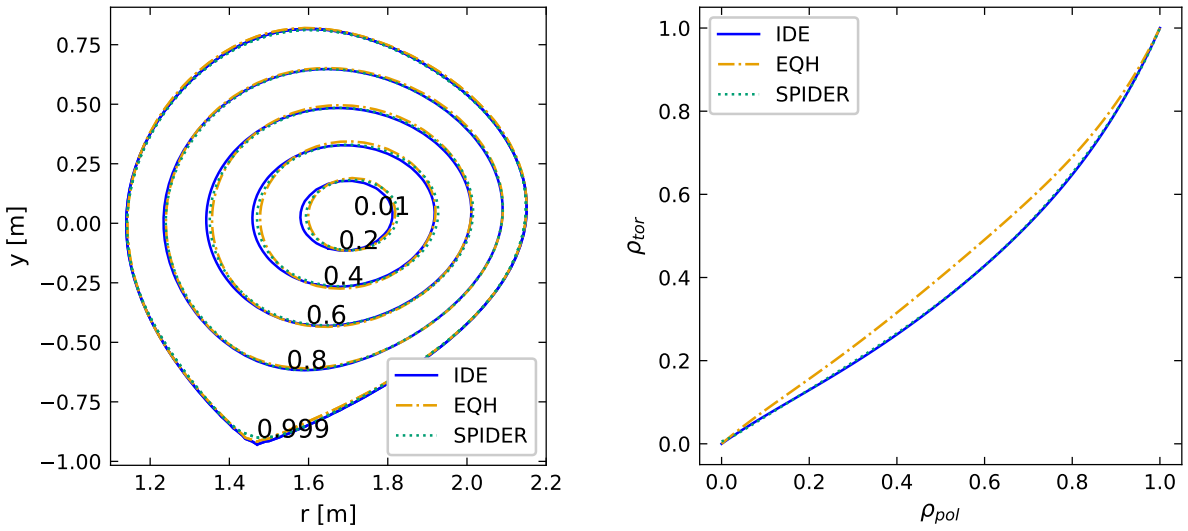

(a) Equilibria for #41550 at 1.9s using the IDE, CLISTE and SPIDER solvers. Flux surfaces were given in ρ_{tor}. The SPIDER equilibrium was made using input from IDE, but for $\rho_{tor} = [0.2 - 0.4]$, the flux surfaces appear closer to the EQH.

(b) The mapping of ρ_{pol} to ρ_{tor} for SPIDER is almost perfectly matching IDE. This is vital for IDA+KM, as IDA is run using ρ_{pol} and ASTRA in ρ_{tor} and the gradients need to match.

Figure 4.10.: H-mode discharge #41550 used modulating NBI power to examine rotation behavior. The simulation in [142] had problems with mismatching flux surfaces, making tracking the diagnostics difficult. Using ASTRA8 some mismatch was also observed but, more important for this thesis, the mapping between ρ_{tor} and ρ_{pol} stayed constant.

with the profile only changing slightly.

To determine how much the simulation is off by, the residuals between the actual flux and flux, including the numerical diffusivity, were examined. Figure 4.11 shows the residuals for the H-mode discharge #33616. As expected, the difference falls off quickly during the first couple of timesteps and then reaches an oscillation stage after 50 steps. The particle flux is slower to converge, with the main problem being the areas of low flux $\rho_{tor} \leq 0.4$. In the low particle flux regions, a small change of gradient can change the transport from diffusive to inward convection.

The different fluxes are shown in figure 4.12. One can see that the differences between the fluxes with and without the numerical diffusivity are quite localized. The electron and ion heat fluxes have some problems close to the ECRH injection area, with the difference diminishing quickly. The difference in the particle flux converges slower, with the actual flux having a convective pinch even after 12s. As shown in the plots, simulations running for more than four times the usual length still had the difference between the two fluxes slightly decreasing, with the actual density and temperature profiles barely changing. Thus it was decided to stick to a 4s (80 steps) simulation as a practical compromise.

The numerical diffusivity has almost no impact on the final converged profile but needs to be considered when comparing fluxes to determine the impact of IDA+KM. Figure 5.8 shows

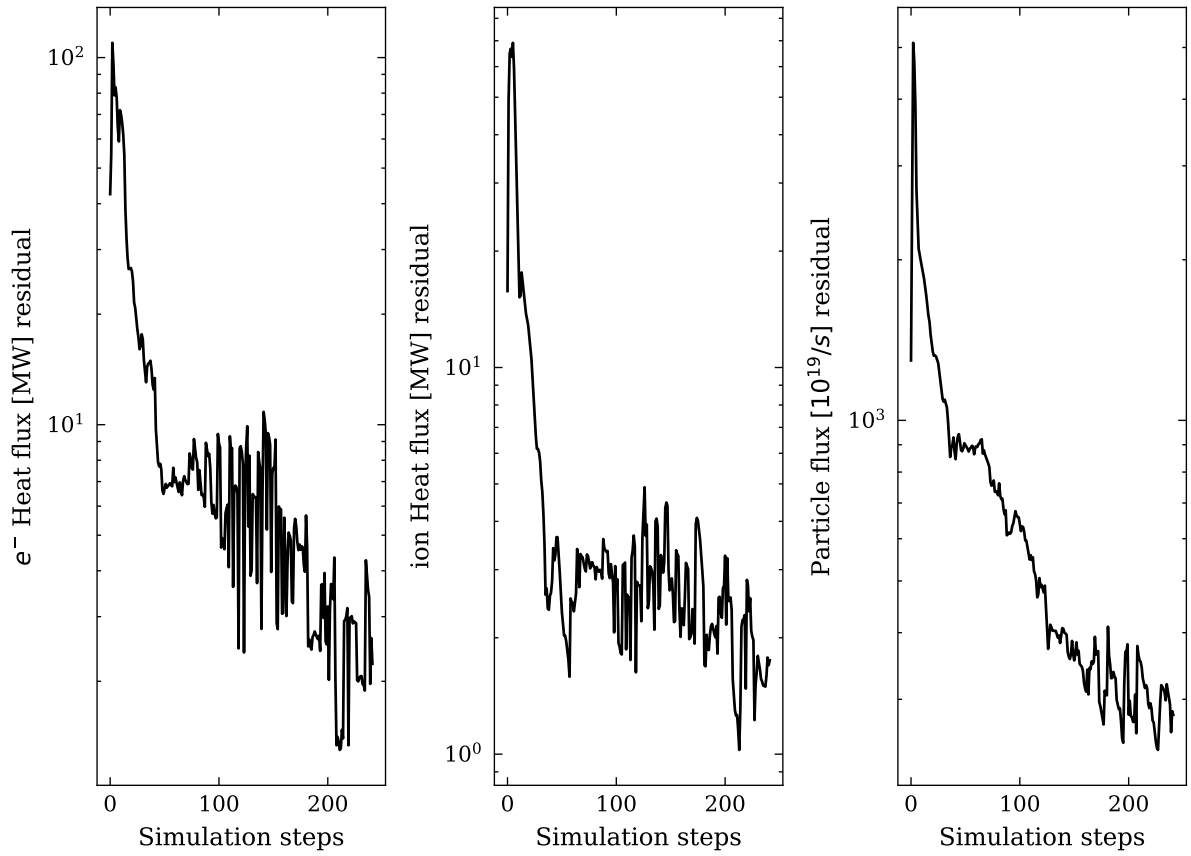

Figure 4.11.: Residuals between the particle and heat fluxes, including and excluding the numerical diffusivity. The slow drop-off for the particle flux is explained by a small gradient change having an outsized impact on the flux itself.

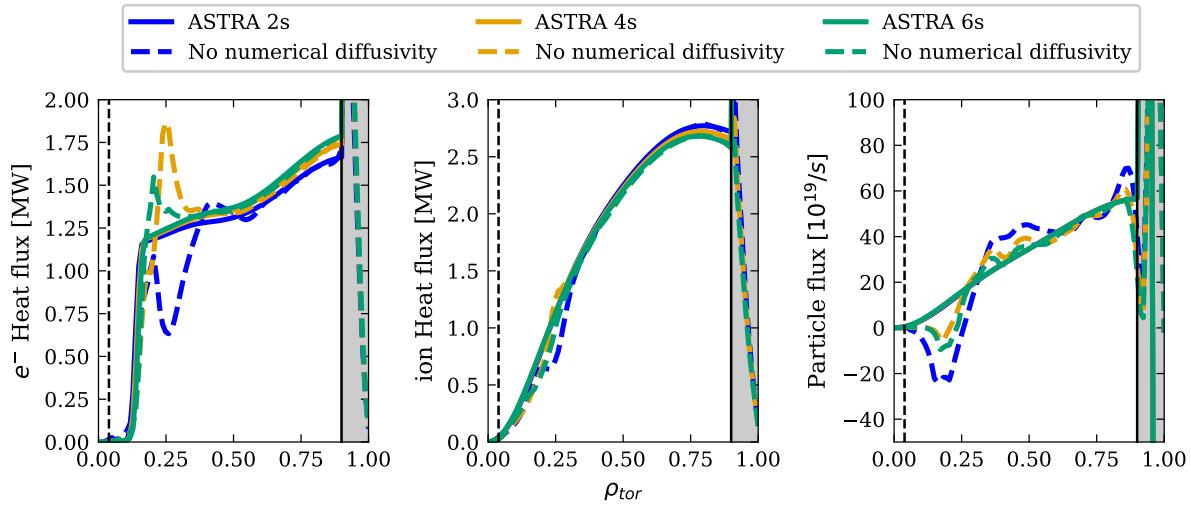

Figure 4.12.: Flux comparison between the flux given by ASTRA and calculated flux without the numerical diffusivity. For figures such as 5.2, the dotted line is calculated as the profiles are kept constant.

the fluxes of the IDA and IDA+KM #33616 discharge. For the particle flux, it looks as if the particle flux is not matching the theory. Comparing the fluxes to figure 4.12, one can see that the mismatch is due to the numerical diffusivities and that the profile gradients match the simulations well. When running ASTRA in interpretive mode and thus keeping the profiles constant, the artificial diffusivity plays no role, so differences between the actual transport are apparent. This needs to be considered when comparing the heat and particle fluxes of IDA and IDA with the kinetic modeling prior in the next chapter, as one fits the profiles to a simulation with a not quite converged profile. In figure 5.8, the particle flux matches the simulation well, even if it does not match the particle balance.

TGLF is run at every radius location. However, to obtain manageable profiles, a smearing function is used that balances smoothing with the profile changing too strongly via the parameter α:

$$\min \int_0^{\rho_B} \left[\alpha \left(\frac{\partial R_{\text{out}}}{\partial \rho} \right)^2 + \left(R_{\text{in}}(\rho) - R_{\text{out}}(\rho) \right)^2 \right] d\rho \tag{4.7}$$

Ideally, one would add more points to our profile to limit the impact of the smearing function. However, the results of a small study in reducing the radial distance and smearing factor found a negligible impact on the simulated profile. Thus the kinetic model uses the standard values given in the GitLab ASTRA-equ files. As was the case with the numerical diffusivity, it will be necessary to reduce smoothing if one wants to model sudden and localized phenomena e.g. pellet injection.

This chapter has shown that the sensitivity of the kinetic model can be calculated by forward UQ algorithms. The sensitivity determined by the Monte Carlo method is in line

with the predetermined uncertainty that the thesis will use in the next chapter. Several potential sources of systematic uncertainty were analyzed and found to have only a minor effect on the simulation. The exception is the comparison of gradients between TGLF and GENE where the large mismatch in the density is potentially troubling. However, these results need to be further verified with more exact tools such as the VITALS framework.

In future work, metrics should also be adapted to reject an inaccurate simulation and change a parameter, such as adding impurities or changing the boundary condition. For now, the users must evaluate the simulation and decide if the kinetic model captured the physics enough to move forward with the implementation in IDA. This decreases the time efficiency of IDA+KM as more human effort is required.

5. Kinetic modeling prior's effect on profiles

After discussing the basis of the kinetic model ASTRA-TGLF and the uncertainties and errors associated with the model, this chapter will show the implementation of the simulation in the IDA framework, followed by presenting the results of it being added to different discharge scenarios.

5.1. IDA+KM workflow

When the prior from the kinetic model is desired, an ASTRA simulation (described in 2.4.1) is started before the IDA fitting process. The user has the ability to choose between a multitude of quasi-linear turbulence models, with the default being TGLF SAT-2. After the simulation is converged, the user has the option to review the simulation results. If the simulated temperatures and densities fail to match the input, it is a strong indicator that the simulation needs to be studied in more detail. For example, the radiated power depends on the tungsten concentration, which can have large uncertainties.

The simulated profiles or their log gradients are compared against the proposed IDA profile using a Gaussian or Student's t-distribution and treated just as any other diagnostic in the framework. Comparing the log gradients and using a Gaussian distribution, the kinetic model prior's likelihood would be:

$$p(KM|n_e, T_e) = \sum \left[\left(\frac{\nabla ln(T_{e,KM}) - \nabla ln(T_e)}{\sigma_{KM}} \right)^2 + \left(\frac{\nabla ln(n_{e,KM}) - \nabla ln(n_e)}{\sigma_{KM}} \right)^2 \right] \tag{5.1}$$

Ideally, one would like to run ASTRA-TGLF multiple times with the profile that is currently being optimized as input. Although the option exists to use the currently proposed density and temperature profile as ASTRA-TGLF input, it was observed that simulation results improve if the input is not coming from the very early optimization steps. Because ASTRA-TGLF (and thus IDA+KM) results only change slightly during the final optimization phase, a standard IDA profile was used as input. The slight change is explainable by the use of a boundary condition and the large uncertainties used at the edge, which lead to the kinetic model not strongly impacting the profiles at the pedestal. Consequently, using a standard IDA profile as the ASTRA-TGLF input does not lead to significant differences in the simulated log gradient and saves computational time. The new workflow with the kinetic model used in this thesis is sketched in figure 5.1.

While their shotfiles are called IDI and IDE, ion temperature and safety factor profiles also come from integrated data analysis frameworks, but the actual electron density and

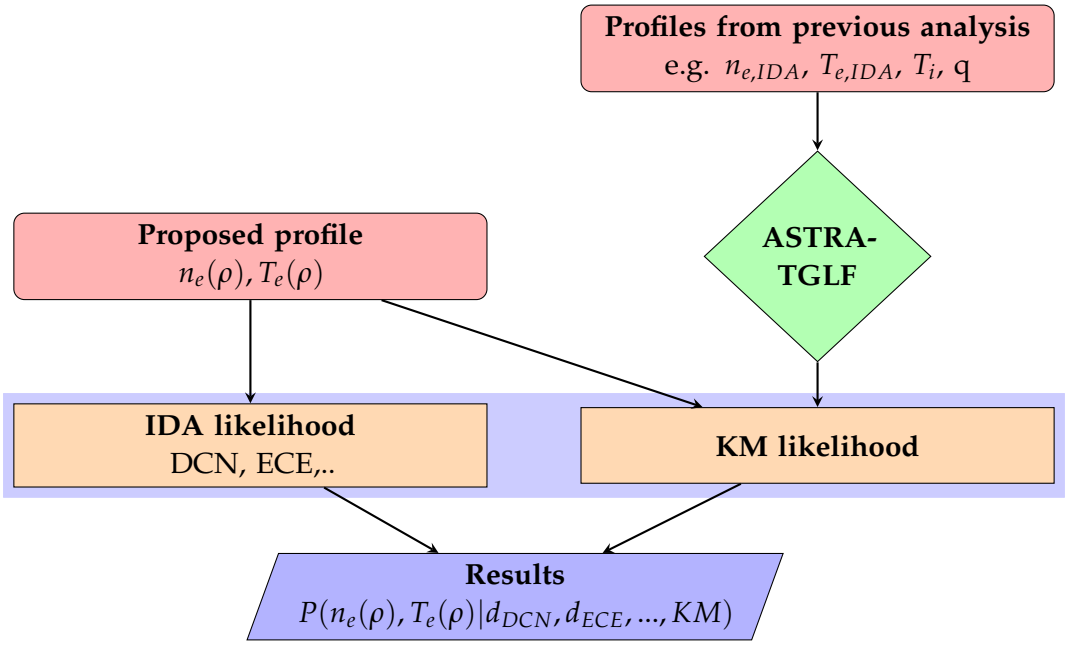

Figure 5.1.: Sketch of the IDA+KM workflow in reference to the flowchart 3.5. The discharge is simulated at the beginning of the IDA fitting process, with the kinetic modeling likelihood being updated in each IDA step as if it was any other diagnostic. For this thesis, the curvature prior was turned off in the IDA+KM profiles.

temperature shotfiles are called *IDA*. To avoid confusion, when simulations are shown, the experimental data will be called *Integrated Data*, while IDA is used when only showing electron profiles or fluxes in which two electron profiles are being compared.

5.2. L-mode discharges

Shot	P_{NBI} [MW]	P_{ECRH} [MW]	Description
GENE isotope validation study [87, 77]			
33585	0	0.7	deuterium
36974	0	0.7	deuterium
36770	0	0.7	hydrogen
GENE gradient validation study with upper single null [140]			
38419	0.8	1.2	flat, steep
38420	0.8	1.0	steep
38421	0.8	1.0	steep
38422	0.8	1.0	flat
38423	0.8	1.0	flat
38424	0.8	1.5	flat, steep
38425	0.8	2.0	flat, steep
38426	0.8	2.3	flat, steep
Heating mix confinement study [53]			
35475	1.6	0.0	
35475	0.8	0.7	
35475	0.0	1.4	
Grillix neutrals discharge [147]			
36190	0.5	0	

Table 5.1.: L-mode discharges simulated with ASTRA-TGLF for this thesis. Not every simulation was also implemented in an IDA-KM fit, as some simulations were mainly used to test the limits of the kinetic model.

Low-confinement mode discharges cannot reach reactor-relevant performances. However, important turbulence measuring diagnostics such as backscattering reflectometers work better with low density as the cut-off frequency moves further towards the plasma core. Thus, L-mode plasmas are preferred to both study turbulence [24] and validate turbulence simulations. Discharge #36974, which was part of a turbulence study, was chosen as a first test to see if the IDA+KM leads to profiles that are more in line with our theoretical understanding. For the comparison, the usual curvature prior has been turned off when fitting the IDA+KM profiles.

When combining IDA with the log gradient from the kinetic model, one finds that the resulting profiles generally lead to better matching fluxes, as shown in figure 5.2. The Q_e profiles are much less peaked, with the heat flux only sharply rising close to the boundary condition or in the innermost core. Q_e now almost matches the electron heating power in the mid-radius region, which has the smallest simulation uncertainty. In this region, the

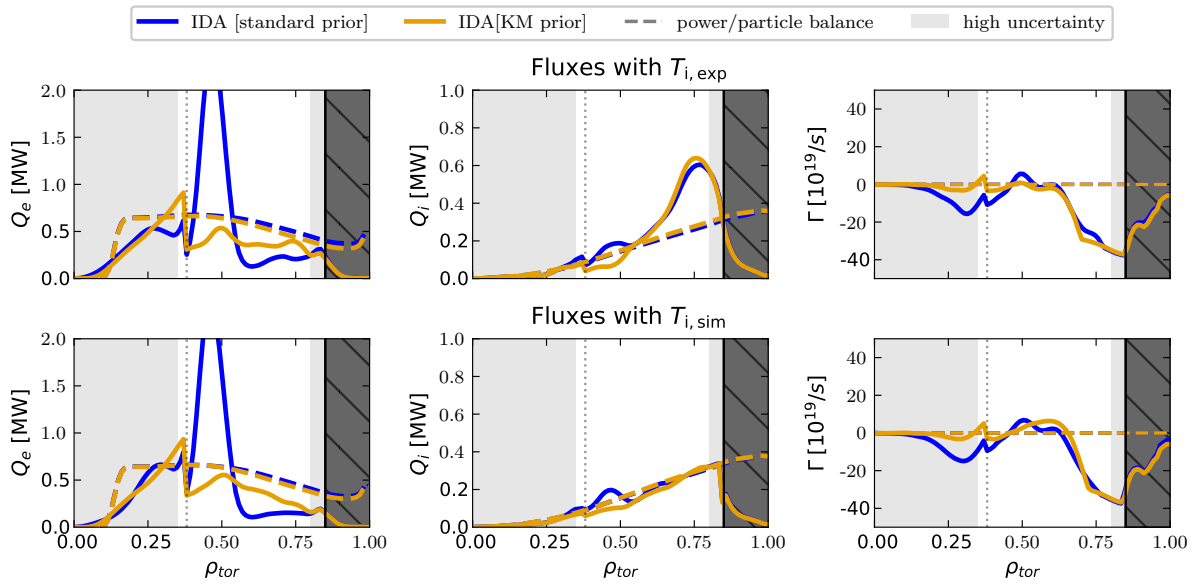

Figure 5.2.: Heat flux and particle fluxes of the standard IDA and IDA with KM prior for discharge #36974 at 3.404s. The electron heat flux match is improved for both experimental and simulated ion temperature profiles. The ion heat flux matches well in the core as the log gradients of the experimental and simulated Ti are roughly the same. At $\rho_{tor} \approx 0.75$, the experimental gradient is too large, and the turbulence is largely ITG driven, leading to the spike in Q_i. Generally, the particle flux match is difficult to achieve for a snapshot when the particle source and flux are so small. The match for Γ is relatively good compared to other L-mode discharges. The power balance for both IDA profiles was plotted to show that these stay relatively constant with the different profiles as input. The q=1 surface is again shown as a faint dotted line.

root-mean-squared error between Q_e and electron heating has decreased by almost a factor of 4. At the q=1 surface, the electron heat flux suddenly jumps as the additional diffusion acts on the plasma. This jump can be reduced with smaller uncertainty in the sawtooth region, which would require a better model.

As the T_i profile is an extremely relevant part of calculating the fluxes, Γ, Q_e and Q_i using the ASTRA-TGLF input $T_{i,exp}$ and simulated ion temperature $T_{i,sim}$ are shown respectively. It was seen that the importance of T_i varies between types of turbulence. In this L-mode case without NBI heating, the Q_e match is improved independently of the used ion temperature. For all analyzed plasmas, the Q_i match was improved more strongly when using the simulated T_i profile. This enhanced ion heat flux match is a motivation source for implementing a kinetic modeling prior to IDI in the future, especially if "only" beam blips are available. This thesis found that for the experimental T_i, the Q_i match is worse when ion temperature gradient drivers dominate turbulence as the ion temperature gradient is the most crucial variable (see also section 5.3). In the right panels, one can see that the particle flux mostly matches the expected values. Such a good match is not achieved for most of the examined cases, with the particle flux match often being especially bad in the core. In general, the difficulties in simulating the density input and flux have led to Γ not being a validation metric in [87, 77,

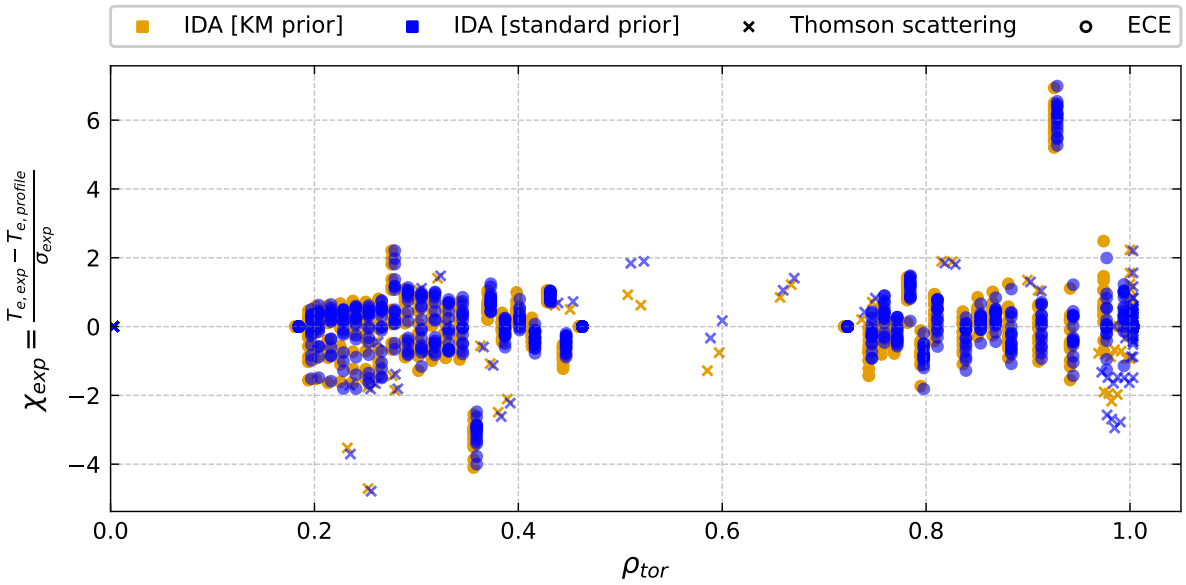

Figure 5.3.: Comparison of the T_e residuals for the different IDA profiles. The ECE residual is slightly larger for the IDA with KM prior, but no systematic or strong deviation stands out. For completeness, the Thomson scattering measurements have been plotted as well, which one can see most clearly as lonely measurement points in the ECE gap where there is a larger difference between the two profiles (see figure 5.4), but it is not necessarily a worse fit of the data. To better tell the two shotfiles apart, the residuals have a radial offset of $\rho_{tor} = 0.03$.

140, 88].

While the heat fluxes are our metric of choice in determining the profile's agreement with transport physics, one needs to prevent the kinetic model from dominating the measured data. In figure 5.3, one can see the residuals of the T_e measurements compared to the profiles. For L-mode discharge, no systematic worsening of the data fit is found. The largest residual remains a stray ECE channel close to the separatrix, which is properly mitigated by the outlier-robust Student's t-distribution. The ECE channels closest to the gap have a slight offset, but these channels generally are harder to calibrate correctly. To further strengthen our belief that the match has not worsened, the Thomson scattering temperature measurements in the ECE gap have been plotted, which are not worsened by the new prior even though the offset is more visible.

Of course, it could also be that diagnostics have been poorly calibrated or measurements are otherwise problematic. For now, it is suggested to double-check both simulation and data if large residuals are present for the diagnostics.

Comparing the standard IDA and IDA+KM profiles in figure 5.4, the actual values of n_e and T_e almost do not change in the areas where experimental data is present. However, their log gradients became significantly smoother. The highest deviation in T_e is in the aforementioned ECE gap $0.45 \leq \rho_{tor} \leq 0.7$. The ASTRA-TGLF simulation also has a pronounced effect in the core, even with the large core uncertainties used. Instead of reaching unrealistic heights as in

figure 3.9, T_e reaches comparable values to IDA even with the curvature prior was turned off. The density has largely remained unchanged, with only the center core being slightly elevated.

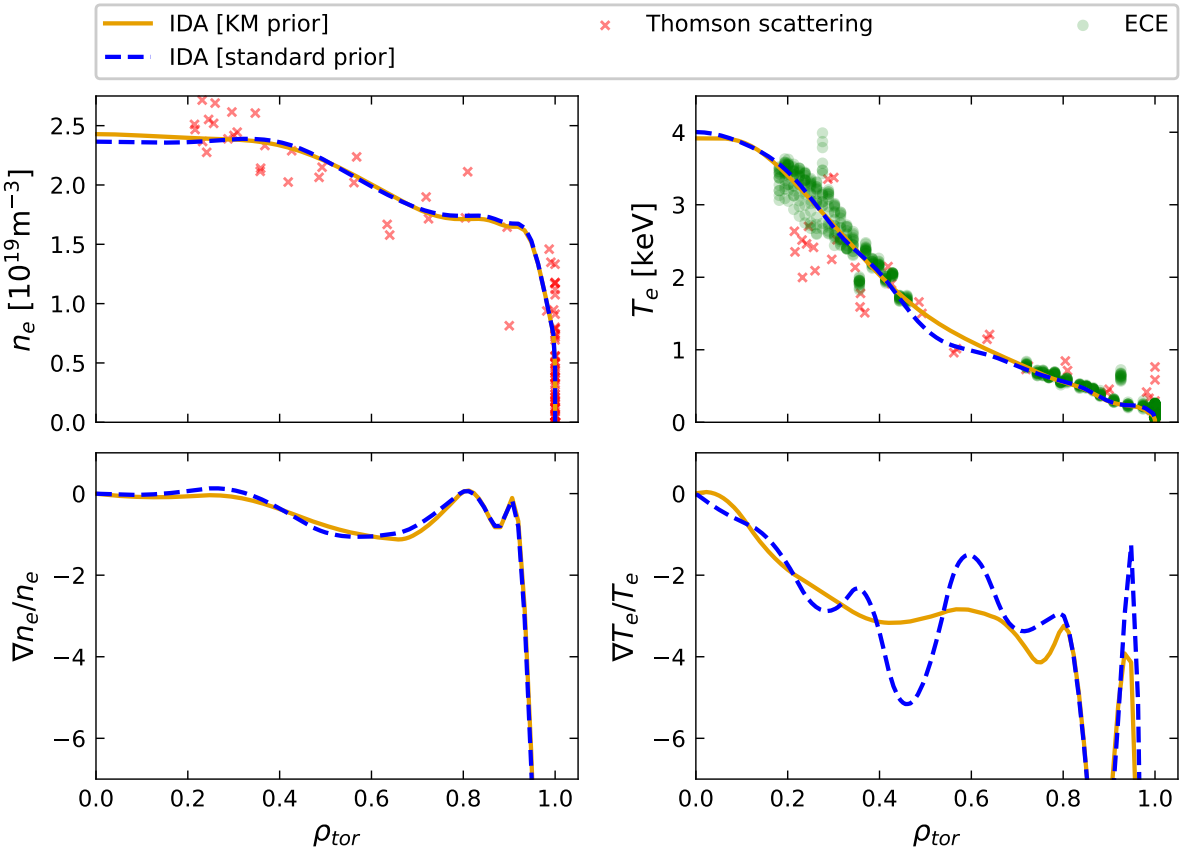

Figure 5.4.: Comparison of IDA profiles with and without the kinetic model. The profiles are largely the same where ECE data was present, with the density remaining practically unchanged except for the innermost core.

This discharge was also used to test the kinetic model prior to other IDA fitting procedures. For a more advanced uncertainty estimate, IDA can also be run with a more computational MCMC method. The Markov Chain Monte Carlo IDA+KM also has a smoothed T_e with a reduced standard deviation of the drawn profile samples compared to the standard IDA-MCMC. Furthermore, the effect of reducing the simulation uncertainty or having diagnostics missing was tested. As expected, this leads to a better flux match as IDA+KM can stronger weight the kinetic model.

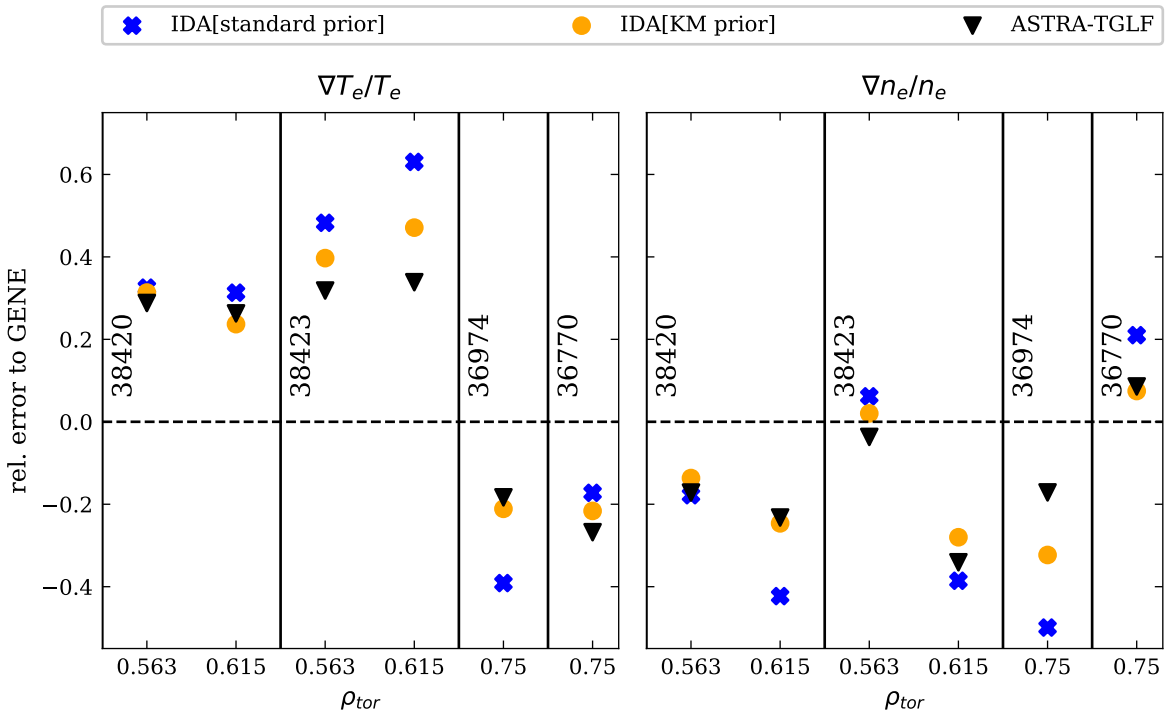

Figure 5.5.: Comparison of IDA, IDA+KM, and ASTRA-TGLF log gradients to GENE simulations for several radii and discharges. A negative error means that GENE predicts larger gradients. The dotted line represents the GENE simulation's gradient, which best matched the heat flux while still within the experimental error bars. In most cases, the IDA+KM gradients are closer to the GENE simulation, with the exception being the sole examined Hydrogen discharge #36770. Using IDA+KM as a starting point could save valuable computing time when conducting high-fidelity turbulence validation.

5.2.1. Application as GENE input

Multiple non-linear local GENE simulations were recently validated against a combination of turbulence measurements [87, 123] for various radii, heating schemes and ion species. The GENE simulations used fine-tuned IDA and IDA-MCMC profiles in which diagnostic coordinates and spline point positions were shifted, and spline points and outlying diagnostic channels were removed to achieve the best possible fit and provide a smooth gradient without a strong curvature prior. In the GENE simulations, profile gradients were varied for these papers to match electron and ion heat fluxes (see section 4.3.1). IDA+KM was applied to these four discharges, as well as ones with increased heating, and obtained improved flux matches in all cases compared to the standard IDA.

In figure 5.5, one can see the relative difference between a selected GENE simulation and IDA(+KM) and ASTRA-TGLF gradients. For the plot, the GENE simulation with the best-combined heat flux match for ions and electrons was chosen while the GENE gradients were still inside the calculated error bars. A negative error indicates that the GENE simulation predicted larger gradients. In most cases, the IDA+KM gradient is closer to the predicted

GENE simulation than the standard IDA. ASTRA-TGLF usually has gradients even closer to the best GENE simulation, so an IDA+KM with lower KM uncertainties could have been beneficial in this case.

Using IDA+KM as an initial input for GENE could help save significant computational resources as fewer simulations are needed to achieve flux matching. This would allow GENE simulators to vary more parameters in the search for the optimal fit. For example, for the best heat flux match, an extra impurity had to be added to GENE simulations for two of the discharges or varying $\frac{T_e}{T_i}$ within the error bars. Adding an extra ion species greatly increases the computational cost and is thus not immediately done from the start. For the sole Hydrogen discharge #36770 IDA+KM T_e gradient is slightly worse, which could be an outlier or point to more work needed to model hydrogen discharges correctly. In section 2.4.3, results of several other authors are presented, which pointed to problems with TGLF when changing main ion mass.

As shown in e.g. [87, 123], measurements of the electron temperature fluctuations using CECE and Doppler backscattering measurements of electron density fluctuations can be used to validate turbulence codes and are available for the discharges above. As this project progresses, TGLF simulations using different IDA profiles as input could be compared to these measurements as a further metric in determining a profile's agreement to transport physics.

It is important to note that while in these L-mode discharges, IDA+KM could have been used to find a converged GENE gradient more efficiently. However, the actual GENE validation must still be done against a standard IDA profile, as it is crucial to keep theory and experimental measurements separate during validation. While these IDA+KM profiles will be helpful for many different applications at ASDEX Upgrade, they will be clearly marked to avoid accidental use in transport validation investigations.

5.3. H-mode discharges

Shot	P_{NBI} [MW]	P_{ECRH} [MW]	Description
ICRH heated discharge and blowfish study			
30506	22	0	ICRH 3.5 MW
EDA H-mode with inverted T_e profile			
38830	0	3	EDA H-mode, inverted T_e
IMEP validation [54]			
33616	5.0	1.16	power scan
33173	10	2.0	fueling scan
Tearing modes			
38926	6.5	2.1	
Advanced scenarios			
36053	12.5	4.25	T_e ITB
39230	7.5	1.6	T_i ITB, fast ions
39233	7.5	1.6	no fast ions 2.73
Torque study by NBI beam modulation [142]			
41550	4.5	0.8	

Table 5.2.: H-mode discharges simulated with ASTRA-TGLF for this thesis. Not every simulation was also implemented in an IDA-KM, as some simulations were mainly used to test the limits of the kinetic model.

This section focuses on the H-mode discharge #33616 at 5.45s. As outlined in Chapter 2, H-mode discharges have a transport barrier at the edge, leading to higher T_e and n_e values in the plasma core. The same turbulence physics applies to the core as when modeling L-mode plasmas. Due to their higher performance, H-mode discharges are the desired state for future power plants and, thus very relevant to future tokamak modeling.

Like most turbulence codes, TGLF cannot capture the physics at the pedestal, so the user must be careful in setting the ASTRA-TGLF boundary condition. For this proof-of-concept work, it was decided to keep the boundary at $\rho_{tor} = 0.9$, which could, in the future, be decreased to a smaller value by implementing an MHD stability code as in [54].
At 5.45 seconds, discharge #33616 offers an advantage over the L-mode discharge #36974 described in the previous chapter. This advantage lies in the constant availability of NBI heating, supplied by two 2.5 MW beams, which allows for continuous charge exchange data. As a result, more reliable measurements of T_i (ion temperature) and toroidal rotation are available. Additionally, the q=1 surface at this particular time step is positioned further inward, making the sawtooth region less significant.

Figure 5.6 illustrates the simulation results of the discharge. Notably, due to the H-mode

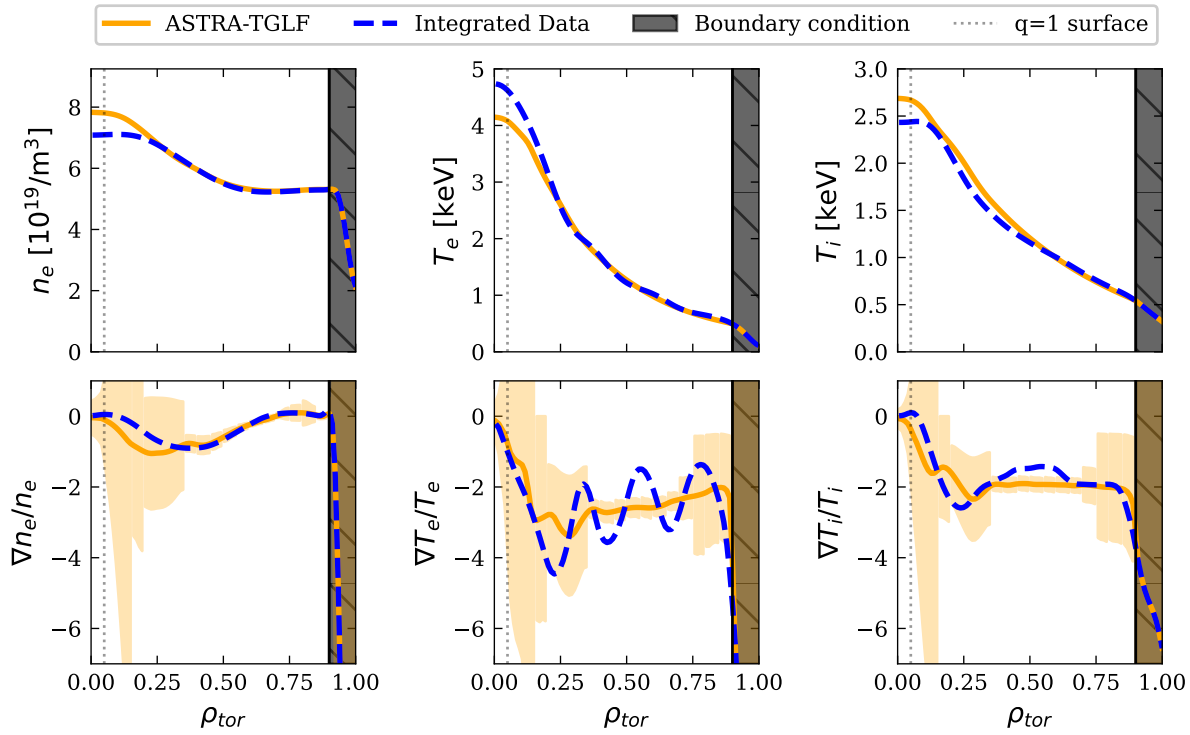

Figure 5.6.: ASTRA-TGLF simulation of the H-mode discharge #33616. The simulation matches the input profiles well, with both T_e and T_i gradients being smoothed. The density profile is slightly raised in the core, which would very slowly keep rising with further simulation time as seen in 4.12.

pedestal, discharge #33616 achieves higher n_e values compared to #36974, starting from $\rho_{tor} > 0.9$ and extending into the core region. The electron temperature pedestal is less obvious, measuring approximately 1 keV, which is still a large performance gain. It is worth noting that the core $T_{e,sim}$ is lower than the corresponding $T_{e,exp}$, mainly due to a smaller gradient within $\rho_{tor} < 0.3$. Nevertheless, the fit was considered to be acceptable since experimental core values fluctuate between 3.2 to 4.8 keV during sawtooth cycles.

The density is overestimated in the core and slightly beyond the values observed before a sawtooth crash. However, its gradients fall within the error bars of the experimental values. On the other hand, T_i shows a better match with the experimental data compared to the non-NBI case, with T_i and the gradient aligning well for $\rho_{tor} \geq 0.2$. Although the core value is lower, it is consistent with the data obtained during a sawtooth crash.

Furthermore, ASTRA-TGLF once again predicts that T_e and T_i exhibit smoother log gradients than the input data had.

Figure 5.7 compares IDA+KM to IDA for #33616 at 5.451s. IDA+KM again did not significantly change the absolute values of T_e but has a much smoother log gradient. The discharge has more spread-out ECE measurements than the L-mode discharge, so the kinetic modeling prior can never dominate in a region. The choice to use log gradients to compare experimental and simulated profiles is confirmed, as the IDA+KM profile still matches the

data in the core even though it simulated considerably lower temperatures. The density and its log gradient are almost unchanged compared to the standard prior.

Unsurprisingly, as the profiles are so close to each other, the diagnostic residuals of the IDA+KM profile do not deviate strongly compared to the IDA profile.

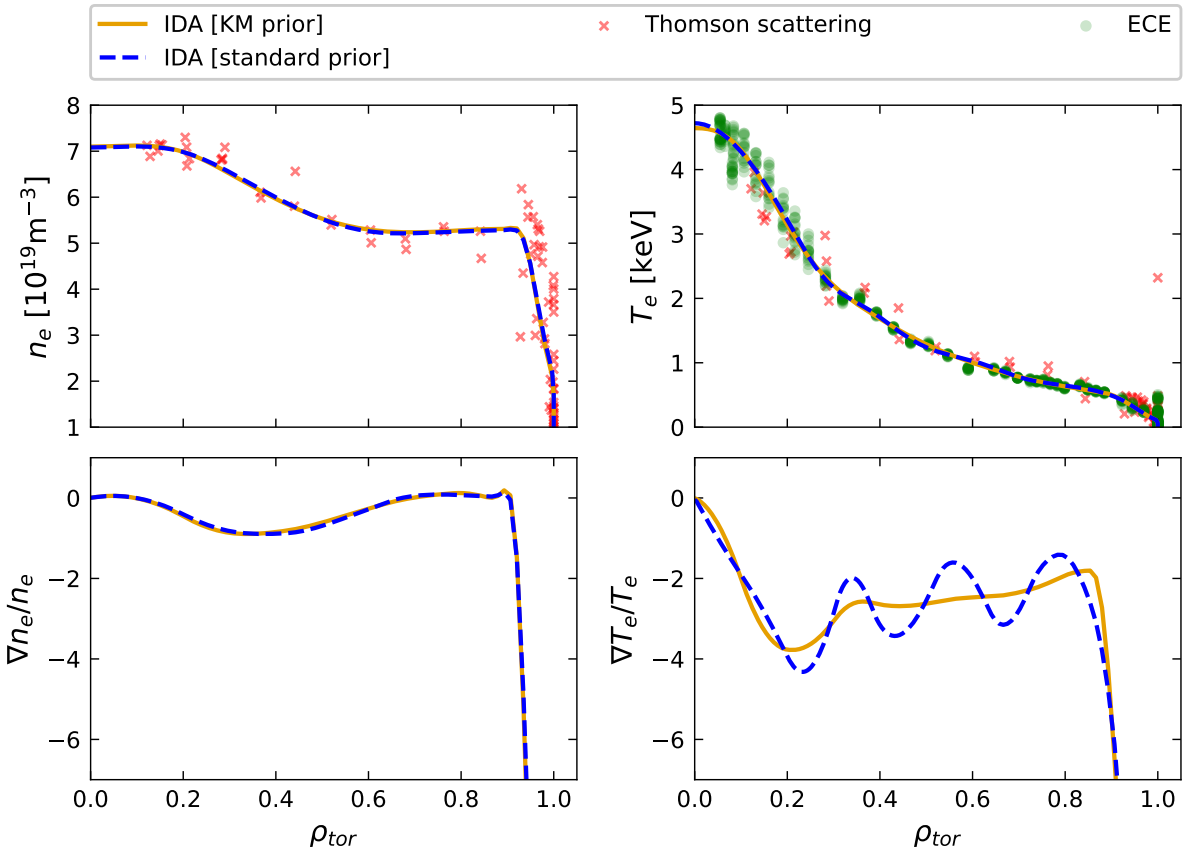

Figure 5.7.: IDA and IDA+KM profiles of #33616 at 5.451s. The absolute values of both profiles have hardly changed with the IDA+KM because the diagnostic coverage has no larger gap. T_e gradient being much smoother than the original IDA. The density has remained largely unchanged.

The Q_e flux in figure 5.8 matches the expected heating power values calculated by TORBEAM and Rabbit in the region with the lowest uncertainty when using the $T_{i,sim}$. Interestingly both IDA and IDA+KM profiles match the initial rise at $\rho_{tor} \approx 0.15$ with the following spike being much smaller for IDA+KM. This early matching is attributed to the existence of ECE data in the core. As the discharge has significant ion temperature gradient-driven turbulence, using the experimental $T_{i,exp}$ does not lead to an improvement. This high dependence on the ion temperature gradient again motivates a possible inclusion of a kinetic modeling prior to IDI. A new IDI shotfile using an IDE equilibrium matches the simulated T_i and its gradient further into the core and is shown in the appendix A.2. The profile's improvement underscores the equilibrium's importance when mapping diagnostics to the field lines.

As mentioned in section 5.2, the particle flux in the core is off due to the slow convergence

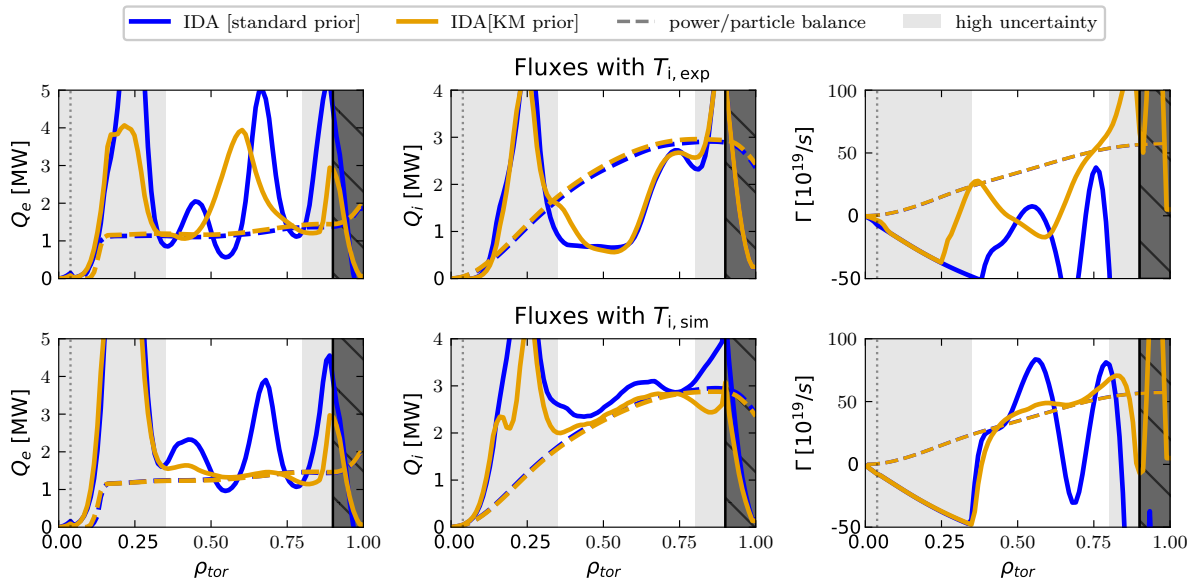

Figure 5.8.: Heating power and heat flux of IDA and IDA+KM for both experimental and simulated T_i of #33616. As the H-mode discharge has more ion heating through NBI, the discharge is dominated by ITG turbulence. IDA+KM leads to a better matching of the expected flux only when using $T_{i,sim}$ from figure 5.6 as input.

of the ASTRA-TGLF particle flux. The particle flux displayed in figure 5.8 matches the flux with simulated T_i values well, meaning that the match to the expected particle flux could only be improved upon by running the simulation for much longer. This simulation still had a mismatch between input and flux even after running the simulation ten times longer and was not continued for practical reasons.

5.4. Non-standard discharges

ASTRA-TGLF is known to be capable of simulating standard discharges. However, even with the progress of more advanced saturation rules and included physics in TGLF, some discharges are still difficult to model. An initial misgiving against the kinetic modeling prior was a possible negative impact in these non-standard situations. This section shows two examples where the kinetic model fails to capture the physics properly, but IDA+KM is not negatively impacted and still fits the measured data.

5.4.1. Advanced Scenarios

Advanced Scenario discharges are made to plan for future tokamak power plants by trying to achieve high plasma performance or extra long pulses by non-inductive current drive [148]. Discharges with even higher pedestal pressure than the traditional H-mode called *Super H-mode* [149] aren't included in this discussion.

Some advanced discharges achieve higher temperatures in the core by turbulence suppression in the core, on top of the usual edge transport barrier achieved in H-mode. It is still an active field of study on how the suppression is achieved, with a combination of fast ions and fishbone modes being likely candidates. $E \times B$ shear is thought not to be as relevant at ASDEX Upgrade[21]. ASTRA, combined with a quasi-linear turbulence model, is known to fail for advanced scenarios involving internal transport barriers [63, 62, 61].

In discharge #39230 (see figure 5.9, one can see an example of a peaked ion temperature most likely due to fast ions. Discharge #39233 does not have this high ion temperature, raising the question of whether there are more effects than just the fast ions. Both discharges have more than 7 MW of NBI and 2 MW of ECR heating at the plotted time point. While ASTRA-TGLF couldn't properly capture the peaked T_i, the electron temperature matched well enough that the gradients would not negatively impact IDA+KM. A slightly better agreement between ASTRA-TGLF and the experiment was found by diluting the main ions with fast ions. This is known to suppress the ITG driven turbulence [41], but the effect is not large enough to replicate the GENE-TANGO simulation.

The #39230 discharge was also studied using GENE-TANGO, which effectively functions as a high-fidelity ASTRA-TGLF simulation. The global GENE simulation took both electromagnetic and fast particle effects into account. TANGO performs tasks similar to ASTRA, combining heating from subroutines such as RABBIT and calling equilibrium solvers [61, 150]. In figure 5.9 one can see that GENE-TANGO is able to reproduce the measured ion temperatures if fast ion effects are taken into account and otherwise struggles similarly to ASTRA-TGLF. Preliminary GENE-Tango simulations have been performed on the discharge #39233, suggesting that changes in the magnetic geometry might be strongly related to the different thermal profiles observed in the experiment. However, more in-depth analyses are required and will be performed in the near future.

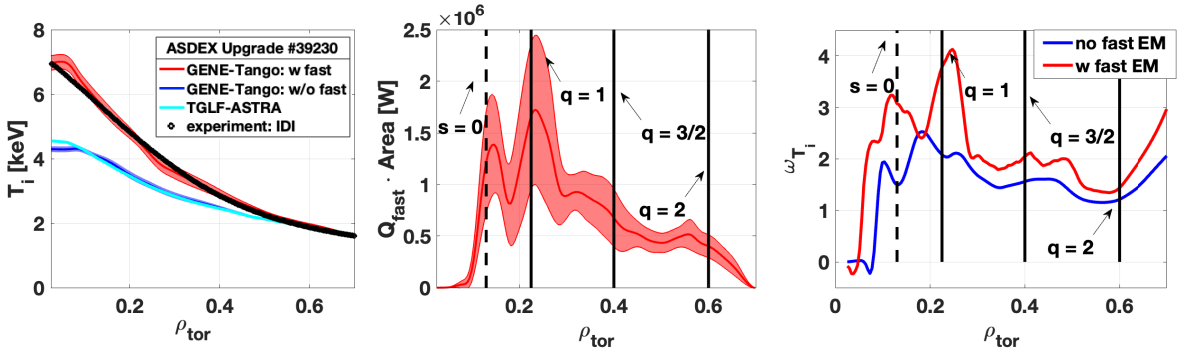

Figure 5.9.: Comparison of GENE-TANGO and ASTRA-TGLF. The fast ion content has peaks at the q=1 and shear s=0 surfaces. These fast ions seem to interact with high-frequency Alfvén eigenmodes to create an internal transport barrier that raises T_i. Currently, the role of fishbone instabilities at the q=1 surface in further reducing the turbulence is being investigated. One can see that ASTRA-TGLF nicely matches GENE-TANGO without fast ions. Figures based on [43].

To test the potential "negative" impact of the kinetic modeling prior, IDA+KM has also been applied on discharge #36053 where the electron temperature is strongly peaked in the core.

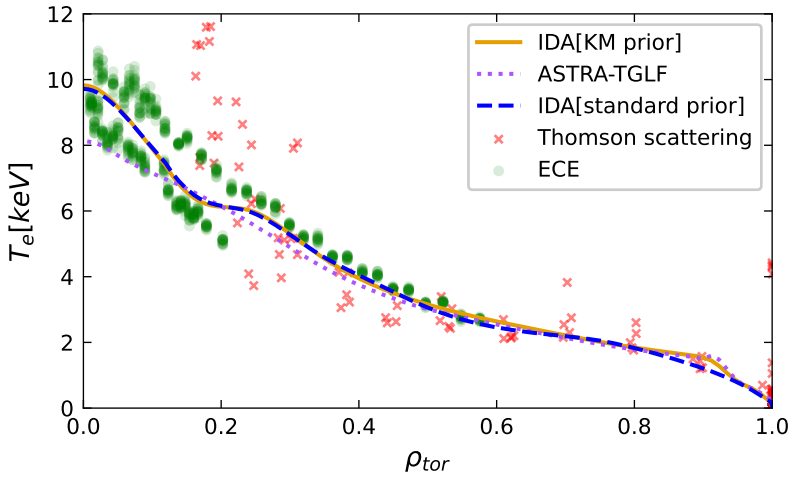

Figure 5.10.: Discharge #36053 with IDA, IDA+KM and the ASTRA-TGLF simulation. ASTRA-TGLF is not able to capture the profile peaking at around $\rho_{tor} < 0.2$, but due to the high uncertainty, it does not negatively affect the IDA-KM profile. The ECrad forward model properly captures the ECE pseudo radial displacement.

Unlike in the #39230 discharge, the gradient suddenly flattens at the q=1 surface, but then rises steeply. With around 10 MW of NBI and 4.25 MW ECR heating, the discharge had the most electron heating of all discharges analyzed. In fig. 5.10, the ASTRA-TGLF simulation smoothed the gradient for $\rho_{tor} \geq 0.6$ where ECE data is missing. The difference between simulation and experimental data in the innermost core does not seem to have negatively impacted IDA+KM due to the high core uncertainty assigned to the kinetic model.

ASTRA and TGLF are constantly being improved upon and hopefully, in the future, a better understanding of the physics of the internal transport barrier will make it possible to reduce uncertainty in these discharges without negatively impacting the IDA+KM fit.

A side note is the pseudo radial displacement of the ECE data due to relativistic shine through by the high-field side, explained in more detail in [109]. The assumption of a single temperature on a flux surface is still correct, and IDA was able to properly fit the data through its forward models.

5.4.2. Neoclassical tearing modes

If the gradient in the plasma current profile is too strong, the plasma will go into an energetically lower state by tearing the magnetic field lines and producing magnetic islands [13]. This change in field topology introduces a radial aspect to the magnetic field lines at the mode's location. As transport along the field lines is almost instantaneous, these magnetic islands flatten temperature and density profiles. As initial perturbations are self-amplified if a flux surface closes into itself, tearing modes are often found on rational flux surfaces. Discharge #38926 has a large 2/1 mode that locks over time and visibly flattens electron and ion temperature data at around $\rho_{tor} = 0.6$.

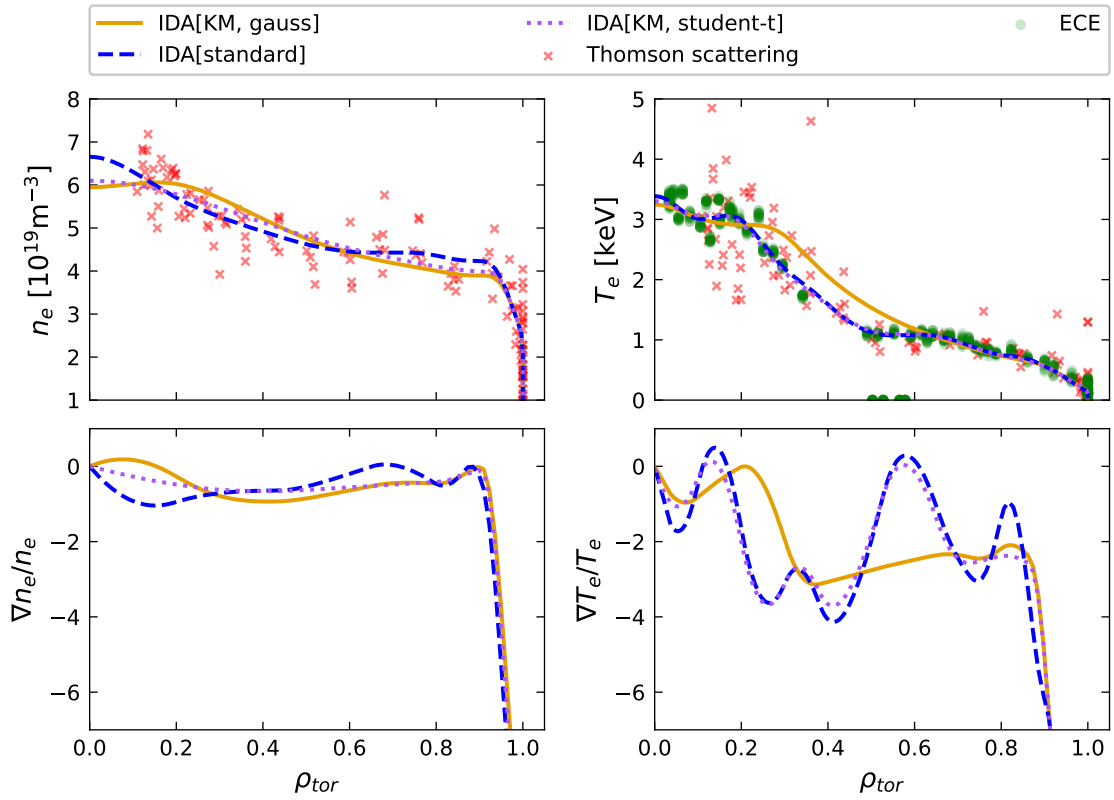

Figure 5.11.: Discharge #38926 with IDA, IDA+KM profiles. ASTRA-TGLF cannot predict the tearing mode at around $\rho_{tor} \approx 0.6$; thus, the kinetic model cannot be trusted. When using a Gaussian distribution for the prior, the resulting profile is not matching the data. A Student's t-distribution fixes this problem, with the temperature profile being almost indistinguishable from the standard IDA. The gradient is also similar with a small smoothing at $\rho_{tor} \approx 0.8$.

ASTRA-TGLF is not able to simulate MHD events such as tearing modes. It thus badly overestimates both density and temperature gradients at the position of the tearing mode. Closer to the core, the kinetic model should still be applicable with the simulated gradient matching the experimental one in the core (not shown here). However, the 2/1 mode's size is large enough that the incorrectly modeled gradient could severely damage the IDA+KM fitting process if the uncertainty of the kinetic model is not properly chosen.

Figure 5.11 in orange shows the IDA+KM model where a Gaussian distribution is applied to the kinetic model as in the cases above. The gradient of the T_e profile does not go to zero, thus not capturing the physics of the discharge involved. The temperature profile ignores the ECE measurements close to the NTM, and T_e is consequently overestimated for $\rho_{tor} = [0.2 - 0.6]$.

A simple method to avoid this mismatch is using a Student's t-distribution. The Student's t-distribution is less susceptible to outliers compared to a Gaussian distribution and is also plotted in figure 5.11 using ν=1, which is equivalent to a Cauchy distribution. The large tails are enough for the IDA with KM profile to match the initial IDA profile at the position

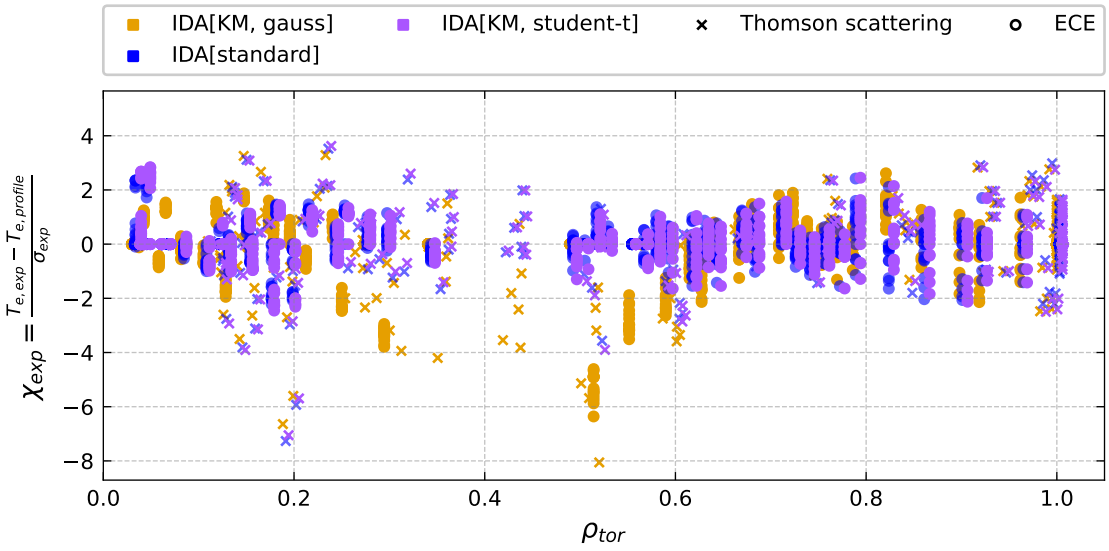

Figure 5.12.: ECE residuals of the profile shown in figure 5.11. The large error of the Gaussian IDA+KM profile is visible radially inward of the NTM ($\rho_{tor} \leq 0.6$). This is the worst-case scenario of the kinetic model overruling data from the diagnostics. It can be avoided by utilizing a Student's t-distribution.

of the tearing mode while still smoothing the profile at around $\rho_{tor} = 0.8$. Using a Cauchy distribution in the previous L- and H-mode cases leads to a negligibly reduced match in Heat flux. The "safe" option would be to use the Student's t-distribution as a default.

IDA+KM can handle the advanced and NTM discharges by using a Student's t-distribution. They also show the difficulty of correctly and self-consistently quantifying uncertainty for the kinetic model. The limited applicability of input sensitivity analyses for ASTRA-TGLF is apparent, as the model is just wrong in these cases and the error will not drastically change with input.

IDA+KM has been shown to improve heat and particle fluxes for various L- and H-mode discharge types without substantially degrading the measurement match. The flux match is achieved by bringing the logarithmic gradients more in line with the ASTRA-TGLF simulations, which amounts to a more sophisticated smoothing operation. However, there are still further ideas that could improve the match. For ITG-dominated discharges, the ion temperature gradient plays a large role thus motivating kinetic modeling for the ion measurements. The ASTRA-TGLF simulations can have negative effects if a Gaussian distribution for the likelihood is used, thus motivating the use of a Student's t-distribution.

The assumption that the prior's points are independent of each other is not addressed in the section above. This is, of course, not the case, and this assumption would lead to a strong weighting of the kinetic modeling prior if one would keep adding points to the simulation as the kinetic model's residual would automatically rise. A possible solution could be some averaged value over a relevant length, such as the turbulence scale length.

6. Extensions of the kinetic model

While ASTRA-TGLF is a well-validated model, there are turbulence model alternatives implemented in ASTRA. In this chapter, Qualikiz and fast solvers based on learning from TGLF and QLK will be presented. Having multiple solvers of different fidelities and speeds is critical for developing a multi-fidelity uncertainty quantification approach [151], which is one of the goals of a partnering PhD student.

IDA+KM results until now were only shown with a boundary condition and for a steady-state plasma. The IMEP framework is presented, as well as ASTRA-TGLF results for an L-mode discharge in which the heating mix was twice varied.

6.1. Qualikiz and neural network turbulence solvers

Like TGLF, Qualikiz (QLK)[152] is a quasi-linear turbulence solver for the linearized gyrokinetic Vlasov equation using KineZero and GENE for its saturation rules, which can be coupled to ASTRA. For an in-detail derivation, see [153].

While it assumes a circular shape and only considers electrostatic perturbations, it is faster than TGLF-SAT2. For this thesis, QLK version 2.8.1 was used, which has been updated with a new Krook collision operator based on GENE simulations [154] since the problems were described in [90]. While TGLF is usually the turbulence solver of choice to be coupled with ASTRA at AUG, QLK's speed and improvements make it a valid option for IDA-KM.

In figure 6.1, one can see that, like in [90], the coupling of ASTRA and QLK still can be problematic for high $\frac{T_e}{T_i}$ caused by large electron heating. One sees that T_e is still simulated as too high, and the density is underestimated. However, even without reducing the collisionality and thus driving more turbulent flux, the results are a vast improvement in the matching of the T_i and T_e compared to [90], showing that QLK is on the right track. The match in T_e is further improved if one keeps the density assigned to the experimental profile, shown in the figure as $\mathrm{QLK}_{\mathrm{n_e=const}}$. The higher density leads to the heating power being spread to more electrons and more power being radiated.

A better match is seen for the H-mode discharge #33616 discussed in section 5.3. The neutral beam injection leads to a higher ion heating, thus increasing Q_i/Q_e. The electron temperature is nicely matched for both n_e assigned and evolved cases. Despite the problems simulating the density, Qualikiz can be used to double-check the suggested temperature gradients from TGLF at ASDEX Upgrade.

Users can freely decide on the turbulence solver used in IDA+KM. QLK is preferred over TGLF for simulating the JET tokamak, possibly due to the QLK saturation rules being fitted

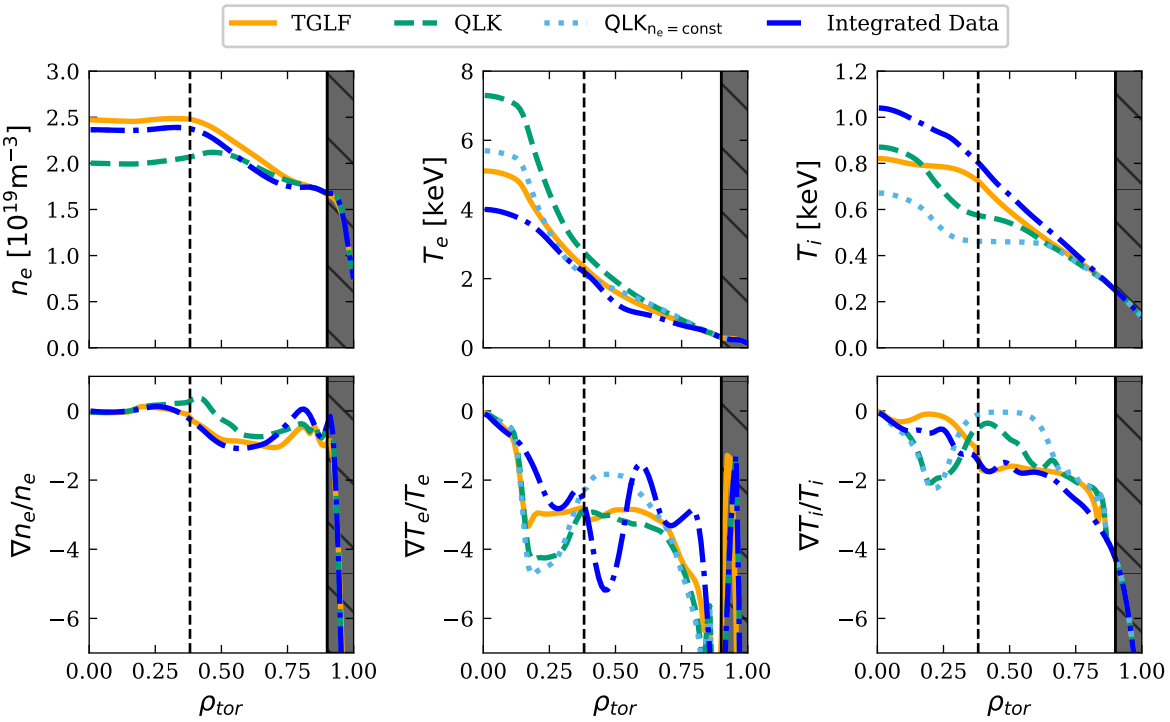

Figure 6.1.: L-mode discharge #36974 simulated by ASTRA using different quasi-linear turbulence solvers. While Qualikiz has made progress in discharges with large electron heating, the $\frac{T_e}{T_i}$ still leads to problems for the updated QLK. This match can be improved upon by keeping the density constant. The q=1 surface is given by the dashed vertical line.

on high-fidelity JET simulations. As IDA and IDA-KM are implemented on more devices, having the freedom to choose a solver is valuable. For this thesis, QLK simulations were mainly used for double-checking results obtained with TGLF.

Neural network turbulence solvers

For QLK, 10^4 times faster neural network solvers exist called QLKNN [155, 156]. The 2021 version of QLKNN-jetexp-15D model and QLKNN-hyper-10D were implemented and tested for this thesis. The 10D network was trained on ten inputs (R/L_{T_e}, R/L_{T_i}, R/L_{n_e}, q, $\hat{s}$, r/R, T_i/T_e, the collisionality ν^*, Z_{eff} and an additional rotation rule for flux suppression) in a Latin hypercube structure [157].

In Latin hypercube sampling, each parameter range is partitioned into intervals, and each interval is sampled once. This achieves a better coverage of the full parameter space compared to a standard grid sampling algorithm. In 2D, this is similar to a chess board with only rooks in which no figure can be captured on the next move. With this technique, it is obvious if the neural network is being used with values outside the training range.

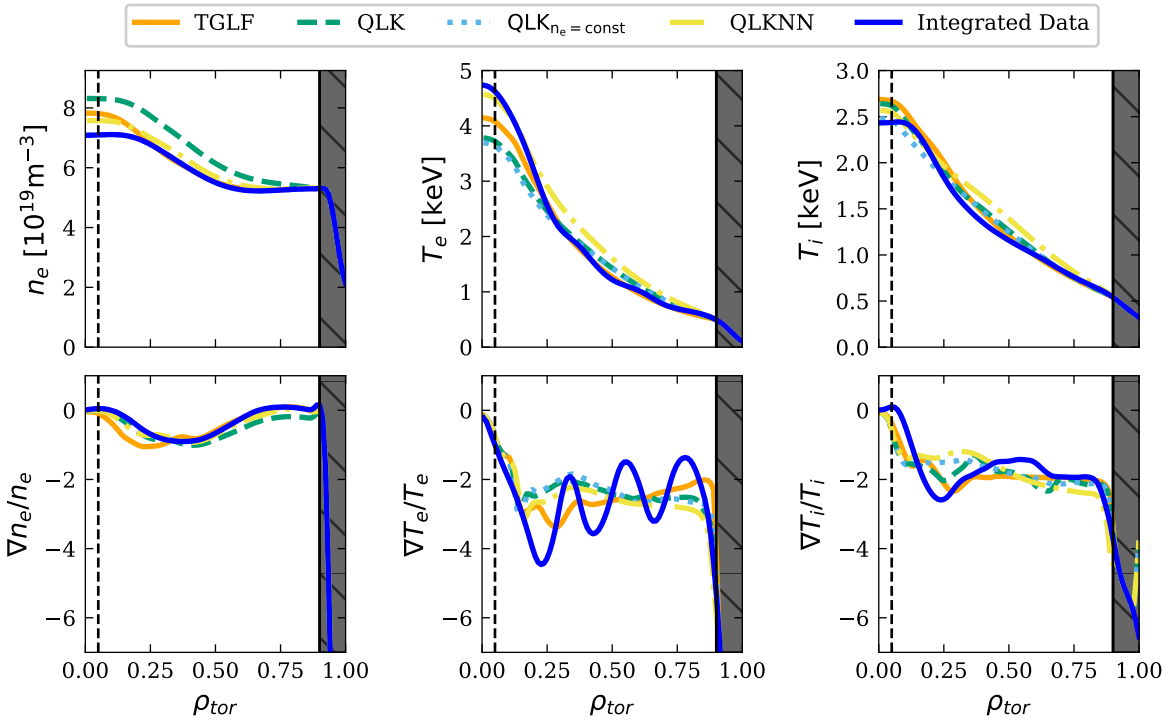

Figure 6.2.: The H-mode discharge #33616 case has better matching QLK due to the higher ion heating fraction. The neural network solver also leads to good results, making a fast kinetic model for an entire discharge possible in the future. The q=1 surface is given by the dashed vertical line.

The 15-dimensional model has an impurity fraction and its gradient, as well as pressure and velocity input, added to it. Training in a Latin hypercube structure would need too many samples, so training was done with experimental values taken from JET experiments instead. A committee of neural networks calculates the variance against an acceptance threshold to warn the user if the model is being used outside of the training range. While this thesis found a better match using the QLKNN-jetexp-15D model combined with ASTRA, the clear boundaries of the hypercube make it easier to assign uncertainties.

In figure 6.2, the QLKNN-jetexp-15D neural network solver is shown to perform well for the H-mode discharge and is thus a valuable option for simulating an entire discharge, which will be discussed in subsection 6.3. In some of the high $\frac{T_e}{T_i}$ discharges QLKNN was tested on the neural network and actually outperformed the QLK model by simulating lower temperatures. A possible reason could be that the neutral network was trained not to overfit, and so it has been so generalized that it just assumes a higher energy flux, or perhaps it is a coincidence. One should not assume that QLKNN is a better physics model than the code it was trained on.

For this thesis, TGLFNN [158] was also implemented in ASTRA, but the simulations have not been successful enough to warrant its use as a prior(see figure 6.3). Possible explanations for the bad fit could be the model's age and its focus on D3D data. TGLFNN is based on TGLF Sat-0 and takes 17 parameters as input, with one input being the Carbon impurities density gradient. As the D3D tokamak's vessel is made of Carbon, the impurity plays a larger role there. Work is being done to update the neural network model with newer saturation rules. Recently, a new neural network trained on GENE simulations was published [159], which will be implemented in ASTRA in the near future.

6.2. Moving IDA+KM towards the edge

As was discussed above, ASTRA-TGLF is run using a boundary condition usually set at around $\rho_{tor} = 0.9$. For L-mode discharges [53] has shown that ASTRA-TGLF using saturation rule 2 is capable of capturing the physics with no boundary condition. However, it is not yet able to model the large turbulence suppression at the edge during H-mode.

In [54], the creation of the IMEP framework is described, which is capable of simulating profiles up to the last closed flux surface in H-mode. IMEP couples an ASTRA simulation to the MHD stability code MISHKA [160] and a two-point scrape-of-layer model. The SOL model provides ASTRA with the electron temperature and density as well as the neutral density on the last-closed flux surface. It further assumed $T_{i,sep} = 2T_{e,sep}$. MISHKA tests the peeling ballooning mode stability [13] of the pedestal. The IMEP simulation shown in figure 6.5 differs from this thesis's ASTRA-TGLF by using TGLF SAT-1, an additional pedestal transport model and a different equilibrium code Helena [161]. The entire IMEP framework is capable of running independently from experimental profiles with high accuracy. For example, it matched the stored energy in AUG discharges better than the ITER scaling law IPB98(y,2)[8]. IMEP does need the B_{tor}, the external heating sources, deuterium and nitrogen fueling rates as well the Z_{eff}. Potentially, with progress from [56] and [162], the plasma

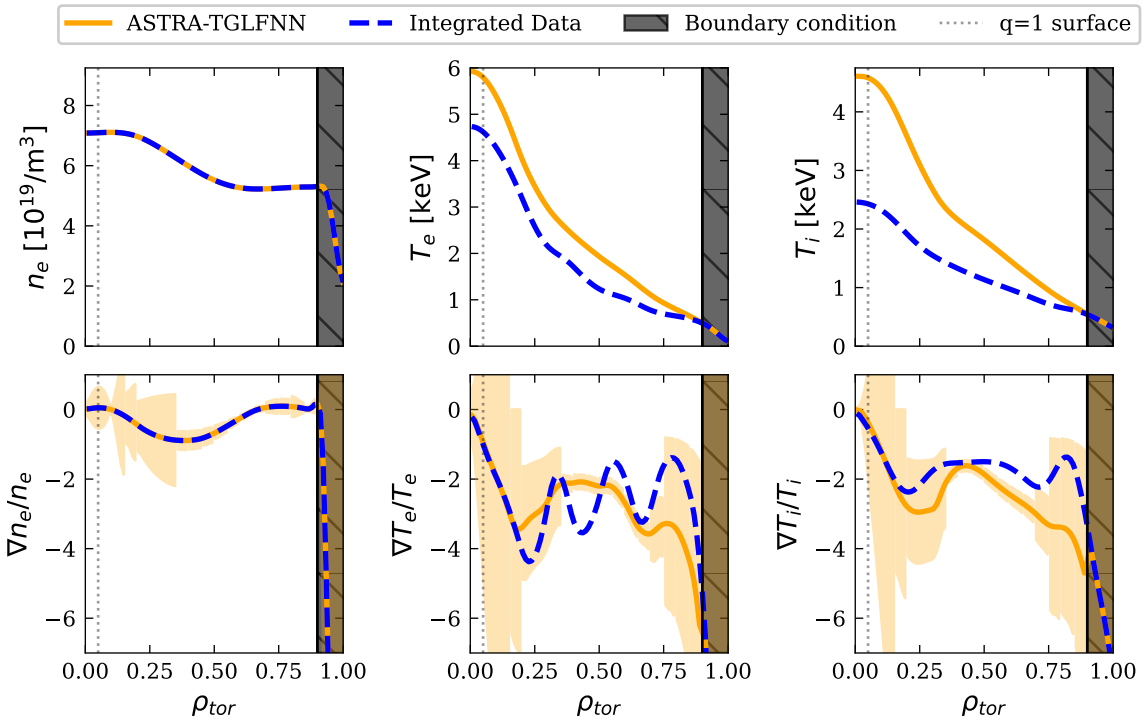

Figure 6.3.: TGLFNN simulation of the H-mode discharge 33616 with the density being kept constant. The neural network is based on TGLF-SAT0. The network struggled to predict discharges, with the best T_e results coming from H-mode discharges with constant density and T_i. Currently, work is being done to update the neural network, which could be interesting to accelerate the kinetic model.

current, as well as the effective charge, could be calculated selfconsistently.

IMEP is an especially interesting option for IDA+KM discharges where the plasma edge is badly resolved due to unavailable lithium beam data. The H-mode discharge #33616 IMEP simulation was compared to IDA and IDA+KM. It was observed that the IMEP profiles and especially its logarithmic gradients match the kinetic model and experimental data nicely. IMEP is thus a viable option for an improved kinetic model. The gradient mismatch at around $\rho_{tor} = 0.2$ is explained by IMEP using different additional transport coefficients to simulate the sawtooth region. The mismatch in density most likely stems from an improvable neutrals model that recycles too few deuterium atoms from the scrape-off layer. In a further update, it is planned to exchange the ideal MHD code MISHKA with the higher-fidelity resistive MHD code CASTOR [163].

As the IMEP simulation takes around 600 ASTRA simulations to find the optimal pedestal, this is not yet a realistic option for standard IDA+KM model. Depending on the use case, one could attempt to first use a neural network turbulence solver to get an approximate solution before moving to higher fidelity. The 600 simulations could at least immediately be used for an input sensitivity analysis. If further input, such as impurity content, were to be tested, these simulations would also have to be made with a lower-fidelity turbulence solver due to computational constraints.

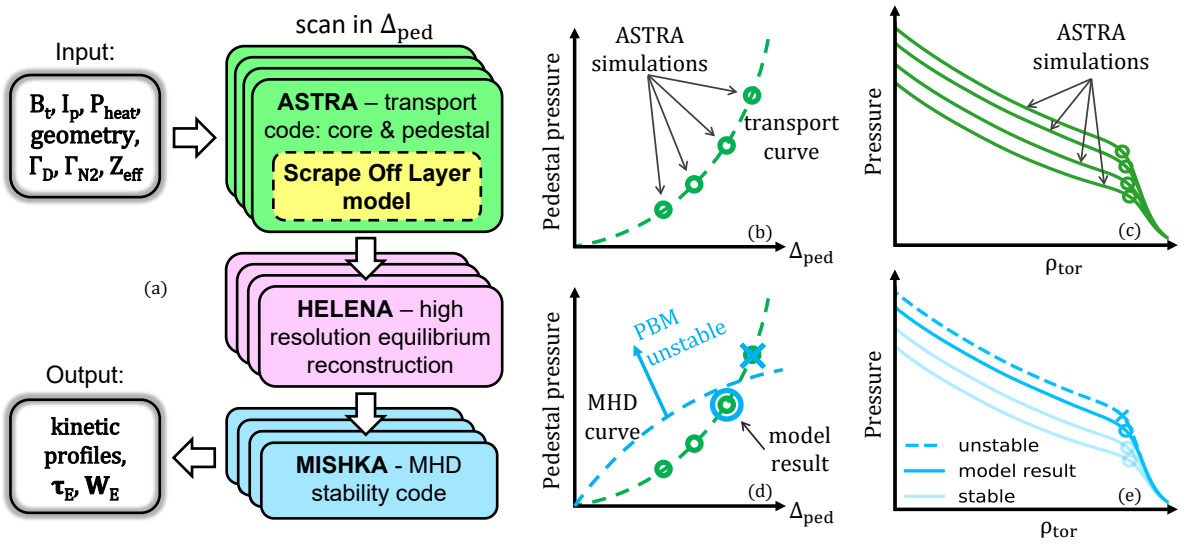

Figure 6.4.: Diagram (a) illustrates the modeling workflow. Multiple parallel ASTRA simulations compute kinetic profiles for varying pedestal width values (c). The integrated pedestal model within ASTRA establishes a transport constraint, determining pedestal pressure based on pedestal width (b). Subsequently, MISHKA assesses profile stability, identifying the maximum sustainable pedestal pressure (d, e). Figure taken from [54].

6.3. IDA+KM for an entire discharge

In the previous cases, IDA+KM was only used to simulate a single time slice. When moving to simulating an entire discharge, several problems arise. For one, many discharges have a changing heating scheme, meaning that ASTRA has to converge faster as it is no longer feasible to let the profile converge after 80 time steps with 25ms per step. This would lead to IDA being fed 2s of unconverged ASTRA-TGLF simulation. Instead, the timesteps of the different subroutines were reduced to 5ms and thus reached convergence with fewer time steps inside the shot as shown in [145]. In the future, a small burn-in period could also be used to ensure convergence from the first step. The downside is, of course, that the simulation takes substantially longer. The simulation below needed approx. 15 hours of wall-clock time. Of these 15 hours, the 16 parallel TGLF transport solvers used up from 10.2h to 13.9h, with a preliminary observation being that the innermost solvers finished quicker. If confirmed, possible speed-ups could be made by redistributing the number of radial points.

In figure 6.6, one can see a L-mode discharge #35475, also analyzed with ASTRA-TGLF in [53], for which the NBI heating was replaced with ERCH in two steps, seen in table 6.1. The most noticeable mismatch between the experiment and simulation is immediately after new ECRH power was added, with the simulated electron temperature lagging behind the measured one. This lag could be solved with an even smaller timestep after a change in heating. For ρ_{tor}=0 it is not entirely clear if the immediate jump of IDA is physical due to a lack of measurement data.

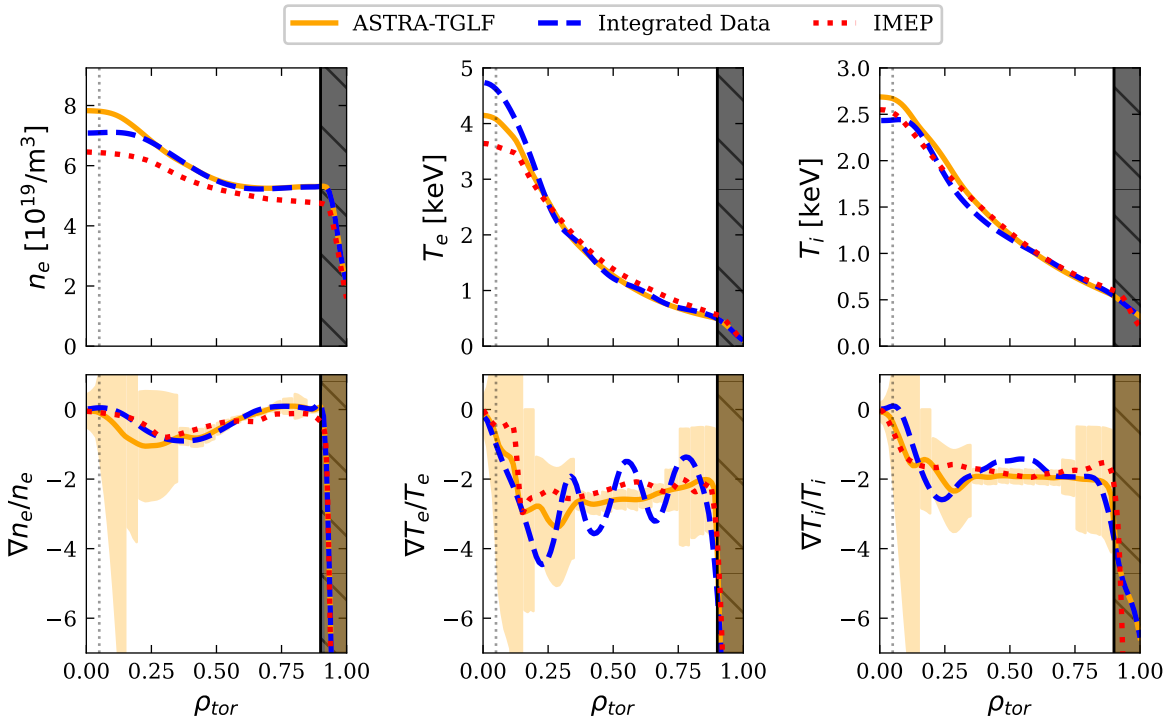

Figure 6.5.: Comparison of the IMEP Framework with ASTRA-TGLF and IDA. IMEP is capable of simulating plasma discharges up to the separatrix without needing input profiles. For this simulation, IMEP was run using the TGLF-SAT1 rule. Due to the pedestal density underprediction, the density is consistently lower than the experiment. The dashed q=1 line is from the ASTRA-TGLF simulation.

Shown in the appendix are the density and ion temperature profiles. T_i is overestimated throughout the discharge due to a too-large gradient close to the boundary condition. After the NBI heating was switched off, the simulation was continued with $T_{i,boundary}$=$T_{e,boundary}$ to counter the lack of CXRS data. This definitely resulted in a further overestimation of T_i as the ion temperature rose with less ion heating. The density is also slightly but consistently overestimated in the main region. Immediately after starting the simulation, the experimental density at the magnetic center rises. The rise in density is not captured by the model, and its cause is unclear. The simulation also uses time-dependent input, meaning that the boundary conditions can move up or down with the experimental data. The equilibrium was recalculated at every step as the q-profile will have changed moving the q=1 surface. This leads to noticeable "wiggles" in the core profiles, which seem to match the experimental values.

The IDA-KM profile is fitted with the ASTRA profile closest to it in the simulated time. In the temperature log gradient profile shown in figure 6.7 and the residuals of the different diagnostics shown in figure 6.8, one can see that the IDA-KM is less prone to the T_e hollowness in the core without negatively impacting the ECE measurements. Overall, the profiles are not negatively influenced except for the density edge measuring H-5 DCN interferometry diagnostic after 5s, when the NBI heating was just turned off. Which could have negatively

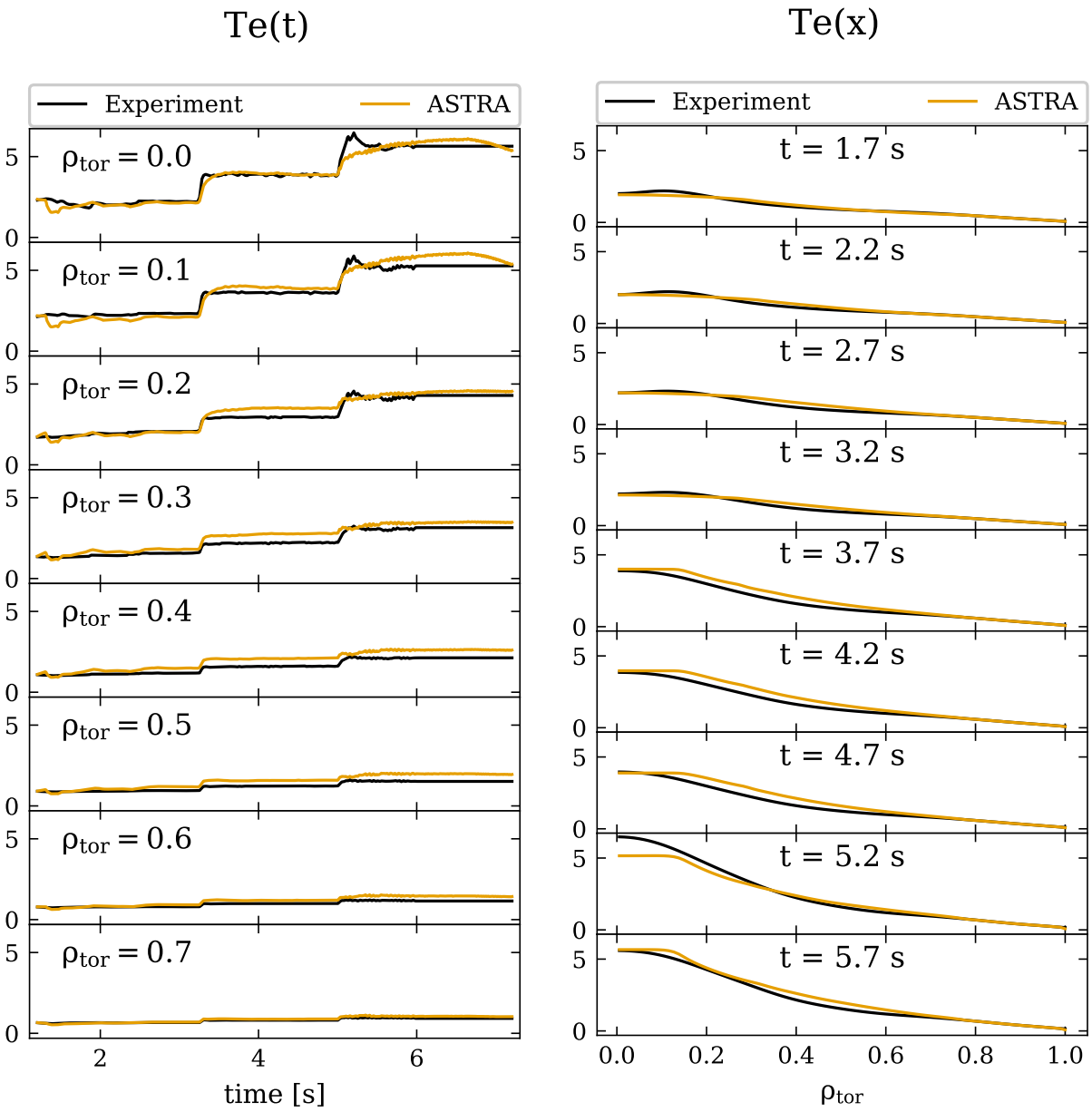

(a) Electron temperature for different selected radii. It is difficult to quantify the mismatch at $\rho_{tor} = 0$ at around 5s as there were no diagnostics at that radius.

(b) Electron temperature for different selected times. Overall the simulation seems to capture the physics.

Figure 6.6.: L-mode discharge #35745 uses different heating powers of both NBI and ECRH during the discharge. This means that the mixture of ITG and TEM also changes as the amount of ion heating decreases step-wise.

time [s]	P_{NBI}[MW]	P_{ECRH}[MW]
1.2-3.2	1.6	0.0
3.2-5.0	0.8	0.7
5.0-6.0	0.0	1.35

Table 6.1.: Heating sources of L-mode discharge #35475 for different timewindows. The discharge was simulated until 7.2s with the input of 6s.

impacted the simulation, or the sudden drop in the particle source is to blame. The sawteeth can be seen as a small jitter in the gradient, which should not be problematic with the large uncertainties used for the kinetic model.

It was observed that increasing the numerical diffusivity and time steps led to a worse match of experiment and simulation. Still, a proper systematic scan is left for future studies.

As more than 20 discharges can be run per day, running these 15h simulations is not necessarily desirable. This thesis presents two main ideas for reducing computational time for IDA+KM. A quick option would be running ASTRA-QLKNN or the formula-based fast transport solver from [164] used in the ASDEX Upgrade flight simulator. In these cases, the biggest time consumers would be the heating subroutines RABBIT and TORBEAM and writing the output to a CDF file. Repeating the discharge from figure 6.6 with ASTRA-QLKNN would take about 45 minutes. Compared to the kinetic modeling prior using ASTRA-TGLF, these cheaper models would require larger uncertainties, with an additional increase in uncertainty if the neural network is extrapolating from its trained input space. A more advanced alternative would be using a multi-fidelity/surrogate model approach, such as used to achieve fast convergence for high-fidelity SPARC simulations in [165, 166].

Maximum gradient limit

An even less exact option for a theory-based prior is to compute the critical gradients from 2.3.3 and use them multiplied with a constant as an upper gradient limit. One would not need heating subroutines, so running ASTRA in interpretative mode with a 5ms time step resolution would need approximately 15min. In figure 6.9 one can see the TEM and ITG critical gradients for the L-mode discharge #36974 compared to the gradients from IDA and the ASTRA-TGLF simulation. Even when computing the gradients with the same simplifications as in the references, e.g. $\frac{d\kappa}{d\epsilon} = (\kappa - 1)/\kappa$, the critical gradients were surprisingly low compared to the gradients simulated by ASTRA-TGLF. The second row shows by what factor IDA and ASTRA-TGLF are larger than the two critical gradients. Outside the q=1 surface at around $\rho_{tor} = 0.4$, the maximum simulated gradient is about three times the TEM critical gradient. The experimental electron log gradient reaches 4.5 times the ECE gap's critical TEM gradient.

In the future, one could scan a database of ASDEX Upgrade simulations and determine an average fraction of the gradients to the critical gradients. Additionally, empirical limits such as the Greenwald-density limit $n_e \leq n_{GW} = 10^{14} m^{-3} \frac{I_p}{\pi a^2}$ [167] (above which the plasma is due to disrupt) or the Troyon limit [168, 13] $\beta_n = \frac{aB_{tor}\beta_{tor,max}[\%]}{I_p}$, where $\beta_{tor,max}[\%] = 2.8\frac{I_p}{aB_{tor}}$ (above which MHD modes are activated) could be incorporated. As these formulas give fairly rough estimates and cannot predict internal transport barriers, this kind of estimate would need very large uncertainties. It is doubtful if using these formulas will lead to a proper upper gradient limit.

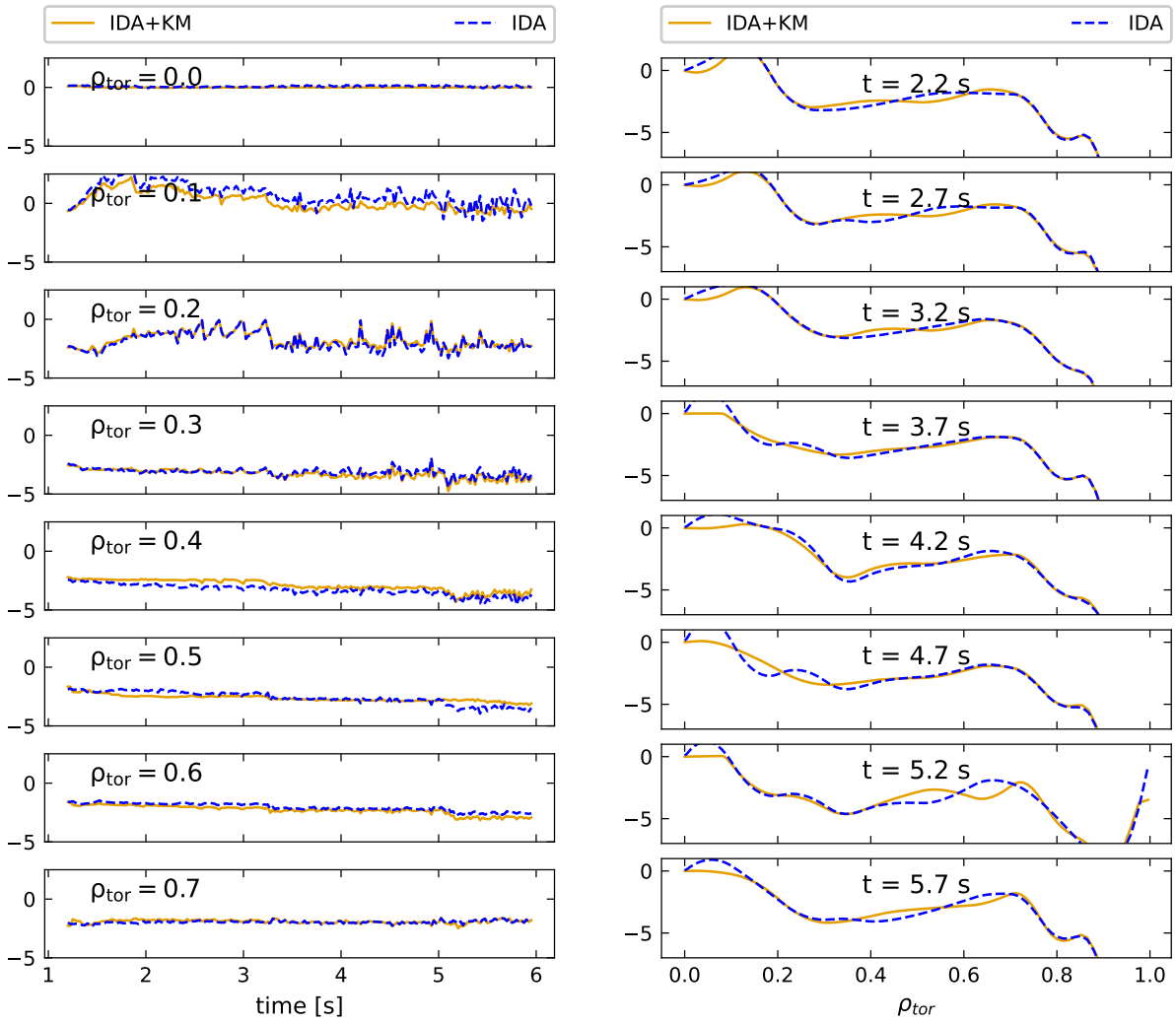

(a) Electron temperature log gradients for different selected radii. The slight hollowness inside ρ_{tor} is seen in the ECE diagnostic. However, the scattering is so large that it could also be an artifact due to some mode activity.

(b) Electron temperature log gradients for different selected times.

Figure 6.7.: L-mode discharge #35745 uses different heating powers of both NBI and ECRH during the discharge. This means that the mixture of ITG and TEM also changes as the amount of ion heating is step-wise decreased.

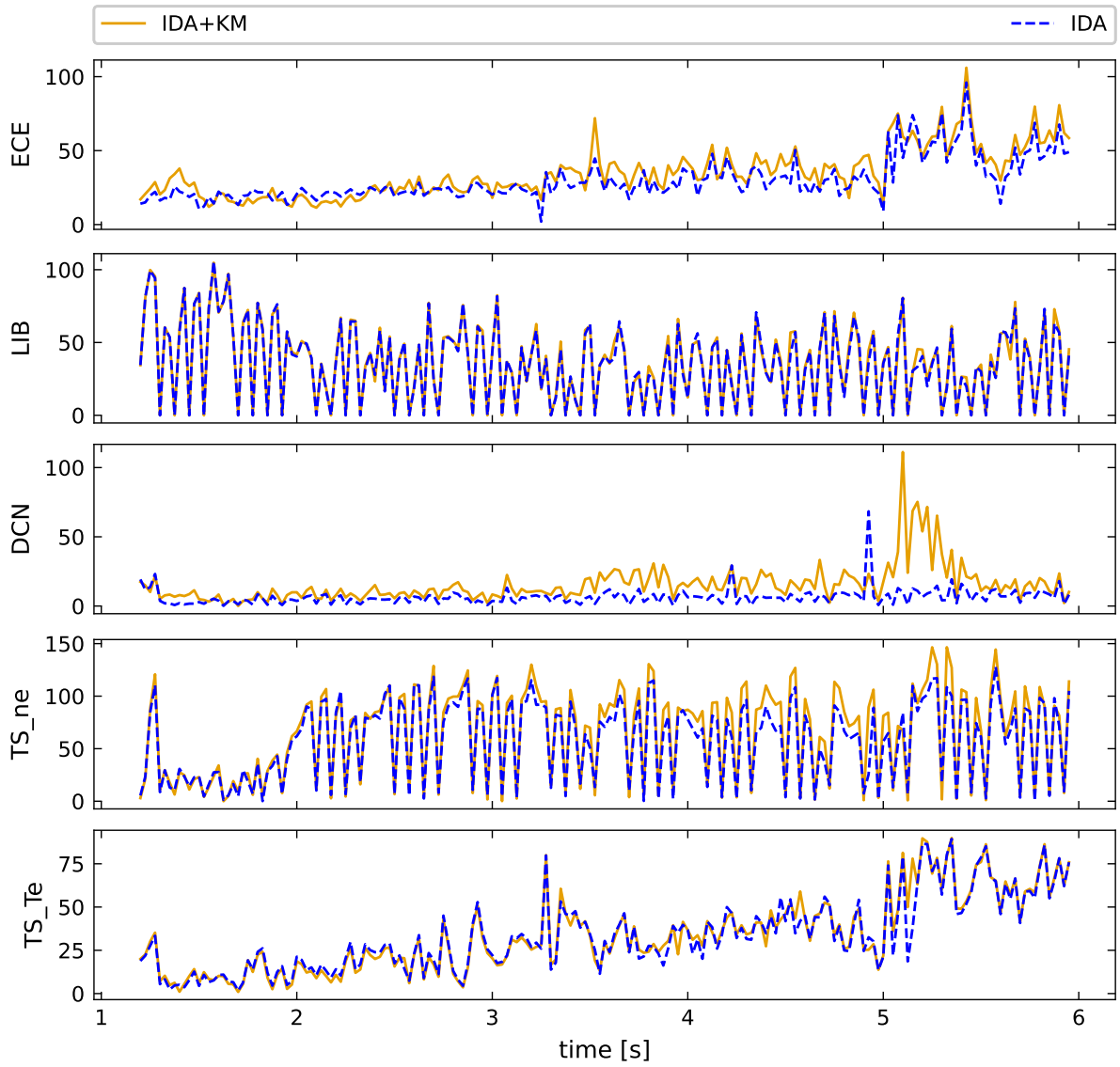

Figure 6.8.: Residual of the different diagnostics over time. The DCN spike after 5s is from the H-5 diagnostic, which measures closer to the edge. A possible explanation is that the NBI was just turned off so that ASTRA-TGLF used $T_i = T_e$ at the boundary condition.

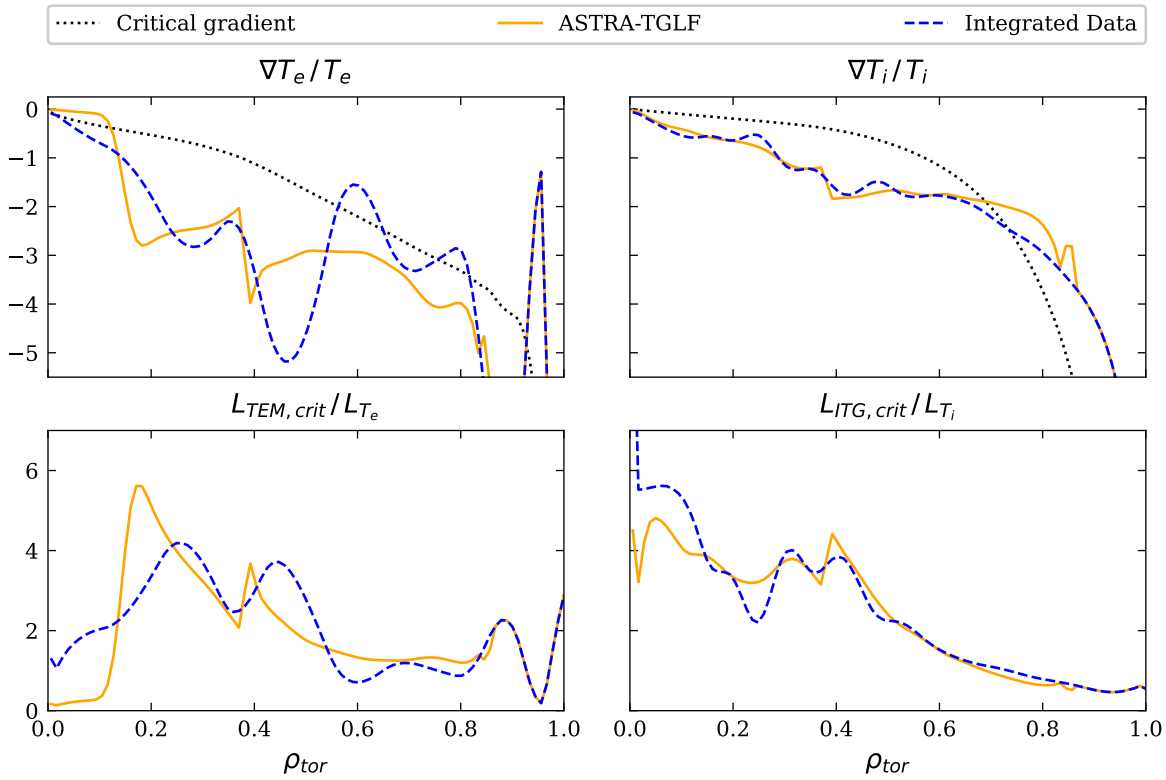

Figure 6.9.: Comparison of critical TEM and ITG critical gradients to the ones calculated from IDA and ASTRA-TGLF. The profiles reach up to 6 times the critical gradients, if similar limits are found for other discharges, then these could be used as upper limits for IDA. However, due to the large differences in heating schemes between discharges, it will be difficult to determine a sensible upper limit.

7. Summary

At ASDEX Upgrade, the plasma community often relies on electron density and temperature profiles from the Integrated Data Analysis framework, which uses Bayesian probability theory to combine diagnostics and well-chosen priors. This thesis found that the plasma profiles stemming from IDA can have strongly fluctuating gradients, especially when measurements are unavailable. These gradients are often at direct odds with theoretical predictions, as they would drive stronger turbulent transport than expected from the power balance. Heat and particle flux stemming from turbulent transport poses a significant constraint in Tokamaks regarding raising the plasma's core temperature and density profiles. IDA has the ability to smoothen profiles with a stronger curvature prior, which would reduce sudden gradient spikes. However, this doesn't necessarily improve the heat flux match and the stronger curvature prior can overrule measurement data.

In this thesis, ASTRA-TGLF simulations were employed as a kinetic modeling prior, which was found to smoothen the gradients of the different profiles. The ASTRA-TGLF simulations are run before the IDA fitting process commences, and the simulation results are weighted as any other diagnostic in IDA. It was found that due to the dominant turbulent transport, comparing the logarithmic gradients of the simulation to the proposed IDA profile led to better results than using the actual profile. This approach was validated by comparing heat and particle fluxes for various L- and H-mode plasma test cases to the power and particle balance. Using this kinetic modeling prior, the matches in standard discharges were found to increase. However, in ITG-dominated plasmas, the heat flux depends so strongly on the ion temperature log gradient that in tested cases, the simulated ion gradient had to be used as input to see improved results. This motivates the implementation of kinetic modeling to IDI in the future.

To ensure that the measurements are prioritized over the kinetic model, the residuals of different diagnostics were assessed, which remained stable under typical scenarios. In discharges that are difficult to model with ASTRA-TGLF, such as discharges with neoclassical tearing modes and internal transport barriers, using a Gaussian likelihood was found to potentially negatively affect the IDA profile. Employing an outlier robust Student's t-distribution instead prevented the kinetic model from adversely affecting the profiles while maintaining positive consequences.

Predefined uncertainties for the kinetic model based on different plasma regions were used for this proof-of-concept work. These were chosen to be large inside the sawtooth region and close to the edge with a minimum of 10% uncertainty at mid-radius. In the future, a more robust uncertainty quantification method will be used. The sensitivity of the

ASTRA-TGLF simulation in regard to the input parameters was examined with a Monte Carlo variation method. The uncertainty at the mid-radius estimation was found to be similar to the predetermined error bars. As Monte Carlo methods need a large number of samples, a further improvement using polynomial chaos expansion was presented.

Furthermore, systematic error sources were scrutinized. Possible adverse effects of how the ASTRA equilibrium solver SPIDER compares to the equilibrium used by IDA were investigated, which found that while the flux surfaces can be shifted, the mapping of ρ_{tor} to ρ_{pol} matches almost completely and should not negatively affect the gradients.

Previous studies in this field have compared fluxes of quasi-linear models with high-fidelity codes turbulence codes at given gradients. This thesis, however, explores how the gradients compare given the flux, which is dependent on the determination of the critical gradients and on how stiff the profiles are. The study was done with over 40 non-linear GENE simulations in which the density gradients were found not to match well, while both Temperature gradients were within 30% .

IDA is a standard profile-generating framework at ASDEX Upgrade. Improving the profile's agreement with simulations can benefit many applications. A use case of achieving faster convergence in GENE flux-matching simulations was highlighted. The IDA+KM's gradients were compared to the best flux-matched GENE non-linear turbulence simulation for 5 L-mode discharges. Encouragingly, the gradients in the IDA+KM model were found to be closer to those predicted by GENE, surpassing the standard IDA results. As the GENE simulations cost several hundreds of thousands of CPU hours, it is imperative to have an optimal starting point. This process allows for the exploration of additional parameters in validation studies. For instance, it is now believed that, for an even more improved match of the turbulence parameters, impurities have to be included in GENE.

While ASTRA-TGLF is an inexpensive code compared to higher fidelity models such as GENE-Tango, it is too computationally expensive to run for an entire discharge for each experiment run at ASDEX Upgrade. After working on implementing the neural network solver of the quasi-linear turbulence model Qualikiz called QLKNN, it is found that the model can give realistic solutions for H-mode discharges while being orders of magnitudes faster. The option of using turbulence solvers intertwined with artificial intelligence will improve further as additional models are implemented in ASTRA. This may entail new neural network solvers trained on TGLF and GENE.

As a very quick alternative to kinetic modeling prior that does not require ASTRA at all, the feasibility of using critical gradient formulas as a maximum limit for IDA profiles was tested. The formulas are based on simplified assumptions, and the critical gradient is routinely crossed by large margins. It is unlikely that using the formulas will have much merit over a fast neural network solver.

Outlook

While this thesis shows encouraging results, several tasks still remain unresolved. This thesis can reduce the amount of time a user needs to invest to obtain profiles for high-fidelity simulations. These time gains could be further improved by metrics that reject a simulation due to the discharge being badly modeled.

Additionally, the uncertainties used to define the likelihood of the ASTRA-TGLF prior should be based on a more solid foundation. In collaboration with the Technical University of Munich, the possibilities of polynomial chaos expansion are being explored to give the user a faster overview of the simulation's uncertainty propagation using trained model surrogates. After implementing PCE, more work must be done to manage discharges for which ASTRA-TGLF cannot capture the physics.

While it has been shown that IDA+KM can be used on an entire discharge, quantifying the uncertainties, for example, stemming from the numerical diffusivities or the heating source ramping up during a change in heating, still needs to be validated. While it is likely that the boundary condition used in the simulations makes simulation fuelling with gas values possible, discharges with pellet injection have not been studied and would need a further expansion of the model.

This thesis has shown the large effect of ion gradients, which motivates further testing simulated gradients for IDI to resolve the consistency issue in ITG-dominated discharges. Ideally, one would combine IDA, IDE, IDI, and IDZ into one optimization structure to utilize the different synergies of all diagnostics employed. This structure could also use kinetic modeling prior's output, as there is recent work in modeling the plasma current and impurities in ASTRA, it could provide a physics-based prior for each fitted quantity. However, this is doubtful to happen promptly, as it would require extensive implementation time.

Work is being done on expanding the GENE-TGLF gradient comparison study while exploring further analysis options with codes such as VITALS. This will enable varying gradients while keeping everything else constant to study systematic effects in more detail. As the physics of the H-mode core should be similar to that of an L-mode discharge, adding H-mode GENE simulations to the database will help minimize the uncertainty of the error quantization.

Acknowledgments

First of all, I would like to thank my academic supervisor Frank Jenko and my direct supervisor Rainer Fischer, for giving me the opportunity to work on this PhD project, their commitment, and always being there when I had a question. Starting the PhD I had almost no experience with either profile reconstruction or turbulence physics and the large strides I made throughout the PhD are a testament to their patience and helpful input. I would also like to thank Rainer for suggesting further opportunities for me to present my work, such as at the IAEA conference in Ghent and for giving me feedback on the new IDA profiles.

I would further like to especially thank Teobaldo Luda, Clemente Angioni, Giovanni Tardini and Emiliano Fable for getting me acquainted with ASTRA and TGLF. There are many different settings possible in the seemingly endless amount of subroutines available in ASTRA and having their feedback saved me from many mistakes. In this regard, I would also like to thank the members of the ASTRA PhD Whatsapp group: Maxi Reisner, Benedikt Zimmermann, Marco Muraca, Christian Schuster, Raphael Stramm, Audrey Saltzmann and Daniel Fajardo.

During the PhD I had the great pleasure of working on several GENE and GENE-Tango validation projects. I would like to thank Klara Höfler, Pedro Molina Cabrera, Tobias Görler, Alessandro Di Siena and Roberto Bilato for the fun and informative collaboration.

I want to thank Hans Bungartz and Tobias Neckel for introducing some uncertainty quantification concepts to me and Kislaya Ravi for developing the polynomial chaos expansion for ASTRA. This collaboration was executed under the *Munich School of Data Science* program, which was effectively organized by Julia Schlehe and Mara Kieke.

When the institute wasn't sent into home office duty during a pandemic, it was invaluable to have an office of bright people to bounce ideas off of, discuss plots and to drink coffee with. I would like to thank Victor Artigues, Hannes Bergström, Andrés Cathey, Hugo Cu Castillo, Constantin Gahr (whom I have to especially thank for developing the python package *latexplotlib* to make the plots for this thesis), Robin Greif, Francisco Matos, Karen Pommois, Peter Halldestam, Sabine Ogier-Collin and Luciana Tanzarella. I would also like to thank the many other physicists who read parts of my thesis or went out of their way to help me, such as Rachel Bielajew, Leonhard Leppin, Daniel Wendler, Dirk Stieglitz, Ulrike Plank, Marion Smedberg, Annika Stier, Jordy Trilaksono and Philipp Ulbl. A special thanks goes to Rebecca Masline, who has been my friend from the first days at DIII-D.

With brief stints in Lausanne and San Diego I have been studying physics in Munich since 2013. In that time, Veronika Pörtge, Bianca Neureiter, Fatos Gaschi, Nina Wenke, Nathalie

Eberlein and Johannes Oberpriller have always been with me and had an open ear for me.

I would like to thank my second family of Andres, Paula and Luna for feeding me throughout the pandemic, keeping me well caffeinated and teaching me too many Cocomelon songs.

Finally, I would like to thank my family (Tony, Annette, Zausi and Princi) and my girlfriend Seti, for always loving me and listening to me. There will always be stress when handing in a project of four years, and I look forward to supporting you with your challenges in the coming months as you have supported me.

A. General Addenda

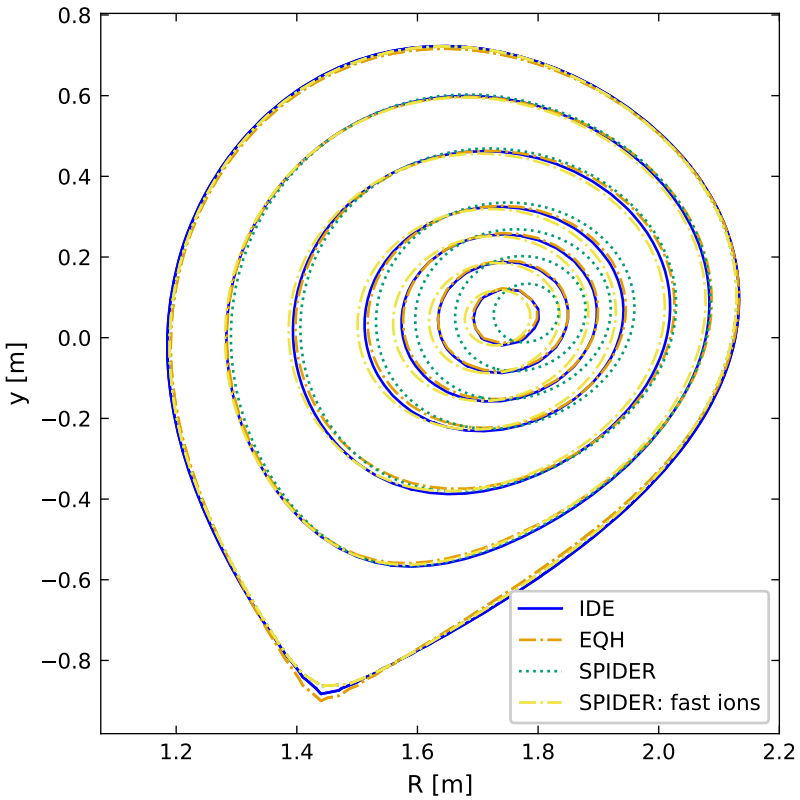

Figure A.1.: Equilibria for an ITB discharge #39230 at 2.73s. The spider solvers were used in an ASTRA interpretive mode simulation, meaning that the profiles matched the experimental data. When including fast particles, the Shafranov-shift in the ITB region is too strong.

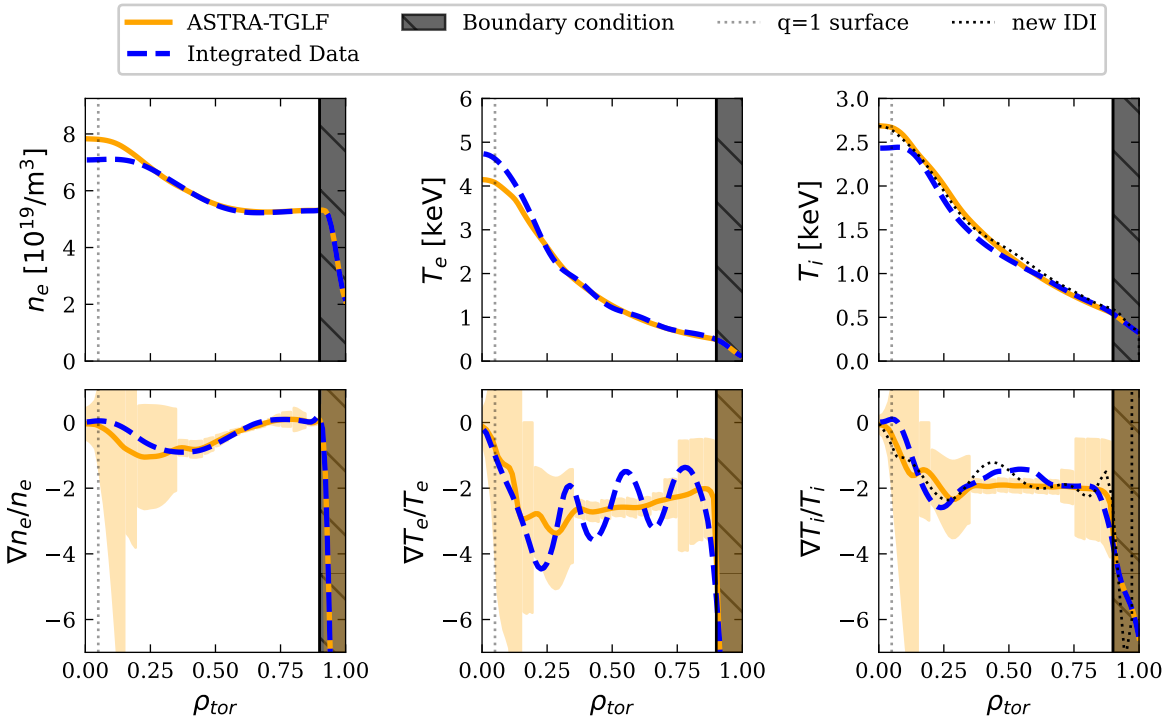

Figure A.2.: Simulation of H-mode discharge #33616 with an additional IDI profile plotted, which nicely matches the simulation. The new IDI profile uses the newest version of IDI as well as the IDE equilibrium.

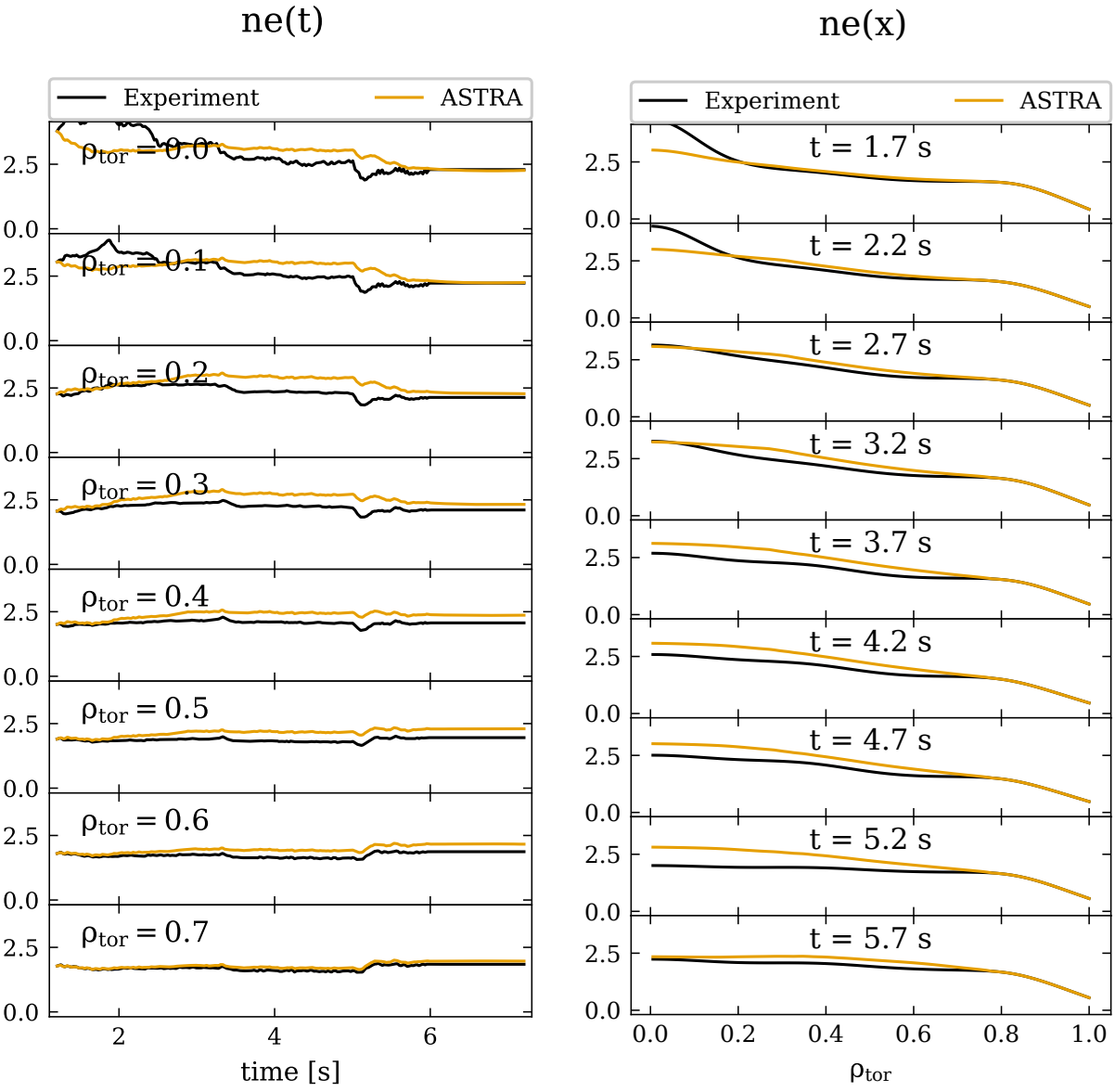

(a) Electron density for different selected radii. It is difficult to quantify the mismatch at $\rho_{tor} = 0$ early in the simulation where the density suddenly rises.

(b) Electron density for different selected times. The largest mismatch is immediately after the NBI is turned off at 5s.

Figure A.3.: L-mode discharge #35745 uses different heating powers of both NBI and ECRH during the discharge. This means that the mixture of ITG and TEM also changes as the amount of ion heating decreases step-wise.

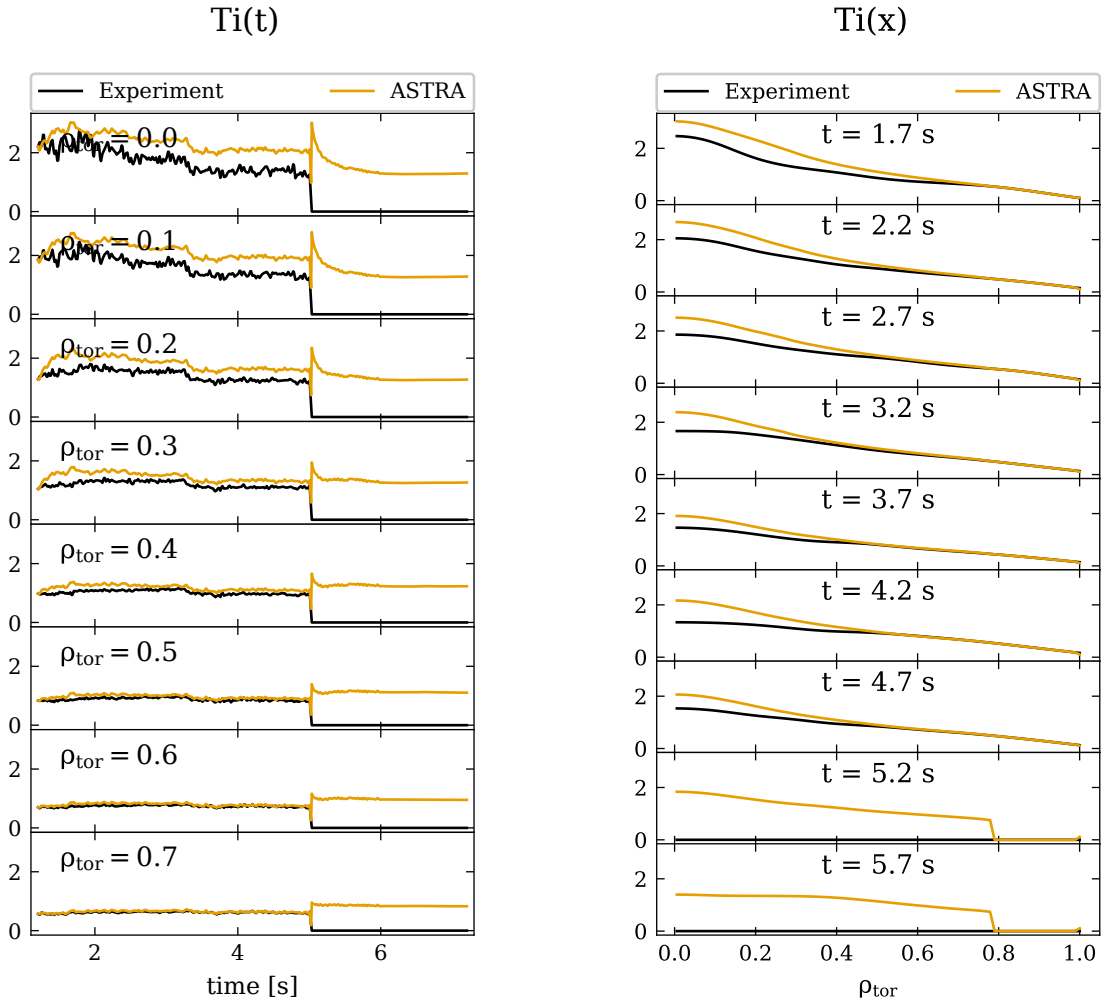

(a) Ion temperature for different selected radii. After 5s the ion temperature boundary is based on the electron temperature.

(b) Ion temperature for different selected times. The core is consistently overpredicted.

Figure A.4.: L-mode discharge #35745 uses different heating powers of both NBI and ECRH during the discharge. This means that the mixture of ITG and TEM also changes as the amount of ion heating decreases step-wise.

List of Figures

List of Tables

Acronyms

BPT Bayesian probability theory. 6

ECRH Electron cyclotron resonant heating. 39

ETB Edge transport barrier. 20

ETG Electron temperature gradient. 16

ICF inertial confinement fusion. 3

ICRH Ion cyclotron resonant heating. 39

IDA Integrated Data Analysis. d, 6

ITB Internal transport barrier. 21, 68, 108, 119

ITG Ion temperature gradient. 16

KM kinetic model. 8

MCF magnetically confined fusion. 3

MCMC Markov Chain Monte Carlo. 53

MHD Magnetohydrodynamics. 10

NBI Neutral beam injection. 39

NTM Neoclassical Tearing mode. 25

PCE Polynomial chaos expansion. 59, 61

pdf probability distribution function. 45, 46

RMS Root Mean Square. 34

TEM trapped electron mode. 16, 99

Bibliography

[1] *Nuclear power: Too expensive and inefficient?* https://www.dw.com/en/nuclear-climate-mycle-schneider-renewables-fukushima/a-56712368. Accessed: 2023-04-25.

[2] csm.jmu.edu/physics/courses/163/older/bepn2.jpg. Accessed: 2018-10-29.

[3] J. Freidberg. "Plasma Physics and Fusion Energy.-Cambridge University Press". In: *New York* (2007).

[4] M. Zucchetti, L. El-Guebaly, R. Forrest, T. Marshall, N. Taylor, and K. Tobita. "The feasibility of recycling and clearance of active materials from fusion power plants". In: *Journal of Nuclear Materials* 367 (2007), pp. 1355–1360.

[5] J. Lawson. "Some Criteria for a Useful Thermonuclear Reactor". In: ().

[6] *National Ignition Facility achieves fusion ignition*. https://www.llnl.gov/news/national-ignition-facility-achieves-fusion-ignition. Accessed: 2023-04-25.

[7] S. E. Wurzel and S. C. Hsu. "Progress toward fusion energy breakeven and gain as measured against the Lawson criterion". In: *Physics of Plasmas* 29.6 (2022).

[8] E. ITER et al. "Overview and summary". In: *Nuclear Fusion* 39.12 ITER physics basis (1999), pp. 2137–2174.

[9] A. Creely, M. J. Greenwald, S. B. Ballinger, D. Brunner, J. Canik, J. Doody, T. Fülöp, D. Garnier, R. Granetz, T. Gray, et al. "Overview of the SPARC tokamak". In: *Journal of Plasma Physics* 86.5 (2020), p. 865860502.

[10] X. Hao. "Radial magnetic field in magnetic confinement device". In: ().

[11] U. Stroth. *Plasmaphysik*. 2018.

[12] H. Zohm. *Magnetohydrodynamic Stability of Tokamaks* -. New York: John Wiley, 2014. ISBN: 978-3-527-67736-8.

[13] H. Zohm. *Magnetohydrodynamic stability of tokamaks*. John Wiley & Sons, 2015.

[14] O. Sauter, M. A. Henderson, F. Hofmann, T. Goodman, S. Alberti, C. Angioni, K. Appert, R. Behn, P. Blanchard, P. Bosshard, R. Chavan, S. Coda, B. P. Duval, D. Fasel, A. Favre, I. Furno, P. Gorgerat, J.-P. Hogge, P.-F. Isoz, B. Joye, P. Lavanchy, J. B. Lister, X. Llobet, J.-C. Magnin, P. Mandrin, A. Manini, B. Marlétaz, P. Marmillod, Y. Martin, J.-M. Mayor, A. A. Martynov, J. Mlynar, J.-M. Moret, C. Nieswand, P. Nikkola, P. Paris, A. Perez, Z. A. Pietrzyk, R. A. Pitts, A. Pochelon, G. Pochon, A. Refke, H. Reimerdes, J. Rommers, E. Scavino, G. Tonetti, M. Q. Tran, F. Troyon, and H. Weisen. "Steady-State Fully Noninductive Current Driven by Electron Cyclotron Waves in a Magnetically Confined Plasma". In: *Phys. Rev. Lett.* 84 (15 2000), pp. 3322–3325.

DOI: 10.1103/PhysRevLett.84.3322. URL: https://link.aps.org/doi/10.1103/PhysRevLett.84.3322.

[15] Max Planck Institute for Plasma Physics. *Magnet System of a Tokamak Fusion Device*. https://www.ipp.mpg.de/14869/tokamak. Accessed: April 29, 2019. 2019.

[16] R. Fischer, C. Fuchs, B. Kurzan, W. Suttrop, E. Wolfrum, and A. U. Team. "Integrated data analysis of profile diagnostics at ASDEX Upgrade". In: *Fusion science and technology* 58.2 (2010), pp. 675–684.

[17] W. Biel, M. Ariola, I. Bolshakova, K. Brunner, M. Cecconello, I. Duran, T. Franke, L. Giacomelli, L. Giannone, F. Janky, et al. "Development of a concept and basis for the DEMO diagnostic and control system". In: *Fusion engineering and design* 179 (2022), p. 113122.

[18] F. Wagner, G. Becker, K. Behringer, D. Campbell, A. Eberhagen, W. Engelhardt, G. Fussmann, O. Gehre, J. Gernhardt, G. v. Gierke, et al. "Regime of improved confinement and high beta in neutral-beam-heated divertor discharges of the ASDEX tokamak". In: *Physical Review Letters* 49.19 (1982), p. 1408.

[19] G. V. Pereverzev and P. Yushmanov. "ASTRA. Automated System for TRansport Analysis in a tokamak". In: Max-Planck-Institut für Plasmaphysik, 2002.

[20] G. M. Staebler, N. T. Howard, J. Candy, and C. Holland. "A model of the saturation of coupled electron and ion scale gyrokinetic turbulence". In: *Nuclear Fusion* 57.6 (2017), p. 066046.

[21] M. Reisner. "Dependence of transport in high-beta low collisional H-modes on ExB-shear and q-profile". In: (2022).

[22] F. Jenko, W. Dorland, M. Kotschenreuther, and B. Rogers. "Electron temperature gradient driven turbulence". In: *Physics of plasmas* 7.5 (2000), pp. 1904–1910.

[23] R. H. Kraichnan. "Inertial ranges in two-dimensional turbulence". In: *The Physics of Fluids* 10.7 (1967), pp. 1417–1423.

[24] P. Manz. *The microscopic picture of plasma edge turbulence*. 2018.

[25] A. Zeiler. "Tokamak edge turbulence". In: (1999).

[26] A. Bock. "Generation and analysis of plasmas with centrally reduced helicity in full-tungsten ASDEX Upgrade". In: (2016).

[27] L. Landau and D. ter Haar. "61–On the vibrations of the electronic plasma". In: *The Collected Papers of LD Landau* (1965), pp. 445–460.

[28] J. Conner and H. Wilson. "Survey of theories of anomalous transport". In: *Plasma physics and controlled fusion* 36.5 (1994), p. 719.

[29] G. Staebler, J. Kinsey, and R. Waltz. "A theory-based transport model with comprehensive physics". In: *Physics of Plasmas* 14.5 (2007), p. 055909.

[30] O. Meneghini, S. Smith, L. Lao, O. Izacard, Q. Ren, J. Park, J. Candy, Z. Wang, C. Luna, V. Izzo, B. Grierson, P. Snyder, C. Holland, J. Penna, G. Lu, P. Raum, A. McCubbin, D. Orlov, E. Belli, N. Ferraro, R. Prater, T. Osborne, A. Turnbull, and G. Staebler. "Integrated modeling applications for tokamak experiments with OMFIT". In: *Nuclear Fusion* 55.8 (2015), p. 083008. URL: http://iopscience.iop.org/article/10.1088/0029-5515/55/8/083008/meta.

[31] F. Jenko, W. Dorland, and G. W. Hammett. "Critical gradient formula for toroidal electron temperature gradient modes". In: *Physics of Plasmas* 8.9 (Sept. 2001), pp. 4096–4104. ISSN: 1070-664X. DOI: 10.1063/1.1391261. eprint: https://pubs.aip.org/aip/pop/article-pdf/8/9/4096/12763930/4096_1_online.pdf. URL: https://doi.org/10.1063/1.1391261.

[32] A. Peeters, C. Angioni, M. Apostoliceanu, F. Jenko, F. Ryter, et al. "Linear gyrokinetic stability calculations of electron heat dominated plasmas in ASDEX Upgrade". In: *Physics of Plasmas* 12.2 (2005).

[33] A. M. Dimits, G. Bateman, M. Beer, B. Cohen, W. Dorland, G. Hammett, C. Kim, J. Kinsey, M. Kotschenreuther, A. Kritz, et al. "Comparisons and physics basis of tokamak transport models and turbulence simulations". In: *Physics of Plasmas* 7.3 (2000), pp. 969–983.

[34] U. Plank, D. Brida, G. Conway, T. Happel, P. Hennequin, A. Hubbard, H. Meyer, T. Pütterich, C. Angioni, M. Cavedon, et al. "Experimental study of the role of the edge radial electric field on the access to H-mode at ASDEX Upgrade". In: *APS Division of Plasma Physics Meeting Abstracts*. Vol. 2021. 2021, TI02–006.

[35] U. Plank. "The effect of the radial electric field around the separatrix on the access to the high confinement mode at ASDEX Upgrade". PhD thesis. Ludwig-Maximilians-Universität München München, 2022.

[36] A. Cathey, M. Hoelzl, K. Lackner, G. Huijsmans, M. Dunne, E. Wolfrum, S. Pamela, F. Orain, S. Günter, J. team, et al. "Non-linear extended MHD simulations of type-I edge localised mode cycles in ASDEX Upgrade and their underlying triggering mechanism". In: *Nuclear Fusion* 60.12 (2020), p. 124007.

[37] P. Manz, M. Ramisch, and U. Stroth. "Physical mechanism behind zonal-flow generation in drift-wave turbulence". In: *Physical review letters* 103.16 (2009), p. 165004.

[38] K. Burrell. "Effects of E× B velocity shear and magnetic shear on turbulence and transport in magnetic confinement devices". In: *Physics of Plasmas* 4.5 (1997), pp. 1499–1518.

[39] T. Antonsen Jr, J. Drake, P. Guzdar, A. Hassam, Y. Lau, C. Liu, and S. Novakovskii. "Physical mechanism of enhanced stability from negative shear in tokamaks: Implications for edge transport and the L-H transition". In: *Physics of Plasmas* 3.6 (1996), pp. 2221–2223.

[40] E. Joffrin, C. Challis, G. Conway, X. Garbet, A. Gude, S. Günter, N. Hawkes, T. Hender, D. Howell, G. Huysmans, et al. "Internal transport barrier triggering by rational magnetic flux surfaces in tokamaks". In: *Nuclear fusion* 43.10 (2003), p. 1167.

[41] G. Tardini, J. Hobirk, V. Igochine, C. Maggi, P. Martin, D. McCune, A. Peeters, A. Sips, A. Stäbler, J. Stober, and the ASDEX Upgrade Team. "Thermal ions dilution and ITG suppression in ASDEX Upgrade ion ITBs". In: *Nuclear Fusion* 47.4 (2007), p. 280. DOI: 10.1088/0029-5515/47/4/006. URL: https://dx.doi.org/10.1088/0029-5515/47/4/006.

[42] A. Di Siena, T. Görler, E. Poli, A. B. Navarro, A. Biancalani, R. Bilato, N. Bonanomi, I. Novikau, F. Vannini, and F. Jenko. "Nonlinear electromagnetic interplay between fast ions and ion-temperature-gradient plasma turbulence". In: *Journal of Plasma Physics* 87.2 (2021), p. 555870201.

[43] A. Di Siena, R. Bilato, A. Banon Navarro, M. Bergmann, L. Leppin, T. Goerler, E. Poli, M. Weiland, G. Tardini, F. Jenko, ASDEX Upgrade Team, and EUROfusion MST1 Team. "Impact of supra-thermal particles on plasma performances at ASDEX Upgrade with GENE-Tango simulations". In: *Nuclear Fusion* (). To be submitted.

[44] V. Igochine, O. Dumbrajs, H. Zohm, A. Flaws, A. U. Team, et al. "Stochastic sawtooth reconnection in ASDEX Upgrade". In: *Nuclear Fusion* 47.1 (2006), p. 23.

[45] H. Azam, B.-X. Gao, W.-D. Liu, J.-L. Xie, E. Team, et al. "Electron cyclotron emission imaging observations of m/n= 1/1 and higher harmonic modes during sawtooth oscillation in ICRF heating plasma on EAST". In: *Chinese Physics Letters* 32.6 (2015), p. 065201.

[46] O. Samoylov. "Magnetic reconnection during sawtooth instability in ASDEX Upgrade". PhD thesis. lmu, 2022.

[47] M. Brüdgam. "Nonlinear effects of energetic particle driven instabilities in tokamaks". In: (2010).

[48] E. Fable, C. Angioni, F. Casson, D. Told, A. Ivanov, F. Jenko, R. McDermott, S. Y. Medvedev, G. Pereverzev, F. Ryter, et al. "Novel free-boundary equilibrium and transport solver with theory-based models and its validation against ASDEX Upgrade current ramp scenarios". In: *Plasma Physics and Controlled Fusion* 55.12 (2013), p. 124028.

[49] F. L. Hinton and R. D. Hazeltine. "Theory of plasma transport in toroidal confinement systems". In: *Rev. Mod. Phys.* 48 (2 1976), pp. 239–308. DOI: 10.1103/RevModPhys.48.239. URL: https://link.aps.org/doi/10.1103/RevModPhys.48.239.

[50] A. Ivanov, R. Khayrutdinov, S. Y. Medvedev, Y. Y. Poshekhonov, et al. "New adaptive grid plasma evolution code SPIDER". In: *Proceedings of 32nd EPS Conference on Plasma Phys., Tarragona, 27 June–1 July 2005 ECA*. Vol. 29. Citeseer. 2005, pp. 5–063.

[51] *TRVIEW by G. Tardini*. https://www.aug.ipp.mpg.de/aug/manuals/transp/trview/index.html. Accessed: 2022-05-12.

[52] W. Houlberg, K.-C. Shaing, S. Hirshman, and M. Zarnstorff. "Bootstrap current and neoclassical transport in tokamaks of arbitrary collisionality and aspect ratio". In: *Physics of Plasmas* 4.9 (1997), pp. 3230–3242.

[53] C. Angioni, T. Gamot, G. Tardini, E. Fable, T. Luda, N. Bonanomi, C. Kiefer, G. Staebler, E. M. Team, et al. "Confinement properties of L-mode plasmas in ASDEX Upgrade and full-radius predictions of the TGLF transport model". In: *Nuclear Fusion* 62.6 (2022), p. 066015.

[54] T. Luda di Cortemiglia, C. Angioni, M. Dunne, E. Fable, A. Kallenbach, N. Bonanomi, P. Schneider, M. Siccinio, G. Tardini, A. U. Team, et al. *Integrated modeling of ASDEX Upgrade plasmas combining core, pedestal and scrape-off layer physics*. 2020.

[55] C. Schuster. "Influence of Fuelling on Transport in the Tokamak Edge Plasma". PhD thesis. Technische Universität München, 2023.

[56] R. Schramm, A. Bock, M. Reisner, E. Fable, J. Stober, M. Maraschek, H. Zohm, A.-U. Team, et al. "Model based optimization of Advanced Tokamak plasma start-up". In: *APS Division of Plasma Physics Meeting Abstracts*. Vol. 2021. 2021, UO07–012.

[57] B. B. Kadomtsev. "Disruptive instability in tokamaks". In: *Sov. Tech. Phys. Lett.(Engl. Transl.);(United States)* 1.5 (1975).

[58] M. Weiland, R. Bilato, R. Dux, B. Geiger, A. Lebschy, F. Felici, R. Fischer, D. Rittich, M. Van Zeeland, E. M. Team, et al. "RABBIT: Real-time simulation of the NBI fast-ion distribution". In: *Nuclear Fusion* 58.8 (2018), p. 082032.

[59] E. Poli, A. Bock, M. Lochbrunner, O. Maj, M. Reich, A. Snicker, A. Stegmeir, F. Volpe, N. Bertelli, R. Bilato, G. Conway, D. Farina, F. Felici, L. Figini, R. Fischer, C. Galperti, T. Happel, Y. Lin-Liu, N. Marushchenko, U. Mszanowski, F. Poli, J. Stober, E. Westerhof, R. Zille, A. Peeters, and G. Pereverzev. "TORBEAM 2.0, a paraxial beam tracing code for electron-cyclotron beams in fusion plasmas for extended physics applications". In: *Computer Physics Communications* 225 (2018), pp. 36–46. ISSN: 0010-4655. DOI: https://doi.org/10.1016/j.cpc.2017.12.018. URL: https://www.sciencedirect.com/science/article/pii/S001046551730423X.

[60] T. Pütterich, R. Neu, R. Dux, A. Whiteford, M. O'Mullane, t. ASDEX Upgrade Team, et al. "Modelling of measured tungsten spectra from ASDEX Upgrade and predictions for ITER". In: *Plasma Physics and Controlled Fusion* 50.8 (2008), p. 085016.

[61] A. Di Siena, A. B. Navarro, T. Luda, G. Merlo, M. Bergmann, L. Leppin, T. Görler, J. Parker, L. LoDestro, T. Dannert, et al. "Global gyrokinetic simulations of ASDEX Upgrade up to the transport timescale with GENE–Tango". In: *Nuclear Fusion* 62.10 (2022), p. 106025.

[62] M. Reisner, E. Fable, J. Stober, A. Bock, A. B. Navarro, A. Di Siena, R. Fischer, V. Bobkov, R. McDermott, et al. "Increased core ion temperatures in high-beta advanced scenarios in ASDEX upgrade". In: *Nuclear Fusion* 60.8 (2020), p. 082005.

[63] A. Bock, E. Fable, R. Fischer, M. Reich, D. Rittich, J. Stober, M. Bernert, A. Burckhart, H. Doerk, M. Dunne, et al. "Non-inductive improved H-mode operation at ASDEX Upgrade". In: *Nuclear Fusion* 57.12 (2017), p. 126041.

[64] P. De Vries, M. Johnson, B. Alper, P. Buratti, T. Hender, H. Koslowski, V. Riccardo, J.-E. Contributors, et al. "Survey of disruption causes at JET". In: *Nuclear fusion* 51.5 (2011), p. 053018.

[65] J. Citrin, J. Garcia, T. Görler, F. Jenko, P. Mantica, D. Told, C. Bourdelle, D. Hatch, G. Hogeweij, T. Johnson, et al. "Electromagnetic stabilization of tokamak microturbulence in a high-β regime". In: *Plasma Physics and Controlled Fusion* 57.1 (2014), p. 014032.

[66] T. Görler, A. White, D. Told, F. Jenko, C. Holland, and T. Rhodes. "A flux-matched gyrokinetic analysis of DIII-D L-mode turbulence". In: *Physics of Plasmas* 21.12 (2014).

[67] A. Bañón Navarro, B. Teaca, F. Jenko, G. Hammett, T. Happel, A. U. Team, et al. "Applications of large eddy simulation methods to gyrokinetic turbulence". In: *Physics of Plasmas* 21.3 (2014).

[68] T. Görler. "Multiscale Effects in Plasma Microturbulence". PhD thesis. Universität Ulm, 2010.

[69] A. J. Brizard and T. S. Hahm. "Foundations of nonlinear gyrokinetic theory". In: *Reviews of modern physics* 79.2 (2007), p. 421.

[70] D. Michels, P. Ulbl, W. Zholobenko, T. Body, A. Stegmeir, T. Eich, M. Griener, G. D. Conway, F. Jenko, and A. U. Team. "Full-f electromagnetic gyrokinetic turbulence simulations of the edge and scrape-off layer of ASDEX Upgrade with GENE-X". In: *Physics of Plasmas* 29.3 (Mar. 2022), p. 032307. ISSN: 1070-664X. DOI: 10.1063/5.0082413. eprint: https://pubs.aip.org/aip/pop/article-pdf/doi/10.1063/5.0082413/16719677/032307_1_online.pdf. URL: https://doi.org/10.1063/5.0082413.

[71] F. Wilms, A. B. Navarro, G. Merlo, L. Leppin, T. Görler, T. Dannert, F. Hindenlang, and F. Jenko. "Global electromagnetic turbulence simulations of W7-X-like plasmas with GENE-3D". In: *Journal of Plasma Physics* 87.6 (2021), p. 905870604. DOI: 10.1017/S0022377821001082.

[72] G. Staebler, J. Kinsey, and R. Waltz. "Gyro-Landau fluid equations for trapped and passing particles". In: *Physics of Plasmas* 12.10 (2005).

[73] T. M. Antonsen Jr and B. Lane. "Kinetic equations for low frequency instabilities in inhomogeneous plasmas". In: *The Physics of Fluids* 23.6 (1980), pp. 1205–1214.

[74] C. Angioni and A. Peeters. "Gyrokinetic calculations of diffusive and convective transport of α particles with a slowing-down distribution function". In: *Physics of Plasmas* 15.5 (2008).

[75] M. Kotschenreuther, G. Rewoldt, and W. Tang. "Comparison of initial value and eigenvalue codes for kinetic toroidal plasma instabilities". In: *Computer Physics Communications* 88.2-3 (1995), pp. 128–140.

[76] G. Staebler, J. Kinsey, and R. Waltz. *Extending the Trapped Gyro-Landau Fluid Equations to General Geometry with Electromagnetic and Collision Terms*. 2006.

[77] S. Freethy, T. Görler, A. Creely, G. Conway, S. Denk, T. Happel, C. Koenen, P. Hennequin, A. White, and A. U. Team. "Validation of gyrokinetic simulations with measurements of electron temperature fluctuations and density-temperature phase angles on ASDEX Upgrade". In: *Physics of Plasmas* 25.5 (2018), p. 055903.

[78] D. Told, F. Jenko, T. Görler, F. Casson, E. Fable, A. U. Team, et al. "Characterizing turbulent transport in ASDEX Upgrade L-mode plasmas via nonlinear gyrokinetic simulations". In: *Physics of Plasmas* 20.12 (2013).

[79] P. Rodriguez Fernandez et al. "Perturbative transport experiments and time-dependent modeling in Alcator C-Mod and DIII-D". PhD thesis. Massachusetts Institute of Technology, 2019.

[80] D. W. Ross. "On standard forms for transport equations and quasilinear fluxes". In: *Plasma Physics and Controlled Fusion* 34.2 (1992), p. 137. DOI: 10.1088/0741-3335/34/2/001. URL: https://dx.doi.org/10.1088/0741-3335/34/2/001.

[81] J. Kinsey et al. "First Transport Code Simulations Using The TGLF Model". In: *Bulletin of the American Physical Society* 52 (2007).

[82] GA-Fusion. *Alphabetical list for input.tglf*. [Online; accessed 03-July-2023]. 2022. URL: https://gafusion.github.io/doc/tglf/tglf_list.html#tglf-kygrid-model.

[83] J. Candy, E. A. Belli, and R. Bravenec. "A high-accuracy Eulerian gyrokinetic solver for collisional plasmas". In: *Journal of Computational Physics* 324 (2016), pp. 73–93.

[84] G. Staebler, E. A. Belli, J. Candy, J. Kinsey, H. Dudding, and B. Patel. "Verification of a quasi-linear model for gyrokinetic turbulent transport". In: 61.11 (2021), p. 116007. DOI: 10.1088/1741-4326/ac243a. URL: https://doi.org/10.1088/1741-4326/ac243a.

[85] G. M. Staebler, J. Candy, N. T. Howard, and C. Holland. "The role of zonal flows in the saturation of multi-scale gyrokinetic turbulence". In: *Physics of Plasmas* 23.6 (2016).

[86] P. Mantica, N. Bonanomi, A. Mariani, P. Carvalho, E. Delabie, J. Garcia, N. Hawkes, T. Johnson, D. Keeling, M. Sertoli, et al. "The role of electron-scale turbulence in the JET tokamak: experiments and modelling". In: *Nuclear Fusion* 61.9 (2021), p. 096014.

[87] M. Cabrera, P. Rodriguez-Fernandez, T. Görler, M. Bergmann, K. Höfler, S. Denk, R. Bielajew, G. Conway, C. Yoo, A. White, et al. "Isotope effects on energy transport in the core of ASDEX-Upgrade tokamak plasmas: Turbulence measurements and model validation". In: *Physics of Plasmas* 30.8 (2023).

[88] P. Rodriguez-Fernandez, A. E. White, A. J. Creely, M. J. Greenwald, N. T. Howard, F. Sciortino, and J. C. Wright. "VITALS: A Surrogate-Based Optimization Framework for the Accelerated Validation of Plasma Transport Codes". In: *Fusion Science and Technology* 74.1-2 (2018), pp. 65–76. DOI: 10.1080/15361055.2017.1396166. eprint: https://doi.org/10.1080/15361055.2017.1396166. URL: https://doi.org/10.1080/15361055.2017.1396166.

[89] C. Angioni, N. Bonanomi, E. Fable, P. A. Schneider, G. Tardini, T. Luda, G. M. Staebler, A. U. Team, et al. "The dependence of tokamak L-mode confinement on magnetic field and plasma size, from a magnetic field scan experiment at ASDEX Upgrade to full-radius integrated modelling and fusion reactor predictions". In: *Nuclear Fusion* 63.5 (2023), p. 056005.

[90] C. K. Kiefer, C. Angioni, G. Tardini, N. Bonanomi, B. Geiger, P. Mantica, T. Pütterich, E. Fable, P. Schneider, A. U. Team, et al. "Validation of quasi-linear turbulent transport models against plasmas with dominant electron heating for the prediction of ITER PFPO-1 plasmas". In: *Nuclear Fusion* 61.6 (2021), p. 066035.

[91] C. Angioni, E. Fable, F. Ryter, P. Rodriguez-Fernandez, T. Pütterich, A. U. Team, et al. "The local nature of the plasma response to cold pulses with electron and ion heating at ASDEX Upgrade". In: *Nuclear Fusion* 59.10 (2019), p. 106007.

[92] P. Rodriguez-Fernandez, C. Angioni, and A. White. "Local transport dynamics of cold pulses in tokamak plasmas". In: *Reviews of Modern Plasma Physics* 6.1 (2022), p. 10.

[93] A. Mariani, P. Mantica, I. Casiraghi, J. Citrin, T. Görler, G. Staebler, and J. EUROfusion. "Benchmark of quasi-linear models against gyrokinetic single scale simulations in deuterium and tritium plasmas for a JET high beta hybrid discharge". In: *Nuclear Fusion* 61.6 (2021), p. 066032.

[94] B. Grierson, G. Staebler, W. Solomon, G. McKee, C. Holland, M. Austin, A. Marinoni, L. Schmitz, R. Pinsker, D.-D. Team, et al. "Multi-scale transport in the DIII-D ITER baseline scenario with direct electron heating and projection to ITER". In: *Physics of Plasmas* 25.2 (2018).

[95] J. Candy, C. Holland, R. Waltz, M. R. Fahey, and E. Belli. "Tokamak profile prediction using direct gyrokinetic and neoclassical simulation". In: *Physics of Plasmas* 16.6 (2009).

[96] C. Holland, J. Kinsey, J. DeBoo, K. Burrell, T. Luce, S. Smith, C. Petty, A. White, T. Rhodes, L. Schmitz, et al. "Validation studies of gyrofluid and gyrokinetic predictions of transport and turbulence stiffness using the DIII-D tokamak". In: *Nuclear Fusion* 53.8 (2013), p. 083027.

[97] and others. "Validation of IMEP on Alcator C-Mod and JET-ILW ELMy H-mode plasmas". In: *Plasma Physics and Controlled Fusion* 65.3 (2023), p. 034001.

[98] H. Dudding, F. Casson, D. Dickinson, B. Patel, C. Roach, E. Belli, and G. Staebler. "A new quasilinear saturation rule for tokamak turbulence with application to the isotope scaling of transport". In: *Nuclear Fusion* 62.9 (2022), p. 096005.

[99] Phys.org. *Asdex Upgrade experimental facility generates its first plasma*. `https://phys.org/news/2021-03-asdex-experimental-facility-plasma.html`. Accessed: July 6, 2023. 2021.

[100] K. Ida. "Experimental studies of the physical mechanism determining the radial electric field and its radial structure in a toroidal plasma". In: *Plasma Physics and Controlled Fusion* 40.8 (1998), p. 1429.

[101] M. Bergmann. "Analysis of Fast Rotating Mode Signals as Precursors of Locked Modes on the DIII-D Tokamak". MA thesis. München: Ludwig-Maximilians-Universität München, 2019.

[102] M. Sertoli, T. Odstrcil, C. Angioni, A. U. Team, et al. "Interplay between central ECRH and saturated (m, n)=(1, 1) MHD activity in mitigating tungsten accumulation at ASDEX Upgrade". In: *Nuclear Fusion* 55.11 (2015), p. 113029.

[103] R. Bilato, M. Brambilla, O. Maj, L. Horton, C. Maggi, and J. Stober. "Simulations of combined neutral beam injection and ion cyclotron heating with the TORIC-SSFPQL package". In: *Nuclear Fusion* 51.10 (2011), p. 103034. DOI: 10.1088/0029-5515/51/10/103034. URL: https://dx.doi.org/10.1088/0029-5515/51/10/103034.

[104] N. Teams, P. Lang, K. Büchl, M. Kaufmann, R. Lang, V. Mertens, H. Müller, and J. Neuhauser. "High-efficiency plasma refuelling by pellet injection from the magnetic high-field side into ASDEX upgrade". In: *Physical review letters* 79.8 (1997), p. 1487.

[105] *Position der Gaseinlassventile*. https://www.ipp.mpg.de/14869/tokamak. Accessed: 2023-08-24.

[106] D. Silvagni, P. Lang, T. Happel, A. Bock, R. Fischer, L. Gil, O. J. Kardaun, R. M. McDermott, U. Plank, B. Ploeckl, et al. "Pellet-fueled I-mode plasmas in ASDEX Upgrade". In: *Nuclear Fusion* (2023).

[107] A. Murari, L. Zabeo, A. Boboc, D. Mazon, and M. Riva. "Real-time recovery of the electron density from interferometric measurements affected by fringe jumps". In: *Review of scientific instruments* 77.7 (2006).

[108] H. Hartfuss, T. Geist, and M. Hirsch. "Heterodyne methods in millimetre wave plasma diagnostics with applications to ECE, interferometry and reflectometry". In: *Plasma Physics and Controlled Fusion* 39.11 (1997), p. 1693.

[109] S. S. Denk, R. Fischer, E. Poli, O. Maj, S. K. Nielsen, J. Rasmussen, M. Stejner, M. Willensdorfer, et al. "ECRad: An electron cyclotron radiation transport solver for advanced data analysis in thermal and non-thermal fusion plasmas". In: *Computer Physics Communications* 253 (2020), p. 107175.

[110] I. Garching. *https://www.aug.ipp.mpg.de/aug/local/diagnostik4/index.html*. https://www.aug.ipp.mpg.de/a

[111] B. Kurzan and H. Murmann. "Edge and core Thomson scattering systems and their calibration on the ASDEX Upgrade tokamak". In: *Review of scientific instruments* 82.10 (2011).

[112] E. Viezzer, T. Pütterich, R. Dux, R. McDermott, and A. U. Team. "High-resolution charge exchange measurements at ASDEX Upgrade". In: *Review of scientific Instruments* 83.10 (2012), p. 103501.

[113] R. Fischer, L. Giannone, J. Illerhaus, P. McCarthy, R. McDermott, and A. U. Team. "Estimation and Uncertainties of Profiles and Equilibria for Fusion Modeling Codes". In: *Fusion Science and Technology* 76.8 (2020), pp. 879–893.

[114] R. Fischer, E. Wolfrum, J. Schweinzer, et al. “Probabilistic lithium beam data analysis”. In: *Plasma Physics and Controlled Fusion* 50.8 (2008), p. 085009.

[115] O. Ford, J. Svensson, M. Beurskens, A. Boboc, J. Flanagan, M. Kempenaars, D. McDonald, A. Meakins, and J. E. Contributors. “Bayesian combined analysis of jet lidar, edge lidar and interferometry diagnostics”. In: *36th EPS Conference on Plasma Physics*. European Physical Society. 2009.

[116] D. Sivia and J. Skilling. *Data analysis: a Bayesian tutorial*. OUP Oxford, 2006.

[117] U. Von Toussaint. “Bayesian inference in physics”. In: *Reviews of Modern Physics* 83.3 (2011), p. 943.

[118] D. Stieglitz, J. Santos, R. Fischer, A. U. Team, et al. “Implementation and validation of swept density reflectometry for integrated data analysis at ASDEX Upgrade”. In: *Review of Scientific Instruments* 94.4 (2023).

[119] M. Griener, E. Wolfrum, M. Cavedon, R. Dux, V. Rohde, M. Sochor, J. Muñoz Burgos, O. Schmitz, U. Stroth, A. U. Team, et al. “Helium line ratio spectroscopy for high spatiotemporal resolution plasma edge profile measurements at ASDEX Upgrade”. In: *Review of Scientific Instruments* 89.10 (2018).

[120] D. Wendler, R. Dux, R. Fischer, M. Griener, E. Wolfrum, G. Birkenmeier, U. Stroth, A. U. Team, et al. “Collisional radiative model for the evaluation of the thermal helium beam diagnostic at ASDEX upgrade”. In: *Plasma Physics and Controlled Fusion* 64.4 (2022), p. 045004.

[121] R. Fischer, A. Dinklage, and E. Pasch. “Bayesian modelling of fusion diagnostics”. In: *Plasma Physics and Controlled Fusion* 45.7 (2003), p. 1095.

[122] R. Fischer, A. Bock, S. S. Denk, A. Medvedeva, M. Salewski, M. Schneider, D. Stieglitz, and A. U. Team. “Integrated Data Analysis and Validation”. In: *Nuclear Fusion ITER Special Issue* (2023). To be submitted.

[123] K. Höfler. *Turbulence measurements at the ASDEX Upgrade tokamak for a comprehensive validation of the gyrokinetic turbulence code GENE*. 2022.

[124] L. Horváth, G. Papp, P. Lauber, G. Por, A. Gude, V. Igochine, B. Geiger, M. Maraschek, L. Guimarais, V. Nikolaeva, et al. “Experimental investigation of the radial structure of energetic particle driven modes”. In: *Nuclear Fusion* 56.11 (2016), p. 112003.

[125] R. Fischer, K. Hanson, V. Dose, and W. von Der Linden. “Background estimation in experimental spectra”. In: *Physical Review E* 61.2 (2000), p. 1152.

[126] M. Nicholas, W. Rosenbluth Arianna, and N. Rosenbluth Marshall. “Teller Augusta H, Teller Edward. Equation of state calculations by fast computing machines”. In: *The journal of chemical physics* 21.6 (1953), pp. 1087–1092.

[127] W. K. Hastings. “Monte Carlo sampling methods using Markov chains and their applications”. In: *Biometrika* 57.1 (Apr. 1970), pp. 97–109. ISSN: 0006-3444. DOI: 10.1093/biomet/57.1.97. eprint: https://academic.oup.com/biomet/article-pdf/57/1/97/23940249/57-1-97.pdf. URL: https://doi.org/10.1093/biomet/57.1.97.

[128] C. E. Rasmussen, C. K. Williams, et al. *Gaussian processes for machine learning*. Vol. 1. Springer, 2006.

[129] S. Rathgeber, R. Fischer, S. Fietz, J. Hobirk, A. Kallenbach, H. Meister, T. Pütterich, F. Ryter, G. Tardini, E. Wolfrum, et al. "Estimation of profiles of the effective ion charge at ASDEX Upgrade with Integrated Data Analysis". In: *Plasma Physics and Controlled Fusion* 52.9 (2010), p. 095008.

[130] R. Fischer, A. Bock, M. Dunne, J. Fuchs, L. Giannone, K. Lackner, P. McCarthy, E. Poli, R. Preuss, M. Rampp, et al. "Coupling of the flux diffusion equation with the equilibrium reconstruction at ASDEX Upgrade". In: *Fusion Science and Technology* 69.2 (2016), pp. 526–536.

[131] R. Fischer, A. Bock, A. Burckhart, O. Ford, L. Giannone, V. Igochine, M. Weiland, M. Willensdorfer, A. U. Team, et al. "Sawtooth induced q-profile evolution at ASDEX Upgrade". In: *Nuclear Fusion* 59.5 (2019), p. 056010.

[132] B. Sudret. "Global sensitivity analysis using polynomial chaos expansions". In: *Reliability engineering & system safety* 93.7 (2008), pp. 964–979.

[133] J. Bergstra and Y. Bengio. "Random search for hyper-parameter optimization." In: *Journal of machine learning research* 13.2 (2012).

[134] I. M. Sobol'. "On the distribution of points in a cube and the approximate evaluation of integrals". In: *Zhurnal Vychislitel'noi Matematiki i Matematicheskoi Fiziki* 7.4 (1967), pp. 784–802.

[135] J. B. Nagel. "Bayesian techniques for inverse uncertainty quantification". In: *IBK Bericht* 504 (2019).

[136] R. C. Smith. *Uncertainty quantification: theory, implementation, and applications*. Vol. 12. Siam, 2013.

[137] H.-J. Bungartz and M. Griebel. "Sparse grids". In: *Acta numerica* 13 (2004), pp. 147–269.

[138] I.-G. Farcaş, T. Görler, H.-J. Bungartz, F. Jenko, and T. Neckel. "Sensitivity-driven adaptive sparse stochastic approximations in plasma microinstability analysis". In: *Journal of Computational Physics* 410 (2020), p. 109394.

[139] I. M. Sobol. "Global sensitivity indices for nonlinear mathematical models and their Monte Carlo estimates". In: *Mathematics and computers in simulation* 55.1-3 (2001), pp. 271–280.

[140] Höfler, K., Görler, T., Happel, T., Hennequin, P., Molina Cabrera, P., Bergmann, M., et al. *Experimental validation of gyrokinetic simulation with scale-resolved multi-field turbulence measurements*. URL: http://hdl.handle.net/21.11116/0000-000A-2B7D-B. 2023.

[141] Hawryluk. "An empirical approach, TRANSP, need better citation". In: ().

[142] C. F. B. Zimmermann, R. M. McDermott, C. Angioni, B. P. Duval, R. Dux, E. Fable, A. T. Salmi, U. Stroth, T. J. J. Tala, G. Tardini, and T. Pütterich. "Comparison of Momentum Transport in Matched Hydrogen and Deuterium H-mode Plasmas in ASDEX Upgrade". In: *Nuclear Fusion* (2023). URL: http://iopscience.iop.org/article/10.1088/1741-4326/acf387.

[143] C. F. B. Zimmermann. "Validation of Momentum Transport Theory in the Plasma Core of the ASDEX Upgrade Tokamak via NBI Modulation Experiments". PhD thesis. TUM, 2023.

[144] E. Fable, G. Tardini, A. U. Team, et al. "FEQIS: A new equilibrium solver for the Fenix flight simulator". In: *48th EPS Conference on Plasma Physics*. European Physical Society. 2022.

[145] G. Pereverzev and G. Corrigan. "Stable numeric scheme for diffusion equation with a stiff transport". In: *Computer Physics Communications* 179.8 (2008), pp. 579–585. ISSN: 0010-4655. DOI: https://doi.org/10.1016/j.cpc.2008.05.006. URL: https://www.sciencedirect.com/science/article/pii/S001046550800218X.

[146] E. Fable. "ASTRA-7.0, Addendum with changes and new features". In: Max-Planck-Institut für Plasmaphysik, 2012.

[147] W. Zholobenko, A. Stegmeir, M. Griener, G. Conway, T. Body, D. Coster, F. Jenko, A. U. Team, et al. "The role of neutral gas in validated global edge turbulence simulations". In: *Nuclear Fusion* 61.11 (2021), p. 116015.

[148] A. Bock, H. Doerk, R. Fischer, D. Rittich, J. Stober, A. Burckhart, E. Fable, B. Geiger, A. Mlynek, M. Reich, et al. "Advanced tokamak investigations in full-tungsten ASDEX Upgrade". In: *Physics of Plasmas* 25.5 (2018).

[149] P. B. Snyder, W. M. Solomon, K. H. Burrell, A. M. Garofalo, B. A. Grierson, R. J. Groebner, A. W. Leonard, R. Nazikian, T. H. Osborne, E. A. Belli, et al. "Super H-mode: theoretical prediction and initial observations of a new high performance regime for tokamak operation". In: *Nuclear Fusion* 55.8 (2015), p. 083026.

[150] A. Di Siena, P. Rodriguez-Fernandez, N. T. Howard, A. Banon Navarro, R. Bilato, T. Görler, E. Poli, G. Merlo, J. Wright, M. J. Greenwald, et al. "Predictions of improved confinement in SPARC via energetic particle turbulence stabilization". In: *Nuclear Fusion* (2022).

[151] B. Peherstorfer, K. Willcox, and M. Gunzburger. "Survey of multifidelity methods in uncertainty propagation, inference, and optimization". In: *Siam Review* 60.3 (2018), pp. 550–591.

[152] C. Bourdelle and J. Citrin. "Core turbulent transport in tokamak plasmas: bridging theory and experiment with QuaLiKiz". In: *Plasma Physics and Controlled Fusion* (2015).

[153] C. Stephens, X. Garbet, J. Citrin, C. Bourdelle, K. van de Plassche, and F. Jenko. "Quasilinear gyrokinetic theory: a derivation of QuaLiKiz". In: *Journal of Plasma Physics* 87.4 (2021), p. 905870409. DOI: 10.1017/S0022377821000763.

[154] C. D. Stephens. *Advances in quasilinear gyrokinetic modeling of turbulent transport*. University of California, Los Angeles, 2021.

[155] A. Ho, J. Citrin, C. Bourdelle, Y. Camenen, F. J. Casson, K. L. van de Plassche, H. Weisen, and J. Contributors. "Neural network surrogate of QuaLiKiz using JET experimental data to populate training space". In: *Physics of Plasmas* (2021).

[156] K. L. van de Plassche, J. Citrin, C. Bourdelle, Y. Camenen, F. J. Casson, V. I. Dagnelie, F. Felici, A. Ho, S. Van Mulders, and J. Contributors. "Fast modeling of turbulent transport in fusion plasmas using neural networks". In: *Physics of Plasmas* 27.2 (2020), p. 022310.

[157] M. D. McKay, R. J. Beckman, and W. J. Conover. "A comparison of three methods for selecting values of input variables in the analysis of output from a computer code". In: *Technometrics* 42.1 (2000), pp. 55–61.

[158] O. Meneghini, S. P. Smith, P. B. Snyder, G. M. Staebler, J. Candy, E. Belli, L. Lao, M. Kostuk, T. Luce, T. Luda, et al. "Self-consistent core-pedestal transport simulations with neural network accelerated models". In: *Nuclear Fusion* 57.8 (2017), p. 086034.

[159] J. Citrin, P. Trochim, T. Goerler, D. Pfau, K. van de Plassche, and F. Jenko. "Fast transport simulations with higher-fidelity surrogate models for ITER". In: *Physics of Plasmas* 30.6 (2023).

[160] A. Mikhailovskii, G. T. Huysmans, W. O. Kerner, and S. Sharapov. "Optimization of computational MHD normal-mode analysis for tokamaks". In: *Plasma Physics Reports* 23 (1997).

[161] C. Konz, W. Zwingmann, F. Osmanlic, B. Guillerminet, F. Imbeaux, P. Huynh, M. Plociennik, M. Owsiak, T. Zok, and M. Dunne. "First physics applications of the Integrated Tokamak Modelling (ITM-TF) tools to the MHD stability analysis of experimental data and ITER scenarios". In: *38th EPS Conference on Plasma Physics*. European Physical Society. 2011.

[162] D. Fajardo, C. Angioni, P. Maget, P. Manas, F. Casson, A. Field, J. Contributors, A. U. Team, et al. "Model for collisional transport of impurities in tokamaks and the combined effect of rotation and collisionality". In: *2022 US-EU Joint Transport Taskforce Workshop (TTF 2022)*. 2022.

[163] W. Kerner, J. Goedbloed, G. Huysmans, S. Poedts, and E. Schwarz. "CASTOR: Normal-mode analysis of resistive MHD plasmas". In: *Journal of computational physics* 142.2 (1998), pp. 271–303.

[164] M. Muraca, E. Fable, C. Angioni, T. Luda, P. David, H. Zohm, A. Di Siena, A. U. Team, et al. "Reduced transport models for a tokamak flight simulator". In: *Plasma Physics and Controlled Fusion* 65.3 (2023), p. 035007.

[165] P. Rodriguez-Fernandez, N. Howard, and J. Candy. "Nonlinear gyrokinetic predictions of SPARC burning plasma profiles enabled by surrogate modeling". In: *Nuclear Fusion* 62.7 (2022), p. 076036.

[166] P. Rodriguez-Fernandez, N. Howard, M. Greenwald, A. Creely, J. Hughes, J. Wright, C. Holland, Y. Lin, F. Sciortino, S. Team, et al. "Predictions of core plasma performance for the SPARC tokamak". In: *Journal of Plasma Physics* 86.5 (2020), p. 865860503.

[167] M. Greenwald. "Density limits in toroidal plasmas". In: *Plasma Physics and Controlled Fusion* 44.8 (2002), R27–R53. DOI: 10.1088/0741-3335/44/8/201. URL: https://doi.org/10.1088%5C%2F0741-3335%2F44%2F8%2F201.

[168] F. Troyon, R. Gruber, H. Saurenmann, S. Semenzato, and S. Succi. "MHD-Limits to Plasma Confinement". In: *Plasma Physics and Controlled Fusion* 26.1A (1984), pp. 209–215. DOI: 10.1088/0741-3335/26/1a/319. URL: https://doi.org/10.1088%2F0741-3335%2F26%2F1a%2F319.